A Feasibility Study of Bridge Deck Deicing Using Geothermal Energy

Morgan State University
The Pennsylvania State University
University of Maryland
University of Virginia
Virginia Polytechnic Institute & State University
West Virginia University

The Pennsylvania State University
The Thomas D. Larson Pennsylvania Transportation Institute
Transportation Research Building ❖ University Park, PA 16802-4710
Phone: 814-865-1891 ❖ Fax: 814-863-3707
www.mautc.psu.edu

1. Report No.	2. Government Accession No.	3. Recipient's Catalog No.
MAUTC-2013-02		

4. Title and Subtitle	5. Report Date
A Feasibility Study of Bridge Deck Deicing using Geothermal Energy	April 28, 2015
	6. Performing Organization Code

7. Author(s)	8. Performing Organization Report No.
Omid Ghasemi-Fare, G. Allen Bowers, Cory A. Kramer, Tolga Y. Ozudogru, Prasenjit Basu, C. Guney Olgun, Tanyel Bulbul, Melis Sutman	

9. Performing Organization Name and Address	10. Work Unit No. (TRAIS)
PI: Prasenjit Basu, Ph.D. The Pennsylvania State University Larson Transportation Institute 201 Transportation Research Building University Park, PA 16802 Co-PI: C. Guney Olgun, Ph.D. Virginia Polytechnic Institute and State University Department of Civil and Environmental Engineering 200 Patton Hall 750 Drillfield Drive Blacksburg, VA 24061	**11. Contract or Grant No.** DTRT12-G-UTC03

12. Sponsoring Agency Name and Address	13. Type of Report and Period Covered
US Department of Transportation Research & Innovative Technology Admin UTC Program, RDT-30 1200 New Jersey Ave., SE Washington, DC 20590	Final 1/1/2013-7/31/2014
	14. Sponsoring Agency Code

15. Supplementary Notes

16. Abstract

In this study, we investigated the feasibility of a ground-coupled system that utilizes heat energy harvested from the ground for deicing of bridge decks. Heat exchange is performed using circulation loops integrated into the deep foundations supporting the bridge or embedded within the approach embankment. The warm fluid extracted from the ground is circulated through a tubing system embedded within reinforced concrete bridge deck to keep the deck temperature above the freezing point. A circulation pump that requires a minimal amount of power is used for fluid circulation. This is different from ground-source heat pump systems used for heating and cooling of buildings. In this study, a proof-of-concept testing is developed to investigate the operational principles and key design parameters. Experiments were performed on a model-scale instrumented bridge deck and model heat-exchanger piles to investigate heat transfer within different components of the ground-coupled bridge deck system. Heat transfer within ground and concrete bridge deck is quantified through numerical simulations under a variety of design and operational conditions. Experimental and numerical studies performed both at Penn State and Virginia Tech campuses demonstrate that this technology has a significant potential in reducing the use of salts and deicing chemicals. The knowledge and experience gained from this research will guide future research on real-life implementation of the proposed alternative bridge deck deicing method and will eventually help the concept to grow as a ready-to-use technology. Consequently, it will be possible to reduce bridge deck deterioration and offset the detrimental effects and environmental hazards caused by these chemicals.

17. Key Words: Geothermal energy; Deicing technology; Concrete bridges; Heat transfer analysis; Heat exchanger piles	18. Distribution Statement No restrictions. This document is available from the National Technical Information Service, Springfield, VA 22161

19. Security Classif. (of this report)	20. Security Classif. (of this page)	21. No. of Pages	22. Price
Unclassified	Unclassified	110	

Table of Contents

List of Figures

List of Tables

1. Problem Statement

Deicing the bridge decks is one of the major problems in the snowy areas which can create dangerous conditions for motorists. The common deicing solutions (i.e., the use of salts and other debonding chemicals) accelerate corrosion of steel reinforcement used in concrete bridge deck and reduce available reinforcement area over time. Such reduction in reinforcement area results in overstress in the available steel cross section and, therefore, creates potential detriment of structural integrity. Naito *et al*. (2010) reported several collapses of reinforced concrete (RC) bridge decks due to corrosion of steel reinforcements. Thus long term use of salts and deicing chemicals increases the maintenance and repair cost for RC bridges. Furthermore, chemical or salts can create potential damage for environment. Such chemicals can contaminate groundwater through surface runoff. Therefore, alternative solutions should be considered to reduce the detrimental effects of chemical deicing agents on RC bridge decks and to reduce environmental hazards caused by these chemicals.

Several research studies have been performed to investigate the deterioration of bridge infrastructures due to chloride attack resulted from salts (Virmani *et al*. 1983, 1984; Baboian, 1992; Yunovich *et al*. 2003; White *et al*. 2005; Granata and Hartt, 2009). Although recent developments suggest the use of corrosion resistant reinforcing steel in RC bridge decks, such an alternative is applicable for new bridge construction only. Structural deterioration of existing bridges due to chloride attack still remains a significant threat to the nation's highway infrastructure. Koch *et al*. (2002) estimated that the annual direct cost due to bridge corrosion is in the range of $6 to $10 billion. Considering the indirect cost, the total cost would be as much as 10 times higher than the direct costs (Yunovich *et al*. 2003). Based on a recent FHWA report (FHWA, 2008) 40% and 19% of the total 600,000 bridges in the U.S. were built with, respectively, conventional reinforced concrete and prestressed concrete. According to the same report, one quarter of the existing bridges are classified as structurally deficient or functionally obsolete. According to the recent landmark report "Bridging the Gap" bridge deterioration was ranked at the top of the major issues facing the nation-wide bridge infrastructure (AASHTO 2008). Based on AASHTO (2005), *optimization of structural systems* and *the extension of service life of bridges with minimal maintenance* were identified by a strategic plan as the two grand challenges facing the nation's highway infrastructure. The Strategic Highway Research Plan 2, with one of the main goals set to achieve a 100-year or longer service life for bridge infrastructure, was authorized by the U.S. Congress in 2005 (SHRP2, 2006). According to AASHTO (2008), materials and techniques need to be developed to improve safety, longevity, and economy of bridge infrastructure though innovative research.

This collaborative research study by The Pennsylvania State University (PSU) and Virginia Tech (VT) investigates the feasibility of bridge deck deicing through ground-source heating system integrated with deep foundations supporting the bridge and possibly embedded within the approach embankment. Based on the expertise and capabilities of both project teams at PSU and VT a comprehensive research with a successful execution of the project tasks was achieved.

Based on the results obtained from experimental and numerical models, the effects of different operational, design and site-specific parameters on the amount of energy harvested through geothermal piles, that can serve as bridge foundation, were studied. The proposed bridge deck deicing technology is very promising and this report determines the key parameters that govern the physical process. By considering the results presented in this report preliminary design recommendations for the ground-source bridge deck deicing technology can be developed. In this research we have investigated the operational principles, and we have identified the key design parameters. Also a proof-of-concept testing approach that has the potential to transform the concept into a ready-to-use technology was developed in this study. This research helps meeting the objective of increasing the service life of RC bridges by providing valuable insight into an innovative, energy-efficient and environmentally friendly alternative for bridge deck deicing.

2. Review of Existing Literature

Seasonal variation of ground temperature below a certain depth (usually below a depth of about 20 ft) is relatively constant (Kusuda and Achenback 1965). Geothermal pile foundations are good candidates to harvest shallow geothermal energy due to the fact that they often extend below this depth. Heat can be transported to and from the ground by circulating heat carrier fluid through a closed loop embedded within concrete piles. The use of geothermal piles, also known as energy piles or heat exchanger piles, in bridge foundations has a great potential for environmental and economic benefits. A pile-anchored heat pump system can be used as an environmentally friendly alternative to the conventional solutions for bridge deck deicing (e.g., use of salts, chemicals, and energy intensive heating methods). Such a system can also be useful during summer to reduce the severity of the thermal stresses within concrete bridge decks.

2.1 Geothermal bridge deck deicing case histories

There are several case studies of ground-source bridge deck heating; however, none of these studies use geothermal pile technology. Minsk (1999) documents several cases where geothermal energy is utilized to heat a bridge deck. A bridge over the North Fork of Silver Creek in Oregon uses well water supplied to a heat pump, which is then used to hydronically heat the bridge deck. Another system in Texas utilizes a geothermal borehole field. The boreholes are 4 inches in diameter and 176 ft deep. The wells are connected to a heat pump, but the system has been successfully used to prevent snow accumulation on the deck by circulating the fluid directly from the borehole field to the deck without the use of a heat pump.

Liu *et al*. (2003, 2007) built an experimental 18.3 m x 6.1 m (60 ft x 20 ft) bridge deck with embedded heat exchanger tubes. The geothermal energy was supplied from a vertical closed-loop ground-source heat exchanger consisting of six 0.13 m (5.25 in) diameter boreholes, each containing a single circulation loop. The geothermal borehole system was connected to a heat pump. With the use of a heat pump, this system was able to successfully keep the deck snow-free during several winter storm events.

Yoshitake *et al*. (2011) reports two bridges in Japan that use geothermal energy to heat an underground tank of water to ground temperature. This water is then circulated through embedded tubes in the bridge decks when needed and relies on geothermal energy alone with no heat pump. The system operates whenever the lowest temperature in a bridge deck is less than 0.5°C. During several snow events, the system performed well and was able to prevent significant snow accumulation. They also reported results of the temperature variation of the water in the tank and of the ground surrounding the tank. A significant observation is that they were able to increase the temperature of the water in the tank during the summer by running the system and this in turn increased the temperature of the ground around the tank.

2.2 Numerical studies of bridge deck deicing

Several numerical studies have considered both the transient and two-dimensional components of a hydronic heating system. Rees *et al*. (2002) developed a two-dimensional numerical model that accounted for the transient effects of the snow melting process on a pavement snow melting system's performance. The authors modeled a cross section of the slab that included one-half of the heating element and extended to a distance directly between two heating elements. The slab rested on soil and the surface boundary condition was controlled by a surface boundary model that was developed to account for seven possible surface conditions. The study included a parametric analysis of pipe configuration, the system's geographical location, and the storm. Results were analyzed by observing the required heat flux to maintain a given snow-free area ratio where the required heat flux could be used and then determine the required inlet fluid temperature. One conclusion from this study is that in order to achieve a snow-free area ratio system idling (or preemptive heating in anticipation of a storm) will likely be required.

Liu *et al*. (2003) improved upon the model found in Rees *et al*. (2002) to simulate hydronic heating of bridge deck over its lifetime as opposed to singular storm events as well as to incorporate a ground-source heat pump. The entire model consisted of four sub-models: a hydronically heated bridge deck model, a ground loop heat exchanger model, a water to water heat pump model, and a system control model. The model was then experimentally validated with a hydronic ground-source bridge deck deicing system installed in an experimental bridge at Oklahoma State University. The deck is 18.3 m long by 6.1 m wide with 19 mm hydronic tubing installed on 0.3 m centers at a depth of 89 mm. The system is designed to control the bridge deck temperature in the range of 4.4-5.6°C (40-42°F) when there is a risk of snowfall. The model did a good job in predicting the average bridge surface temperature and fluid exiting temperature but slightly over predicted the surface temperatures. The authors highlight the difficulty of numerically accounting for the long-wave radiation and convective heat fluxes.

Liu and Spitler (2004) utilize the simulation from Liu *et al*. (2003) and perform a parametric study to investigate the effects of idling time, pipe spacing, slab insulation, and control strategies on system performance. Among their findings are that preemptive heating is required to achieve the expected snow-melting performance when using the tabulated ASHRAE surface heat flux. Furthermore, preheating the slab with full heating capacity before snowfall can significantly

improve the system's performance. This model has been further refined (Liu *et al*. 2007a) and validated (Liu *et al*. 2007b).

3. Laboratory-scale tests on a model heat exchanger pile

The geothermal model pile setup, built and used in this study, is located at the Civil Infrastructure Testing and Evaluation Laboratory (CITEL) facility of The Pennsylvania State University (PSU), University Park. A model-scale precast geothermal pile was embedded in sand bed prepared within a large soil tank (**Error! Reference source not found.**).

One of the main advantages of model pile tests is that multiple load tests under varying conditions can easily be performed under fully controlled testing conditions, avoiding uncertainties of natural soil profiles. The model geothermal pile was subjected to several thermal and mechanical load cycles under varying conditions. Through these thermal performance tests, the effect of circulation flow rate, and inlet fluid temperature on the amount of energy harvested from the ground and soil temperature increments were investigated.

The model geothermal pile was installed in a sand bed prepared within a custom-designed steel tank. The soil tank has a 1.83 m × 1.83 m (6 ft × 6 ft) square cross-section and is composed of a 1.22-m-tall base portion and a top portion with height equal to 0.91 m (Figure 3-1a). The upper half of the tank fits directly on top of the lower portion of the tank, and has bolted connections around the circumference of the tank. The advantage of having two separate sections for the tank is that the lower part of the tank is more easily accessible (without the top half placed on it) during preparation and instrumentation of the soil bed. An adjustable reaction frame is attached to the tank, position of the cross beam in this reaction frame can be changed to attain a desired height during pile load tests.

3.1 Scale Effect

The width of the soil tank is equal to 18 times pile diameter B. For nondisplacement piles, the distance of the free-field boundary is dictated mostly by loading condition (i.e., lateral versus axial); however, for displacement piles such boundary is mostly governed by installation process (i.e., driving or jacking). Literature suggests that for axial load tests on nondisplacement piles in sand, the use of a tank that is at least 8 to 10 pile diameters wide is sufficient to avoid mechanical boundary effects; however, such a distance should be significantly higher for full displacement piles (Kraft 1991, Parkin *et al*. 1982, Schnaid and Houlsby 1991, Salgado *et al*. 1998). The distance between the pile base and the bottom boundary is kept equal to 6B, which is greater than the expected zone of influence (around 1.5B to 3B) below the pile base when the pile is subjected to axial loading (Salgado 2008). In addition to the mechanical boundary effects, the tank is designed to avoid immediate thermal boundary effects. The test program and soil tank dimensions were designed carefully to quantify the effect of thermal boundary conditions and pile geometry on heat transfer performance of the model pile. The thermal performance tests results may also be projected to assess heat transfer performance of real geothermal piles under

field conditions. Preliminary finite element simulations of heat transfer through the model pile suggested that thermal loading can be applied for almost seven days before any change in temperature at the tank boundary. Actual thermal tests in the tank later validated such initial calculation. To compare heat flow measured during a laboratory scaled model test with a full-scale system, soil temperature is reported for both real time and normalized time expressed by Fourier number Fo:

$$\mathrm{Fo} = \frac{\alpha_s t}{r_p^{\,2}} \qquad (3\text{-}1)$$

where t is real time, r_p is the pile radius, and α_s is thermal diffusivity of soil (r_p, α_s and t are in consistent units to make Fo dimensionless). Using Fourier number Fo is reasonable to compare the time scales for laboratory scaled model test and a real geothermal pile.

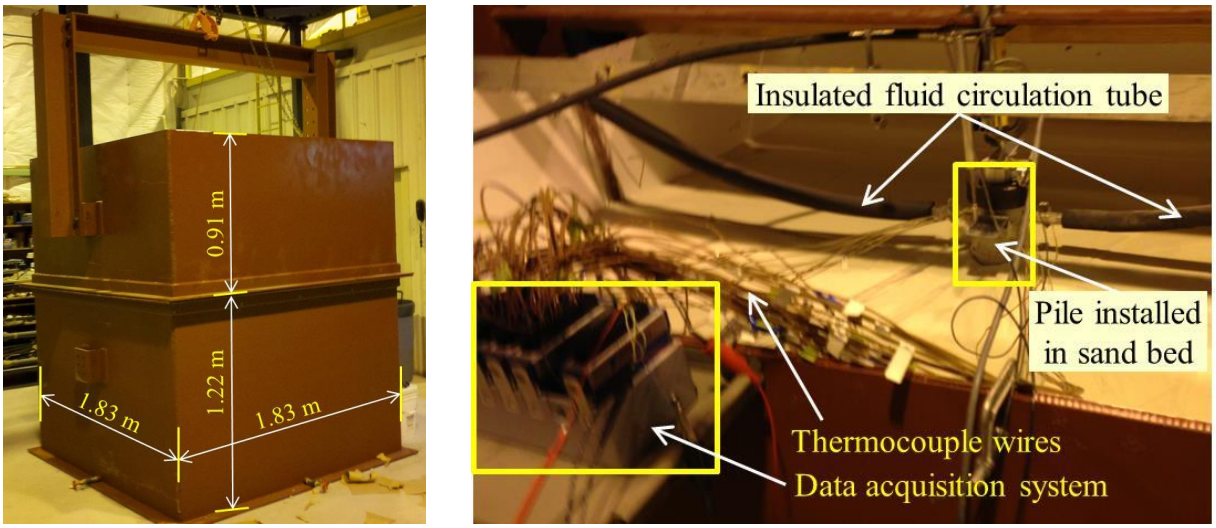

(a) (b)

Figure 3-1 **Setup for model-scale tests performed at PSU: (a) soil tank (b) top view of the model geothermal pile embedded in the sand bed**

3.2 Test setup

The test bed was prepared using conventional 'sand raining' technique (Bieganousky and Marcason 1976, Rad and Tumay 1987, Cresswell *et al*. 1999). A pluviation system (0.76 m × 0.76 m) was designed and fabricated for raining sand into the soil tank. This system contains a perforated steel box with an attached shutter plate on its bottom (to stop sand raining when desired) and up to four layers of sieves underneath. The large sieves which were fabricated for use in the pluviation device include #6, #10, #12, and #16 standard size meshes (corresponding to sieve opening sizes 3.36, 2.00, 1.68 and 1.19 mm, respectively). Desirable relative density was achieved by choosing an appropriate sand drop height and the combination of three sieve sizes. The assembled pluviator with three of the four sieves attached is shown in Figure 3-2. By

reaching to the desired level of pile base, sand deposition was temporary stopped to place the model geothermal pile. The model pile was held vertically until the sand deposition process was finished. This model pile installation process closely simulates the in situ stress condition that would exist around nondisplacement piles, i.e., piles that produce minimal or zero soil displacement during its installation and thus, the in situ stress condition in the vicinity of the pile is not significantly disturbed by pile installation (Salgado 2008). Before starting the sand pluviation into the tank, the bottom of the tank was filled using a 6 cm crushed stone layer which was covered with a felt fabric. The stone layer can facilitate tank saturation and allowed uniform bottom-up saturation of the sand bed. Also, this layer reduced possibility of piping. The fabric layer used to separate sand and stone layers to avoid clogging of the crushed stone. The criterion for aperture size of the fabric layer is that the aperture size should be small enough to block the sand particles from passing into the layer. However, the cloth should be the water permeable layer.

Figure 3-2 **Sand pluviation system using #6, #10, and #12 sieves**

To ensure quality and repeatability of sand raining method, trial sand depositions using different combinations of sieve sizes and varying fall heights (measured from the bottom of the shutter plate) were performed. To establish the relation between the fall height and sieve combinations, density calibration plots were prepared. As expected, increasing the number of sieves increases relative density of the sand deposit. Interestingly, using more than two sieves would not increase the relative density of the sand deposit. It can be noted that from this point on, the relative density is pretty much independent of the sieves numbers and it is only a function of drop height. For a desirable relative density of the sand deposition, the sieve combination and drop height can be determined from Figure 3-3. This figure shows that three different sieve combinations with two or more sieves. Repeatability of the deposition process falls within a 4% of standard

deviation. According to the Figure 3-3, sieves #6, and #10 with the drop height of 80 cm was adopted to pluviate the sand into the soil tank with desirable relative density. The tank was filled using 7.5 cm lifts, with instrumentation placed at desired depths between lifts.

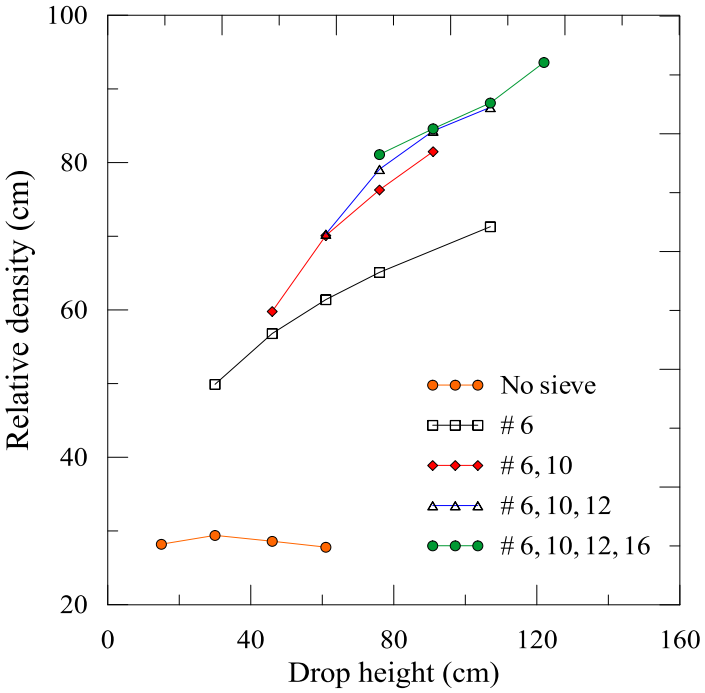

Figure 3-3 **Relative density calibration curve**

3.2.1 Sand bed saturation

Dry sand was first deposited into the tank and then water was pumped into the tank from the bottom of the each side of the tank. The 7cm crushed stone layer and the fabric layer at the bottom of the tank prohibited the piping issues and erosion of the tank. Since the hydraulic conductivity of the limestone is an order of magnitude higher than Ottawa sand, the layer can be considered as free draining layer. Therefore, water level would easily and slowly rise through the tank. Since water pass through the preferential pass ways, percolation effects will halter the full saturation of the sand deposit (Iskander 2010). Therefore to ensure that the sand deposit is in near saturation condition, 5 times of the void volume of the sand bed was pumped into and out to the tank from bottom and top surface, respectively.

3.2.2 Model geothermal pile

A concrete pile with the diameter of 100 mm and 1.38 mm length was designed for this study. A U-shaped poly-vinyl chloride (PVC) circulation tube was embedded within the pile. The inner and outer diameters of the PVC tube were, respectively, 9.5 mm and 12.7 mm. The model pile was embedded 1.22 m into the sand deposit. Bottom displacement of the model pile was measured using a telltale rod passed through the entire pile length to rest on the pile base. The room for the telltale rod was accommodated by placing a 9.5-mm-diameter PVC tube within the formwork before casting the concrete. According to the FHWA recommendation, 25.4 mm

concrete cover was used based on the maximum aggregate size in the concrete mix. Figure 3-4 shows a schematic view of the model pile with embedded U-shaped tube and the telltale sheath.

The concrete mix was designed according to the Federal Highway Administration guideline for drilled shafts (FHWA 2010). Fine aggregate of the concrete was selected such that it meets ASTM C33 specifications. River sand was used as a fine aggregate. Specific gravity of the river sand used was 2.60 as determined by ASTM D854 and its absorption capacity was 0.96%. According to the ASTM D6913 the fineness modulus of the sand was 2.93. Based on the FHWA mix design recommendations and ACI 211.1 mix design procedures, mix design for the concrete pile per cubic meter of the concrete is presented in Table 3-1.

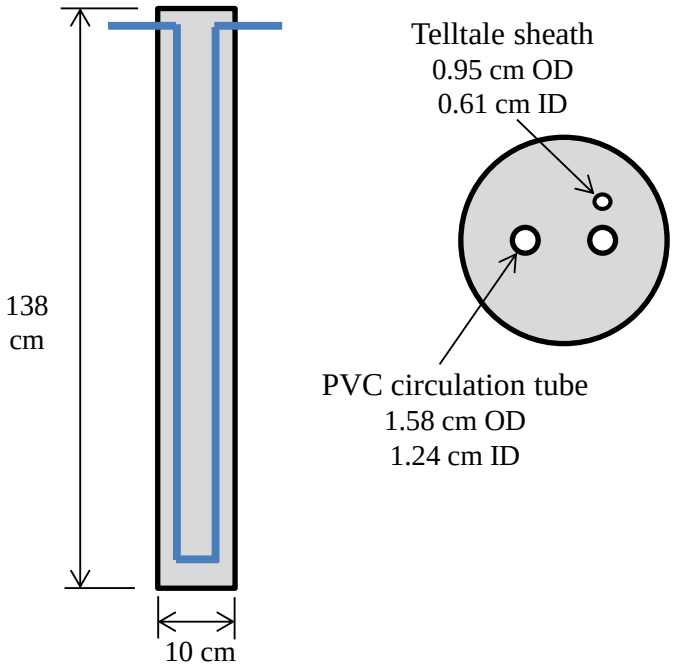

Figure 3-4 **Vertical and horizontal cross-sections of the test pile**

To achieve the desired workability such that the concrete would flow into the form and around the circulation tubing, water-reducing admixture (Glenium 7710) was added at a ratio of 722 mL/m^3. With this mix design, the fresh concrete had a measured slump of 140 mm and an air content of 2%.

Table 3-1 **Concrete mix design (per cubic meter) for model pile**

Material	Weight (kg)	Volume (m^3)
Water	181	0.181
Cement	427	0.135
Coarse Aggregate	549	0.200
Fine Aggregate	584	0.231
Air	0	0.023

3.3 Material Characterization

3.3.1 Sieve Analysis

Standard F50 Ottawa sand (silica sand) was selected for use in this research. The mean particle size D50 of this sand equals to 0.25 mm, and coefficient of uniformity C_u and coefficient of curvature C_c are, respectively, equal to 1.8 and 0.95. Figure 3-5Figure 3-5 shows the particle size distribution curve for this sand according to ASTM D6913-04.

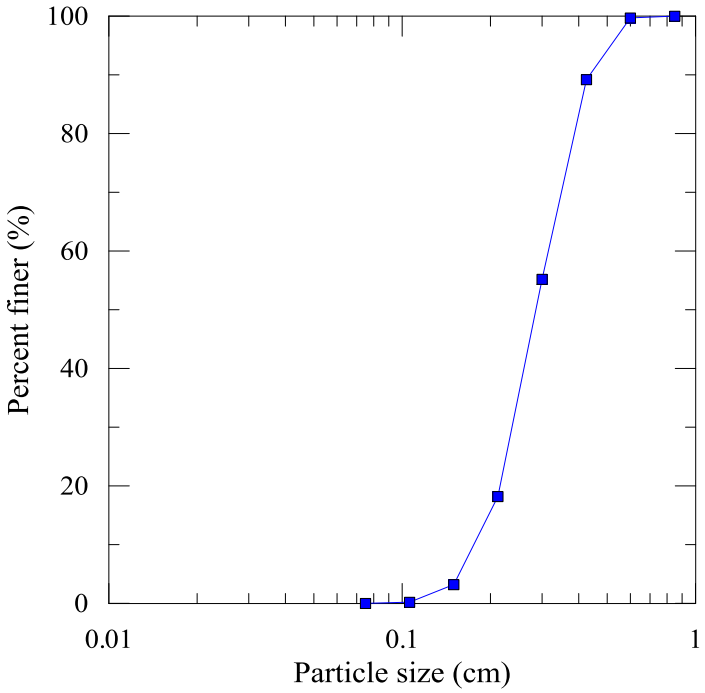

Figure 3-5 **Particle size distribution curve for F50 Ottawa sand**

Material used as crushed limestone at the base of the tank was selected based on the ASTM C33 criteria for #8 stone. Figure 3-6 shows the particle size distribution for crushed limestone. Specific gravity of the limestone is 2.80. According to the ASTM C127 the mean particle size

D50 of this material equal to 6.8 mm, and coefficient of uniformity C_u equal to 1.76 according to ASTM D6913.

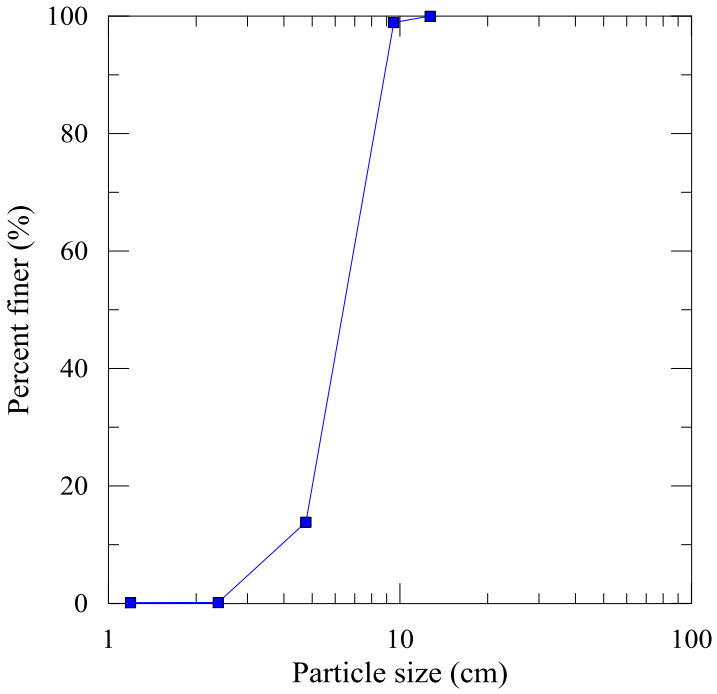

Figure 3-6 **Particle size distribution for crushed limestone**

3.3.2 Mechanical properties of Ottawa sand

According to ASTM D854-10 the pycnometer method was used to measure the specific gravity G_s of the silica sand used in this research. Specific gravity determined from the pycnometer test was 2.65. Minimum and maximum void ratios were also measured in this research to calculate relative density. According to ASTM D4253 and ASTM D4254 the maximum and minimum void ratios were determined to be equal to 0.78 and 0.48, respectively. Since the desired relative density used for sand deposit was 75%, direct shear method was used to determine the critical friction angle of F50 sand at 75% relative density. According to ASTM D3080, different direct shear tests were performed under normal stresses of 100, 200, 300 and 400 kPa. The critical state friction angle calculated from direct shear tests results was found to be 31.8°. Figure 3-7 shows the results obtained from direct shear test.

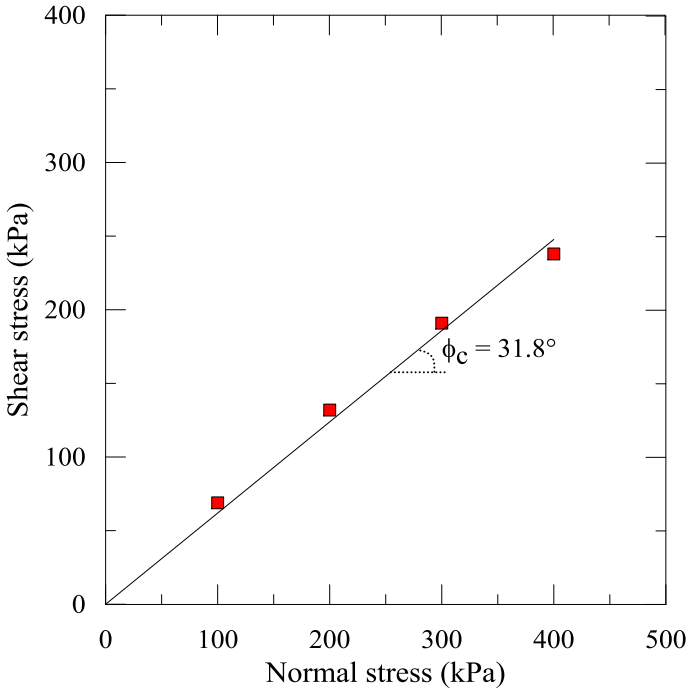

Figure 3-7 **Results from direct shear tests on F50 Ottawa sand**

3.3.3 Scanning electron microscope (SEM)

To investigate the typical shape and the mineral composition of the F50 Ottawa sand, the scanning electron microscope (SEM) and X-ray spectroscopy (EDS) tests were performed on this sand. As Figure 3-8 shows SEM images proves that the sand particles are sub angular. As expected, energy-dispersive X-ray spectroscopy (EDS) reveals that the dominant mineral composition of the F50 Ottawa sand is quartz (Figure 3-9). It also showed that there are some traces of aluminum oxides and other metal oxides in the mineral compositions as well.

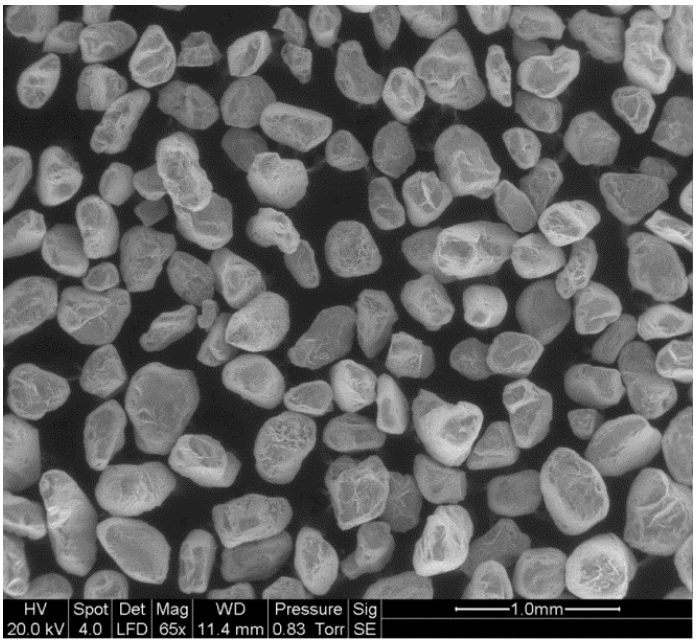

(a)

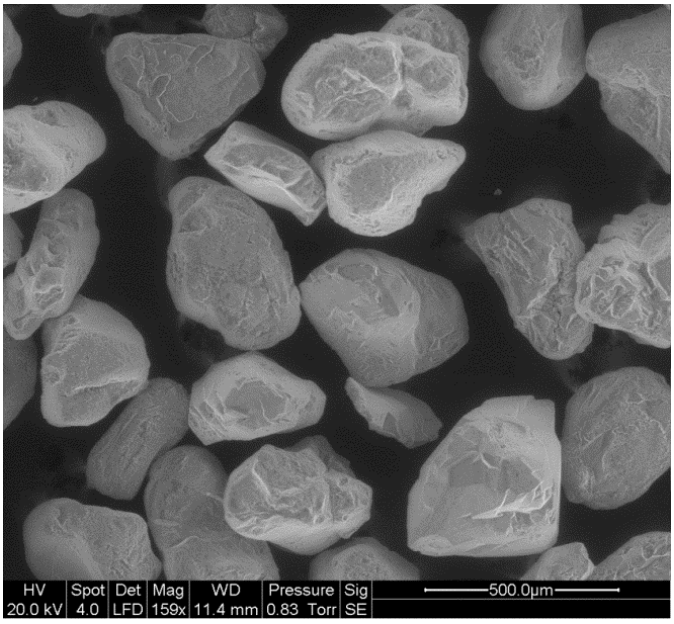

(b)

Figure 3-8 **SEM image of F50 silica sand: (a) at 65x magnification and (b) at 159x magnification**

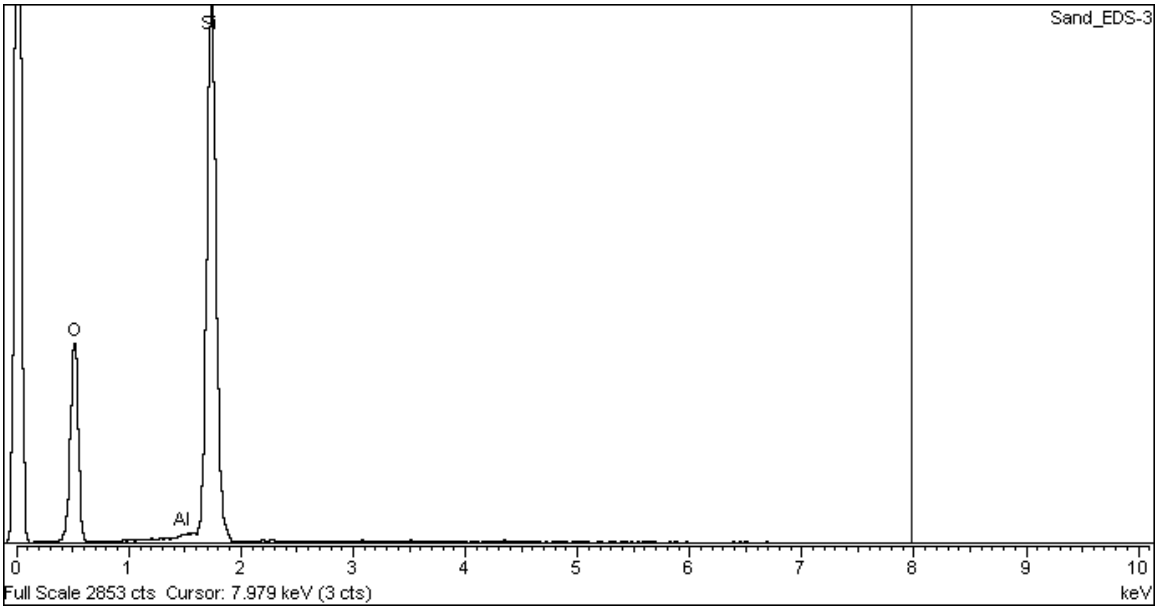

Figure 3-9 **Results from EDS spectrum for F50 Ottawa sand**

3.3.4 Thermal conductivity

To determine the thermal conductivity of the sand and the concrete, two thermal conductivity test setups were built during this study (Figure 3-10). These setups were similar to the ASTM D5334 test which is for measuring thermal conductivity in soil and soft rock. The difference between the apparatus used in this study and the ASTM test was that a heat carrying fluid was used as the heat source instead of a heating probe. The diameter and height of the model equal 0.3m, and 0.6 m, respectively. Heat source was placed at the center of the mold. Same PVC tube which was embedded within the model geothermal pile was used at the center of the thermal conductivity test setup (outer diameter was 15.8 mm, and inner diameter was 12.4 mm). Fourier's law can be used to calculate thermal conductivity of the material inside the mold (soil and concrete).

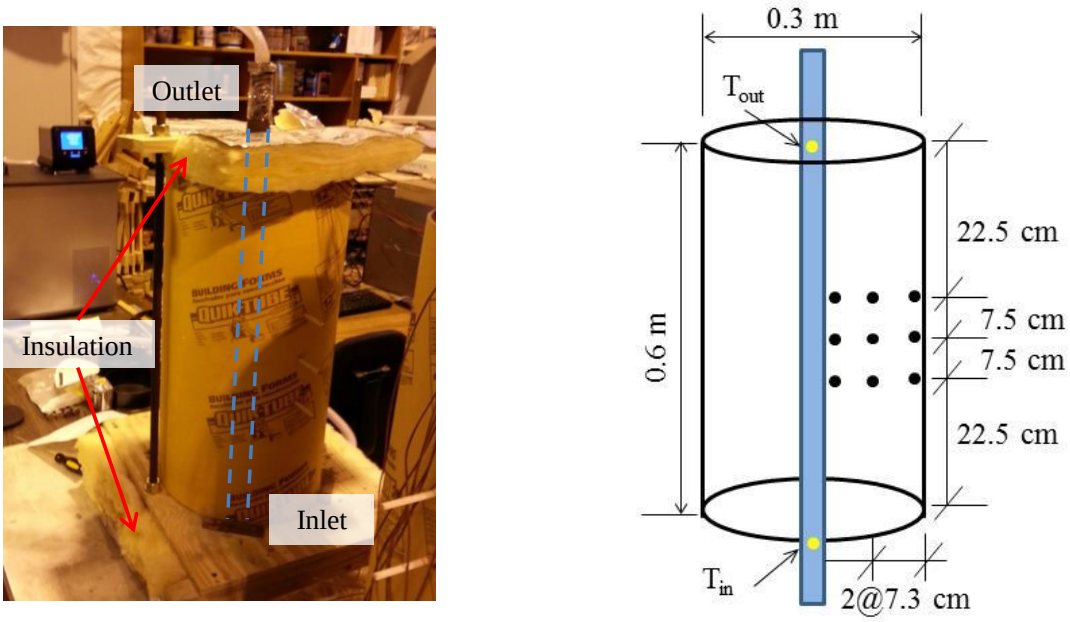

(a) (b)

Figure 3-10 **Element test setup to measure thermal conductivity of sand and concrete: (a) custom-built test apparatus and (b) temperature measurement locations**

Fluid temperature at the inlet side was maintained at a constant value and the outlet fluid temperature was monitored during the thermal conductivity tests. The system was allowed to reach to the thermal equilibrium. Figure 3-11 shows the results for both concrete and soil thermal conductivity tests and the equilibrium states. According to the Fourier's law, based on the total energy dissipated from the heat source to the media and radial soil temperature increments, the thermal conductivity value *k* can be calculated. Equation (**Error! Reference source not found.**) hows how the total energy can be predicted using the temperature difference between fluid inlet and outlet points.

$$E = \dot{m} C_p (T_{in} - T_{out}) \tag{3-2}$$

where *E* is the energy dissipated to the media, $\dot{m}$ is the mass flow rate of the fluid which depends on the circulation velocity and tube's area, *C*p is the specific heat capacity of the fluid, and T_{in} and T_{out} are, respectively, fluid temperatures at the inlet and outlet points. While the system is in the thermal equilibrium state (steady-state), Fourier's law can be applied to determine thermal conductivity of the material.

$$k = \frac{\dot{m} C_p (T_{in} - T_{out}) \ln\left(\frac{r_2}{r_1}\right)}{2\pi L (T_1 - T_2)} \tag{3-3}$$

where k is the material thermal conductivity, L is the length of the heat source, T_1 and T_2 are temperature recorded at radial distances r_1 and r_2 from the centerline of the heat source (circulation tube).

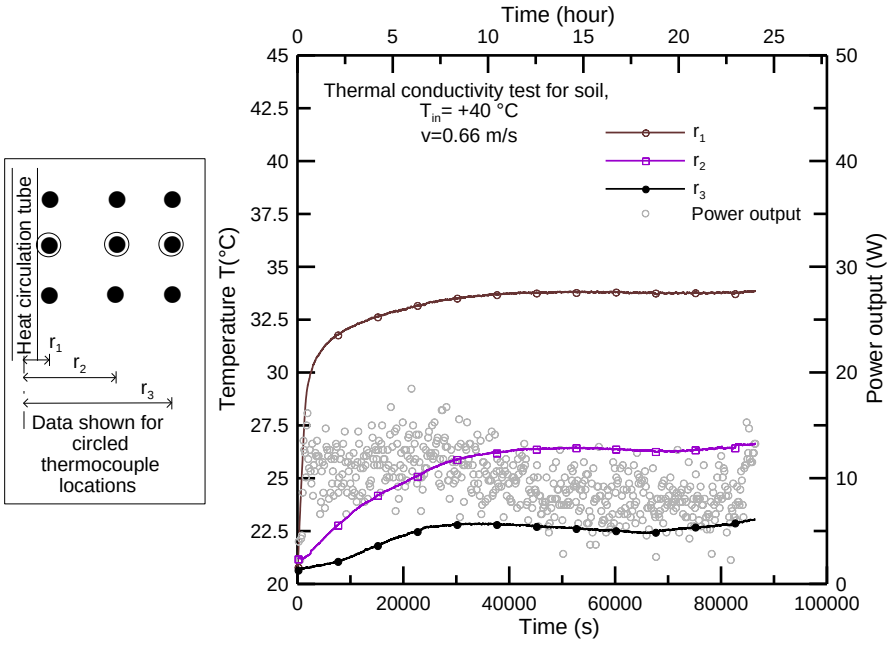

(a)

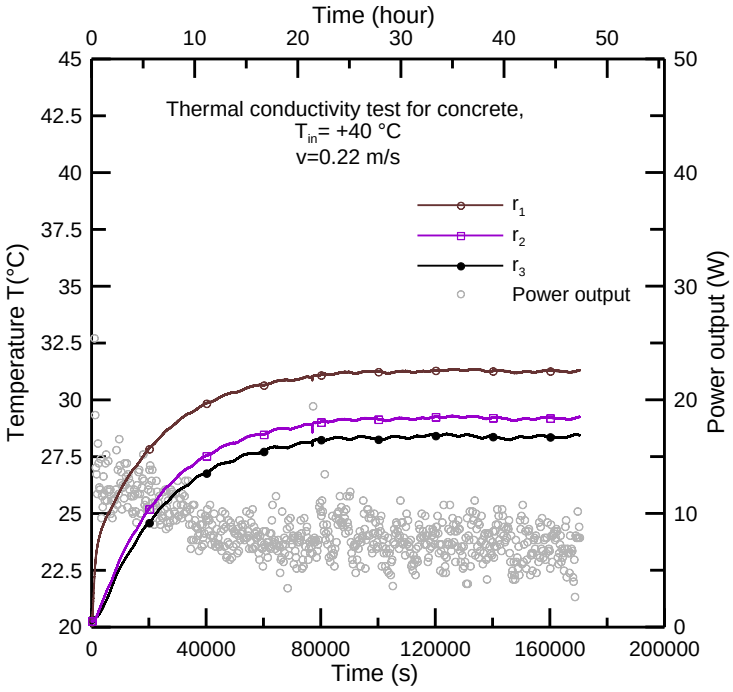

(b)

Figure 3-11 **Thermal conductivity test results for (a) sand (b) concrete**

3.3.5 Hydraulic conductivity

The hydraulic conductivity values for different void ratios (relative densities) for the F50 sand were measured following ASTM D2434-68. As Figure 3-12 shows, hydraulic conductivity value varies from 0.025 to 0.038 cm/s for the void ratio varying between 0.54 and 0.72.

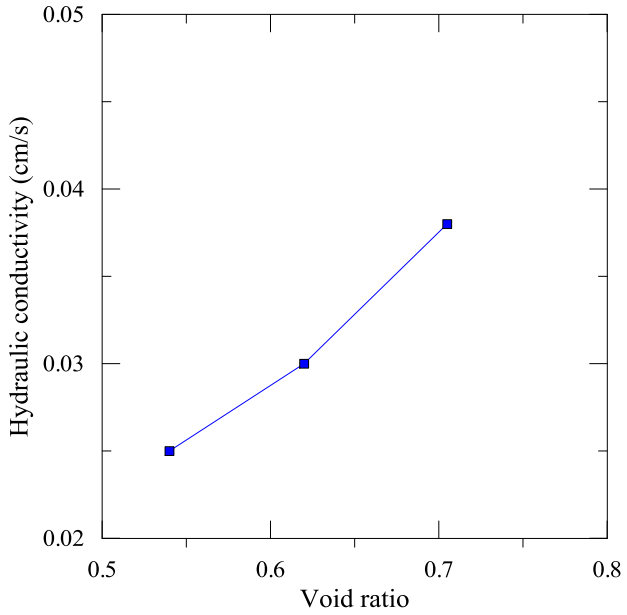

Figure 3-12 **Hydraulic conductivity of F50 Ottawa sand as a function of void ratio**

Based on the sieve analysis, direct shear test, SEM, EDS and thermal conductivity tests, various properties for the F50 Ottawa sand are summarized in Table 3-2.

Table 3-2 **Properties of F50 Ottawa sand**

Parameter	**Value**	**Test Method**
Shape	Subangular	Scanning Electron Microscope
Mineral composition	> 99% Quartz	Energy Dispersive Spectroscopy
Mean particle size, D_{50} (mm)	0.25	ASTM D6913
Coefficient of Uniformity, C_u	1.83	ASTM D6913
Coefficient of Curvature, C_c	0.95	ASTM D6913
Specific gravity, G_s	2.65	ASTM D854
Minimum void ratio, e_{min}	0.48	ASTM D4253
Maximum void ratio, e_{max}	0.78	ASTM D4254
Critical state friction angle, φ_c	31.8°	ASTM D3080
Hydraulic conductivity ($cm \cdot s^{-1}$)	0.025 to 0.038	ASTM D2434
Thermal conductivity, dry ($W \cdot m^{-1} \cdot K^{-1}$)	0.25	Cylindrical Heat Source
Thermal conductivity, moist ($W \cdot m^{-1} \cdot K^{-1}$)	2.65	Cylindrical Heat Source

3.4 Concrete model pile

To determine the various mechanical properties of the concrete pile, a series of cylinders were cast along with the casting the model pile. These samples were cast in two ways (1) concrete with an embedded U-shaped tube, (2) concrete only. Casting concrete samples with embedded PVC tubing consider the loss of strength and stiffness compared to the homogenous mold. Table 3-3 presents the mechanical and thermal properties of the concrete used in thermal performance tests. The embedded tubing resulted in a compressive strength reduction of 2.76 MPa (≈ 400 psi) on average.

Table 3-3 **Mechanical and thermal properties of concrete at 28 days**

Compressive strength without tubing in MPa (psi)	44 (6,389)
Compressive strength with tubing in MPa (psi)	40.94 (5,939)
Elastic modulus in MPa (psi)	29730 (4,312,000)
Poisson's ratio	0.11
Thermal conductivity (W/mK)	1.4
Specific Heat (J/Kg/C)	1000

Surface roughness of the pile was also measured along several representative sections of the precast concrete in this study. Due to size restriction each section could not be more than 1 cm. Pile-soil interface can be divided into two groups: perfectly smooth or perfectly rough (Basu *et al*. 2011). Slip failure along the surface of the pile is the dominant failure for perfectly smooth interface. Perfectly rough interface creates shear bands near the vicinity of the pile interface. Normalized roughness R_n which represents the pile interface condition is calculated by dividing the maximum roughness of the pile surface R_{max} by the mean particle size of the soil (D_{50}). R_{max} obtained from optical profilometry equal to 20 μm (Figure 3-13). As mentioned earlier D_{50} of for the F50 Ottawa sand used in this study is 0.25 mm. Therefore, R_n value equal to 0.08. Based on the R_n value the pile-soil interface can be considered as a perfectly rough interface (Uesugi and Kishida 1986, Uesugi *et al*. 1988, Lings and Dietz 2005, Basu *et al*. 2011). Therefore, critical state friction angle (31.8°) can be considered as an interface friction angle for perfectly rough pile-soil interface.

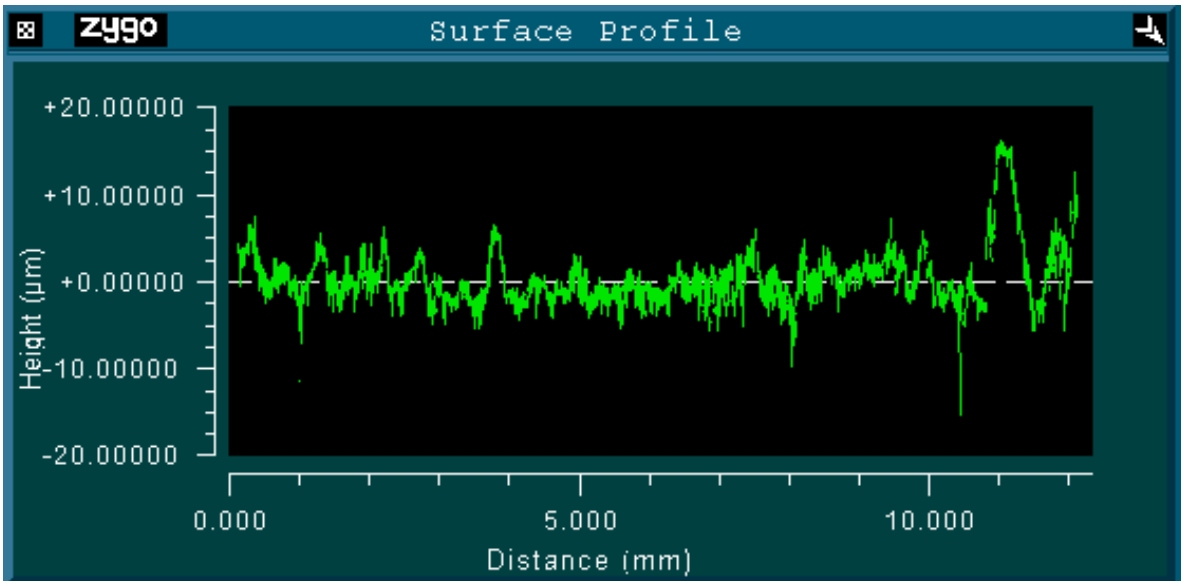

Figure 3-13 **Surface roughness profile for the concrete model pile**

3.5 Instrumentation and data acquisition

3.5.1 Thermocouples

To investigate the thermal performance of the geothermal pile, soil temperature was monitored at 94 locations inside the sand deposit as well as at the inlet and outlet fluid points. Type T thermocouples which can measure temperature range of −200°C to 350°C with an accuracy of ± 0.5 °C were selected in this research. Type T thermocouples have a pair of twisted wires: one copper and the other constantan (copper-nickel alloy). Thermocouples has two ends, hot ends which is basically a twisted of two different wires and cold ends which is left unpaired. The cold end should be connected to the data acquisition (DAQ) system. As mentioned earlier temperature increments was monitored at 94 locations within the sand bed, on pile surface, tank boundaries and within the circulation tube. Figure 3-14(a) shows the layout of the thermocouples locations on a plane passing through the pile and the circulation tube (hereafter referred to as XZ plane). With the selected layout, we could monitor the warm side and cold side of the pile. Between these two extreme sets of temperature records (warm side and cold side), temperature was also measured at different points on the YZ plane. Figure 3-14(b) also shows the layout of thermocouples locations on a plane perpendicular to the plane containing the circulation tube (hereafter referred to as YZ plane).

From 94 thermocouples 17 locations were selected along the pile surface, eight thermocouples at each side and one at the pile base. Six thermocouples were placed at the tank boundary and another six thermocouples were placed at the top of the sand bed. The rest of 94 thermocouples were placed within the sand bed. Besides than these 94 locations, temperature was also recorded at the fluid inlet and outlet points. Having temperature readings at the inlet and outlet points is necessary to quantify the heat exchange efficiency of the system. All of the 96 thermocouples were connected to a total of six NI 9213 modules. Each of these modules is capable to acquire 16

differential voltage inputs at an aggregate data acquisition rate of 75 samples per second per channel (S/s/ch). All the modules were connected to the NI cDAQ 9178 chassis. Temperature measurements were collected, displayed, and logged in real time at a rate of 0.1 Hz using data collection software written in LabVIEW 2011 (National Instruments 2013) (Kramer 2013, Kramer and Basu 2014a, 2014b, Kramer *et al*. 2014).

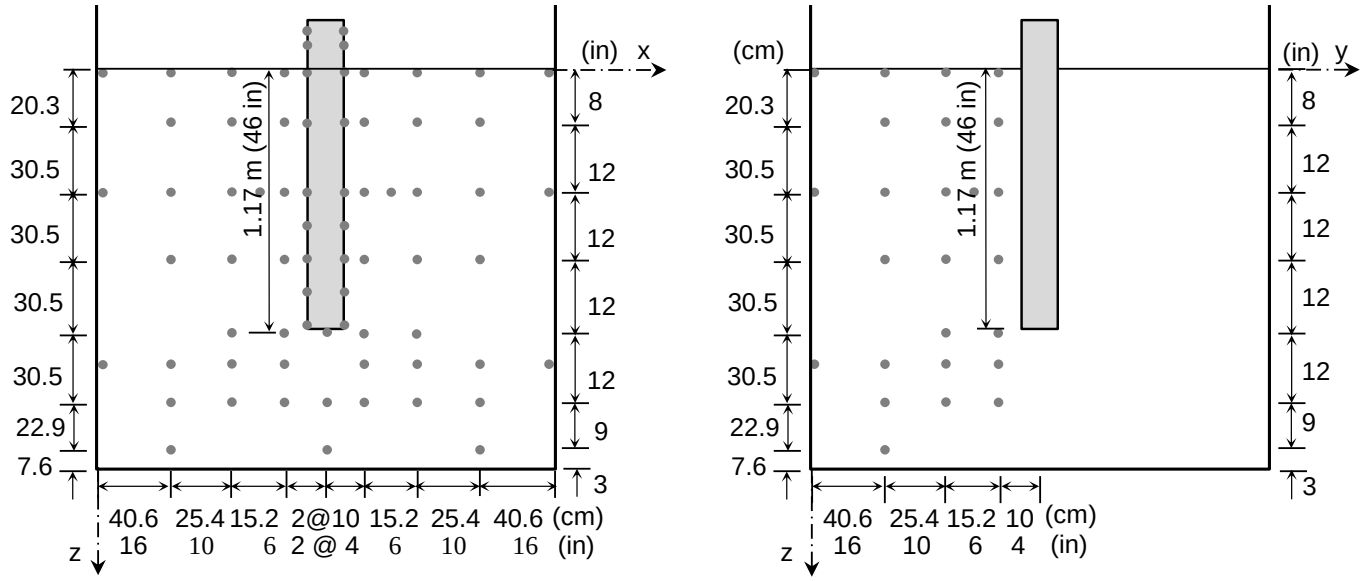

(a) (b)

Figure 3-14 **Temperature measurement locations: (a) XZ plane and (b) YZ plane**

3.5.2 Load cell and displacement sensor

Omega LCM401-2.5K load cell was placed between the pile helmet and load cylinder to control the amount of mechanical loading applied by a hydraulic jack (Enerpac RC-55). The load cell was connected to an NI 9205 module housed in the same NI cDAQ 9178 chasis which housed the thermocouples modules. The load cell module has an aggregate sampling rate of 250×103 S/s. The data was gathered, logged, and displayed in real time at an acquisition rate of 2 Hz using the Labview code (Kramer 2013, Kramer and Basu 2014a, 2014b, Kramer *et al*. 2014).

Two linear variable differential transformers (LVDTs) were used to monitor top and bottom displacements of the pile. Both LVDTs used in this research were Omega LD621-100. The LVTD can measure the displacement up to 10.6 cm. Both LVDTs were connected to the NI 9205 which was previously housed for the load cell. One of the LVDTs, that was used to measure the pile head displacement, was fixed to the load cylinder and its tip was exactly placed on the pile helmet. A telltale rod was used to measure the pile base displacement. The other LVDT was attached to the telltale to monitor the displacement of the telltale. The telltale was composed of a 0.3175 cm steel rod that lies inside a plastic tube. The plastic tube was used to separate steel rod from the concrete. The displacement of the rod is independent of the pile compression and it only

shows the pile base settlement. However, the LVDT at the top of the pile measured both pile settlement and pile compression.

3.5.3 Labview code

Data logging software was developed in Labview using a graphical interface (GUI) to present the results in real time (Kramer and Basu 2014a, 2014b, Kramer *et al*. 2014). The program developed in Labview is capable to acquire and process the data in parallel. Aggregate acquisition rates can be as fast as 75 samples per second per channel (S/s/ch). However, considering a couple of days for a time scale of the thermal performance tests, samples were acquired at a rate of 2 S/min/ch. Figure 3-15 shows a temperature contour which was presented by Labview code at both XZ and YZ planes. Linear approximation was used to estimate the temperature for the nodes between the thermocouple locations.

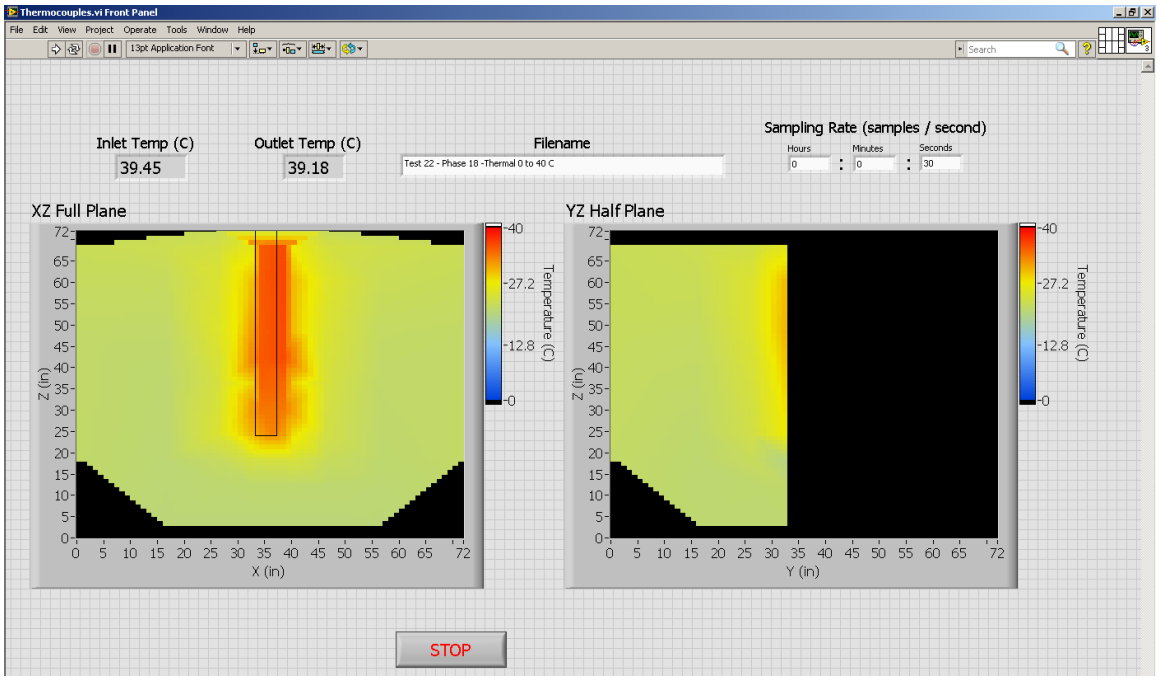

Figure 3-15 **Temperature contours displayed by the developed labview code**

Model pile displacements and the axial load were also collected and displayed on the same GUI. The GUI shows three graphs, (1) axial load versus a real time, (2) pile head and pile base displacement versus time, (3) pile head displacements versus the axial load. Figure 3-16 shows these three graphs in a single screen shot.

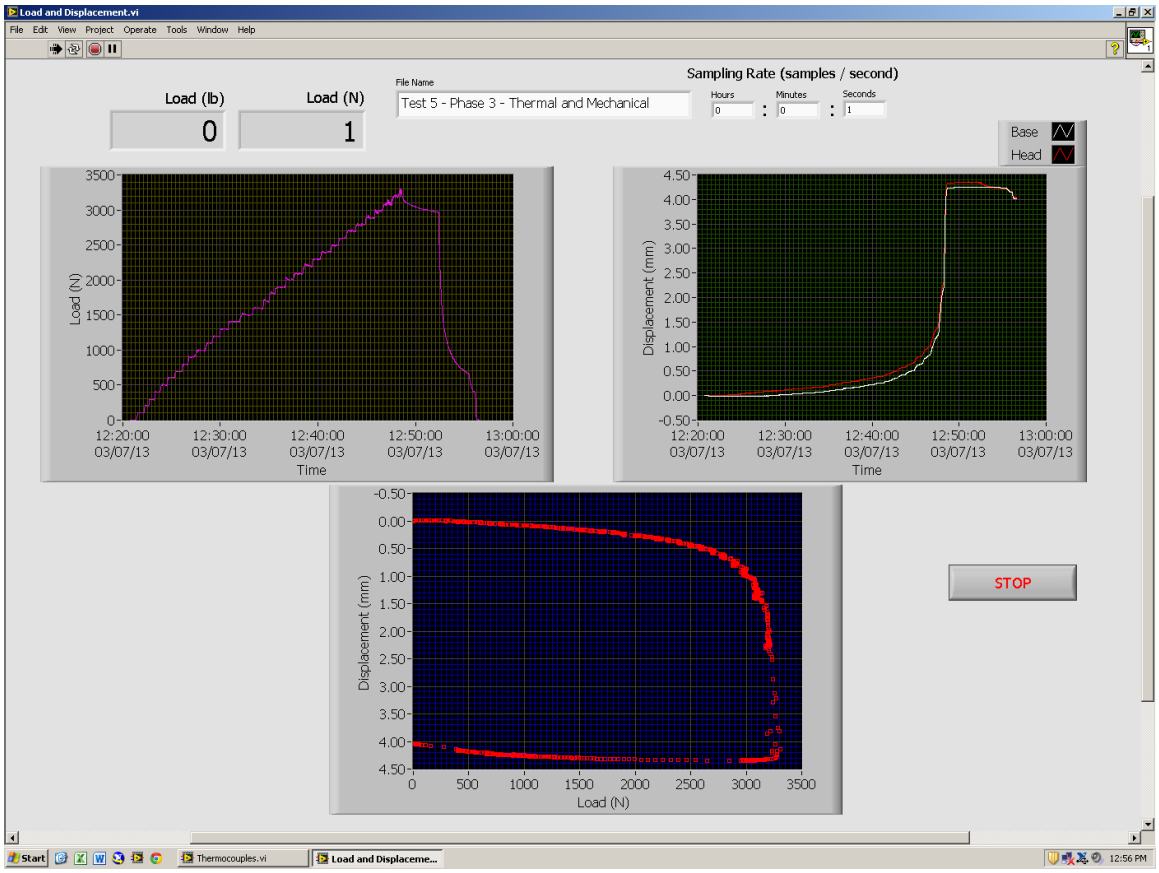

Figure 3-16 **Axial load and pile head and base displacements displayed by the developed labview code**

For data acquisition aggregate sampling was used to reduce the noise. The rate used to acquire that load-displacement data was 1 S/s/ch. However a given data was actually the average of 100 measurements made at a rate of 1000Hz. Since, very high data acquisition rates were required; a producer-consumer architecture was used to separate data acquisition from display and logging (Kramer 2013, Kramer *et al*. 2013). The developed GUI code has two major benefits, (1) the load versus time graph would confirm that the loading steps were consistent, (2) the load displacement curve shows the start of plunging behavior that could be used as an indicator to terminate a load test.

3.6 Results

3.6.1 Thermal performance

Inlet fluid temperature was kept constant during each thermal loading test using a temperature-controlled water bath. Heat carrier fluid was circulated from the constant temperature water bath to the tubing embedded within the model geothermal pile. As mentioned in previous section, temperature increments were measured at 94 locations within the soil and along the pile. The thermal conductivity and specific heat capacity of the sand, and the concrete pile, are assumed to be constant for all tests under dry condition. Same assumption is valid for the saturated

condition. Considering this assumption, the effect of different parameters such as the circulation velocity and imposed thermal gradient, can individually be investigated. The room temperature was kept constant at 19°C. Since, soil and pile were at room temperature, there was a slight temperature gradient in the tank due to room temperature variation. Figure 3-17 shows the variation of soil temperature deposit before start of a test.

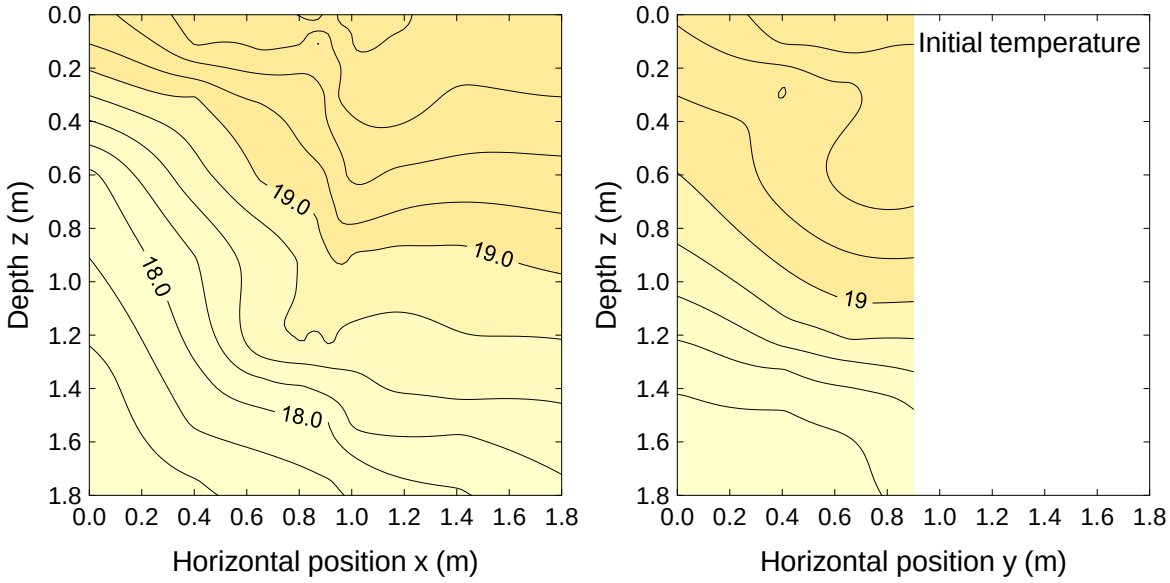

Figure 3-17 **Initial temperature gradient: (a) in the XZ plane (b) in the YZ plane**

Thermal performance tests were first performed under dry condition. Fluid inlet temperature of the first test, which was considered as a base case, was T_{in} = 39°C. The inlet fluid temperature was 20 °C higher than the initial soil temperature. The fluid was circulated at a flow rate of 1.34×10-5 m3/s (≈ 0.8 L/min) which corresponds to a linear average flow velocity v = 0.11 m/s. In the next section it is demonstrated that it is better to use higher circulation flow rate (velocity). Higher circulation flow rate yields higher power output. The flow rate and entrance temperature were maintained throughout a test.

Test conditions for all of the thermal tests performed under dry condition are presented in Table 3-4. Note that the TPH4 was started with non-uniform temperature in the test bed. This test was started right after TPC1 had finished, and thus the initial condition for TPH4 was different from that of TPH1. In the beginning of TPH4, pile temperature and temperature of soil in the immediate vicinity of the pile was approximately equal to 5°C and the constant inlet fluid temperature T_{in} for TPH4 was equal to 20°C.

Temperature contours obtained from the first test (TPH1) at different time steps are presented in Figure 3-18. Most of the heat flow occurred in the radial direction. The radial heat conduction was also showed in several researches (Laloui *et al*. 2006 and Man *et al*. 2010). As it can be seen in this figure, after 7 days of thermal performance test at a depth of 2B (= 20 cm; B is the diameter of the pile) below the pile base temperature increment is negligible. However temperature increment at the mid depth and at r = 2B (radial distance =2B) was 11.3°C.

Significant heat loss was also observed at the ground surface of the sand deposit. Thus, we can conclude that there is a significant convective heat transfer from the soil surface.

Table 3-4 **Thermal performance test matrix**

Test name	Heating vs cooling	Initial temperature gradient $\Delta\theta$ (°C)	Circulation velocity v (m/s)
TPH1	Heating	+20	0.11
TPH2	Heating	+20	0.33
TPH3	Heating	+20	0.66
TPH4	Heating	+15	0.11
TPC1	Cooling	−20	0.11
TPC2	Cooling	−20	0.66
TPSCH	Cooling followed by heating	−20 and +35	0.66

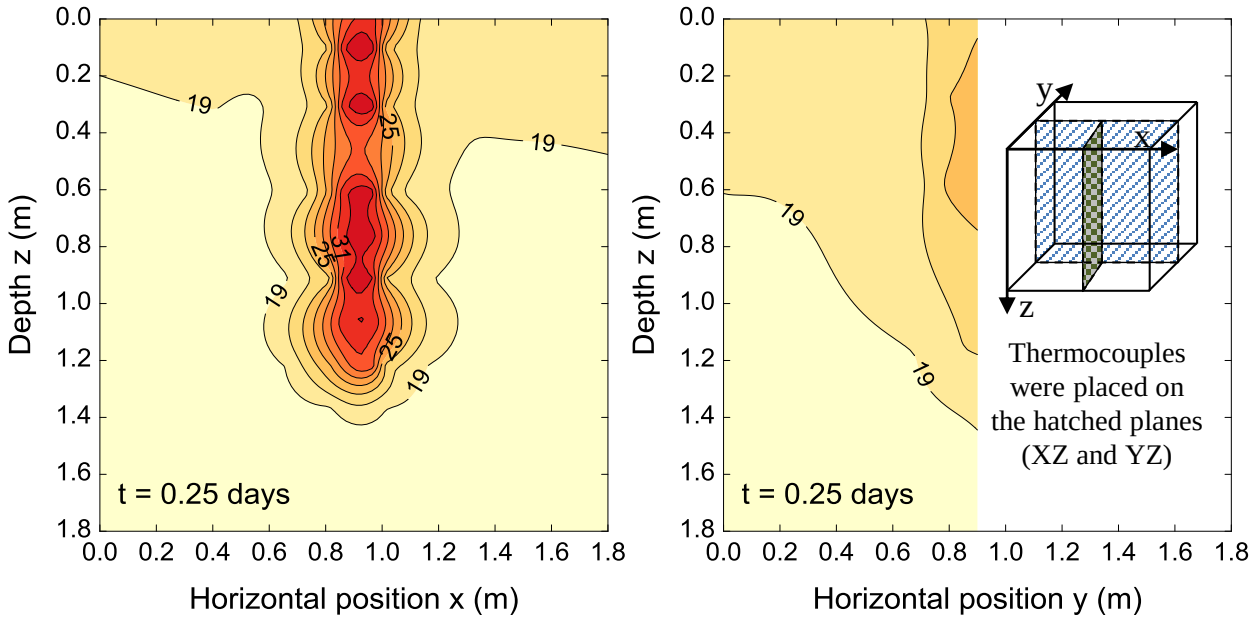

Figure 3-18 (a)

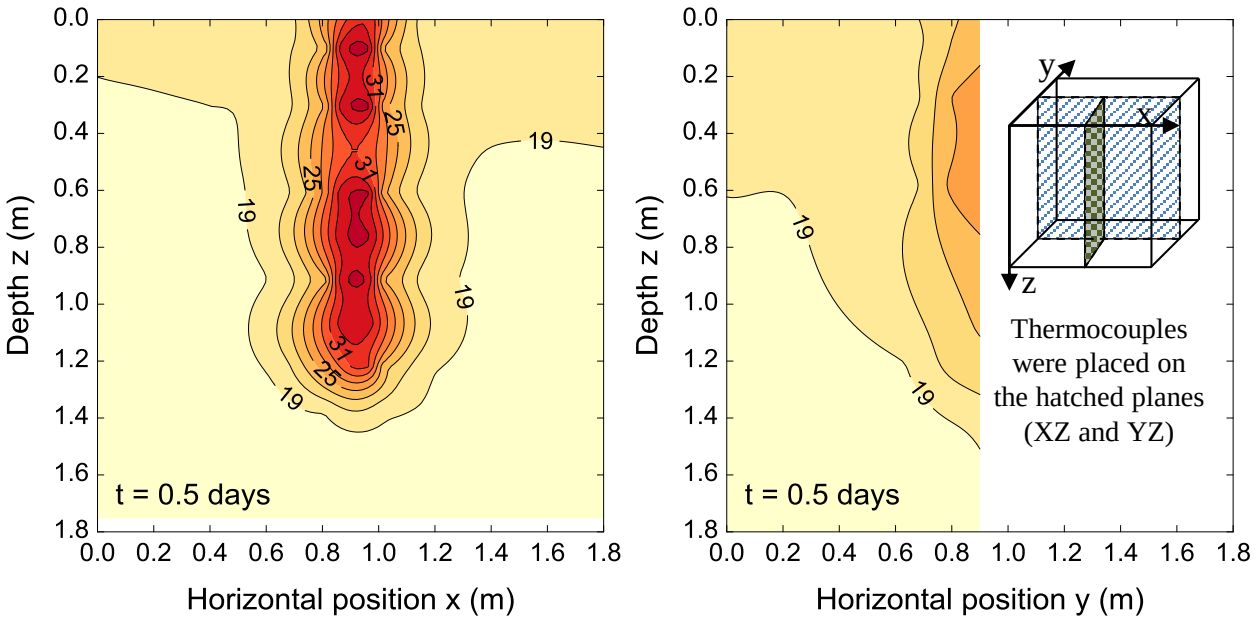

Figure 3-18 (b)

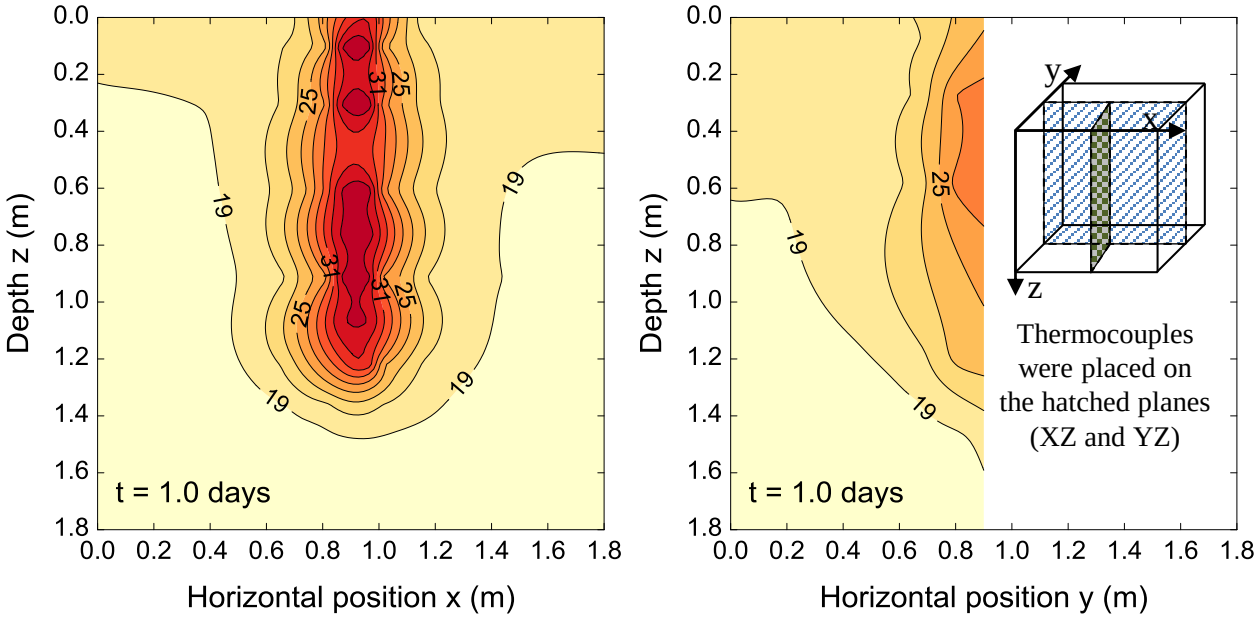

Figure 3-18 (c)

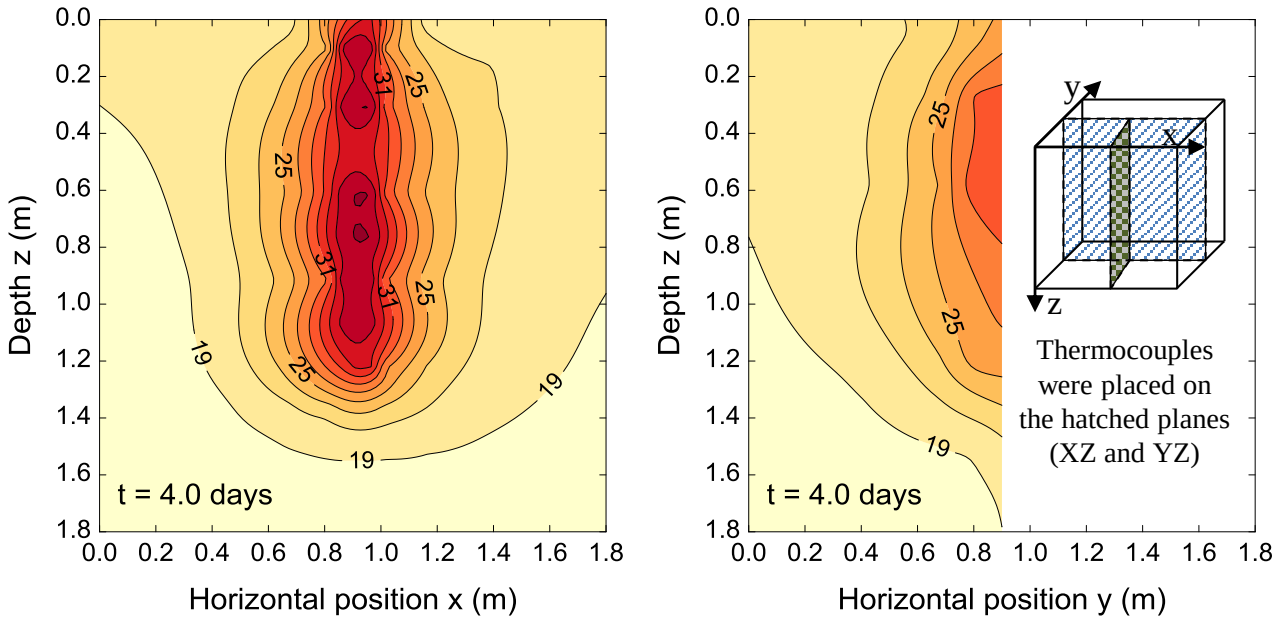

Figure 3-18 (d)

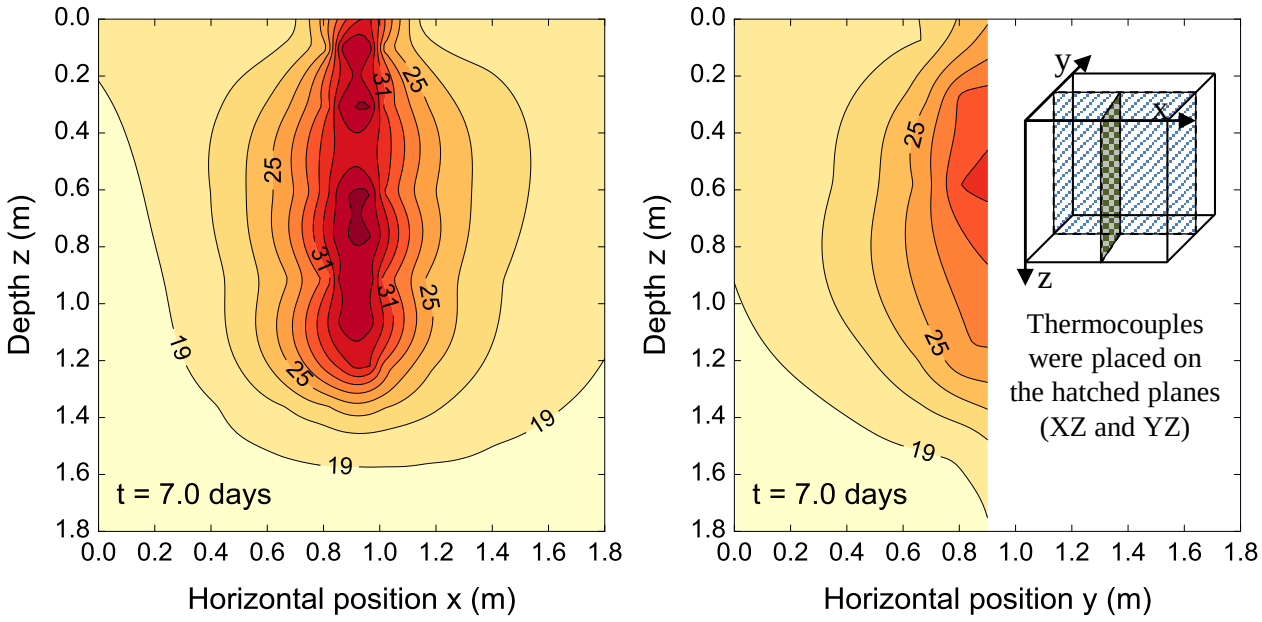

Figure 3-18 (e)

Figure 3-18 **Temperature evolutions (contours) at different time steps**

Thermal influence zone was also identified in this research. It will be showed later in the numerical model section that the soil temperature beyond the thermal influence zone would not be changed even after 2 months of operation. Soil temperature increments along the depth at $r = 2B$ at different time steps are presented in Figure 3-19. As it can be seen in this figure, temperature at r = 10 cm increases by 9 °C in 2 days and in the following 5 days (at t=7 days) it only increases by 2 °C. This shows a drastic change near the geothermal pile within a short time

after the start of the test and the temperature reaches to a somehow steady state condition in a couple of days.

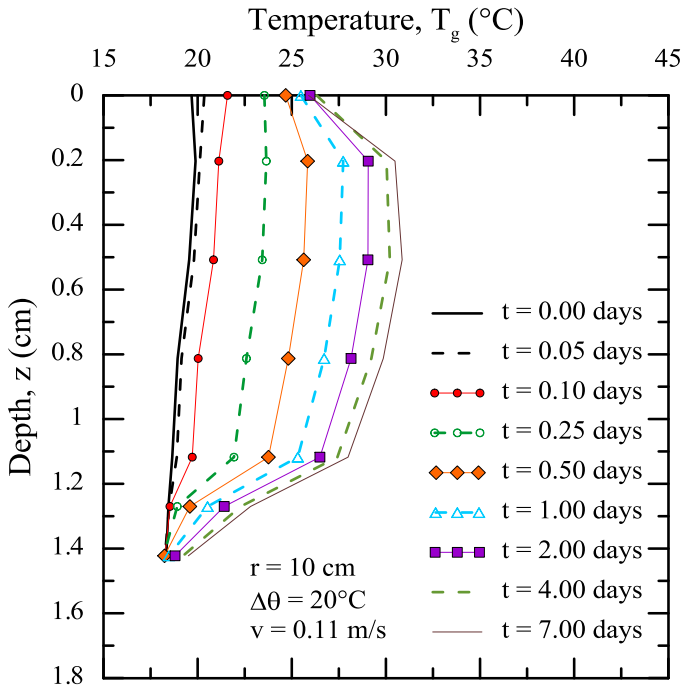

Figure 3-19 **Soil temperature T_g measured at different thermocouple locations at $r = 2B$**

As heat dissipated from the heat source into the surrounding soil, a zone of thermal influence was evident within the soil. Soil temperature will not significantly change (less than a degree) beyond this zone. Temperature evolutions ΔT_g (under dry condition) at different radial distances with both real and normalized time (expressed as Fourier number Fo) for two different tests (one heating and one cooling) are presented in Figure 3-20. At radial distances farther from the pile the amount of time to experience a change in temperature is higher. Soil temperature at r=0.5B (= 5 cm) away from the pile increases in only 15 minutes after the heat transfer started. Whereas, for the same test, same amount of temperature increments for a point at a distance of 10B (= 50 cm) away from the pile take 24 hours. Moreover, it could be confirmed that (as expected), with all other parameters identical heating ($\Delta\theta$ = 20°C) and cooling ($\Delta\theta$ = −20°C) produce identical but opposite thermal responses in soil.

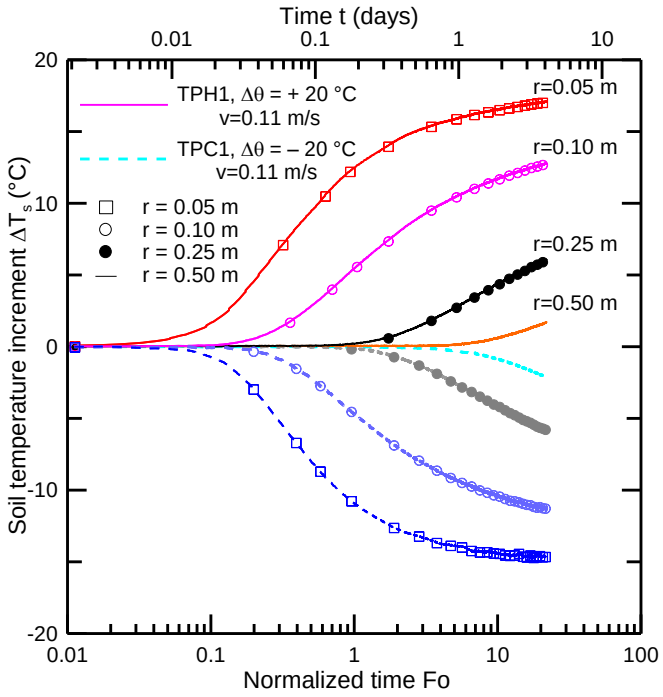

Figure 3-20 **Temperature evolution with normalized and real time**

During the seven days of thermal performance test, only the zone near the geothermal pile reached to a nearly steady state condition. However, the pile-soil system was still in a transient heat flow condition. By the end of seven days, soil temperature at the tank boundary did not change, so there was not any heat loss from the tank boundaries during the test duration. In real condition there is not any side boundary and, therefore, heat would not dissipate to the outside of the media, except possibly from the surface. Therefore, all the thermal performance tests were stopped while heat reached to the tank boundary. Figure 3-21 also shows that the inlet side of the pile was slightly warmer than the outlet side of the pile at all measurement points.

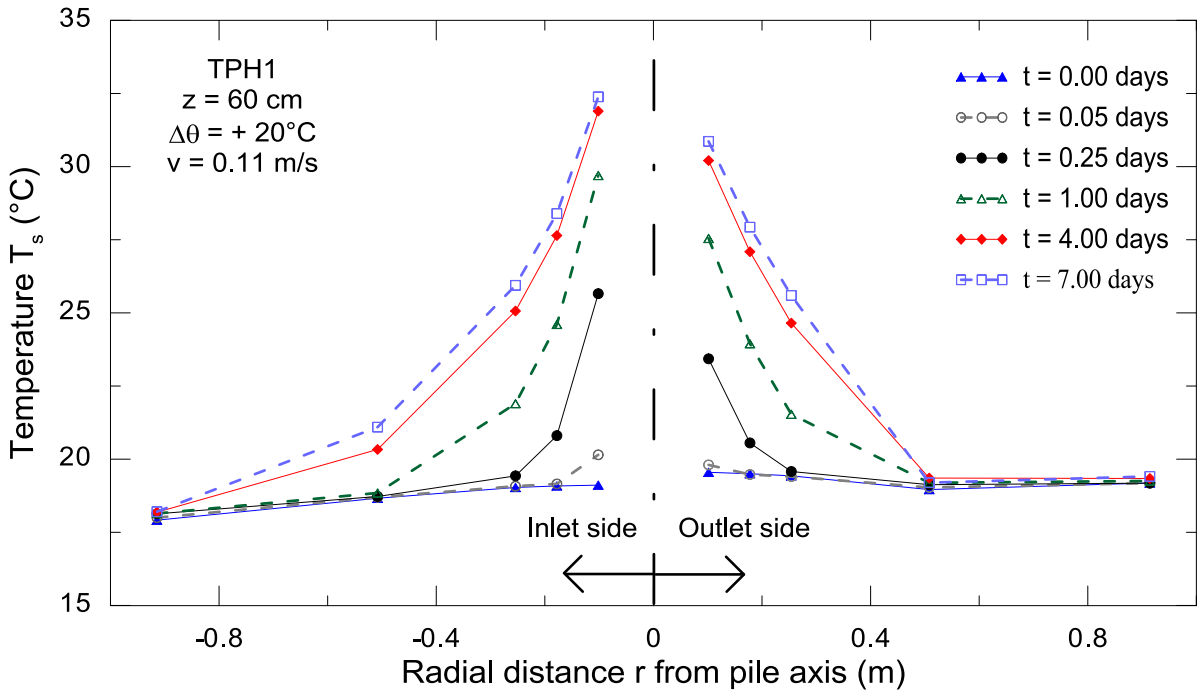

Figure 3-21 **Radial distribution of Soil temperature evolution**

Fluid temperatures at the inlet and outlet points of the circulation tube were recorded during the test. The amount of power output can be calculated from the temperature difference ΔT_f between these two points. Circulation flow rate is one the key parameters which can change the power output of the system. To study the effect of circulation flow rate (or circulation velocity) on the efficiency of the model geothermal pile, three different circulation flow rate (three different thermal load tests) were considered under dry condition. The circulation velocities of these tests were respectively, 0.11 m/s (the base case), 0.33 m/s and 0.66 m/s.

The energy output E over a certain period of heat transfer through the model geothermal pile can be viewed as a representation of thermal power output P (energy extraction/rejection rate) (or heat transfer efficiency) of the pile. Mathematically,

$$P = \dot{m} C_{pf} \Delta T_f = \rho_f v A C_{pf} \left(T_{in} - T_{out} \right) \qquad (3\text{-}4)$$

where $\dot{m}$ is the mass flow rate of the circulation fluid, C_{Pf} is the specific heat capacity of the circulation fluid, and ΔT_f is the fluid temperature difference between the inlet and outlet points. The mass flow rate $\dot{m}$ can be determined by multiplying volumetric flow rate by the density of the circulation fluid. As Figure 3-22 shows an increase in the flow rate of the circulation fluid increases the power output.

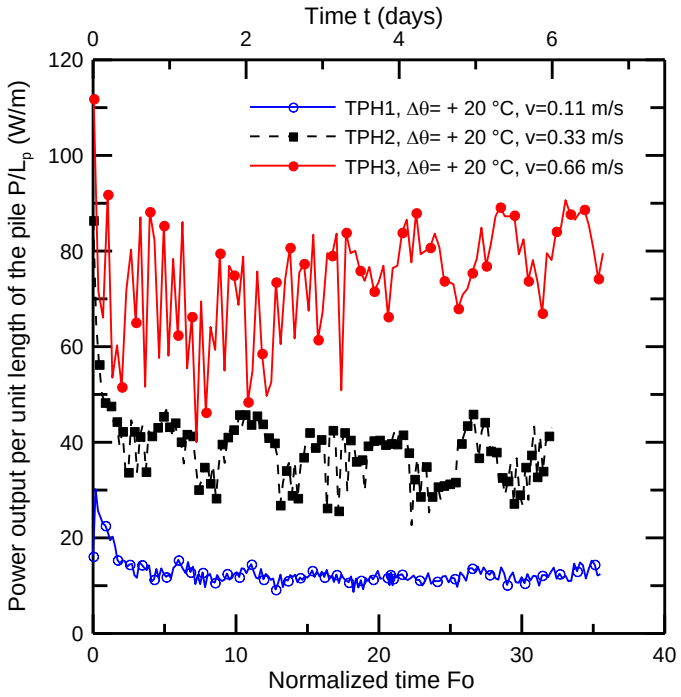

Figure 3-22 **Geothermal power output obtained from a mode pile for different circulation flow rate**

There are both daily short-term variations as well as long-term seasonal variations in air temperature. Therefore, cyclic thermal loads should be investigated to predict power output obtained from the real geothermal pile. Soil surrounding these piles would be subjected to heat extraction during winter followed by heat rejection during summer months (or heat extraction during the night followed by heat rejection during the day). To investigate the effect of thermal cycle loading on heat transfer performance of the geothermal model pile, a cyclic load test (test TPSCH) was performed. Deicing the bridge decks starts in winter and the system can be continuously working to reject heat into the ground and recharge it in future. To model the real thermal loading cycles, heat was first extracted from the soil ($\Delta\theta = -20$°C, $T_{in} = 0$ °C) for seven days and then immediately heat extraction phase was started. Results obtained from the cyclic test showed that thermal efficiency of the system for a short duration in the initial part of the second phase of thermal loading was increased by 30% compared to that obtained from the first half of thermal loading with $\Delta\theta = -20$°C (Figure 3-23). This occurred due to the presence of high thermal gradient ($\Delta\theta = 35$°C) at the onset of thermal loading reversal and the availability of additional thermal storage in the soil immediately after the heat extraction phase. However, by depleting the initial thermal potential, the system approached similar steady state efficiency for both phases of thermal loading. Real life situation may also include some intermediate thermal loading phases (or even no operation at all) during intermediate seasons (e.g., late spring and early fall) in between the extreme thermal loadings during winter and summer or during the day and night. Such intermediate phases of operation (or temporary pause in thermal operational) affect heat transfer efficiency of the system for a short period of the time. Numerical simulation also showed the same trend.

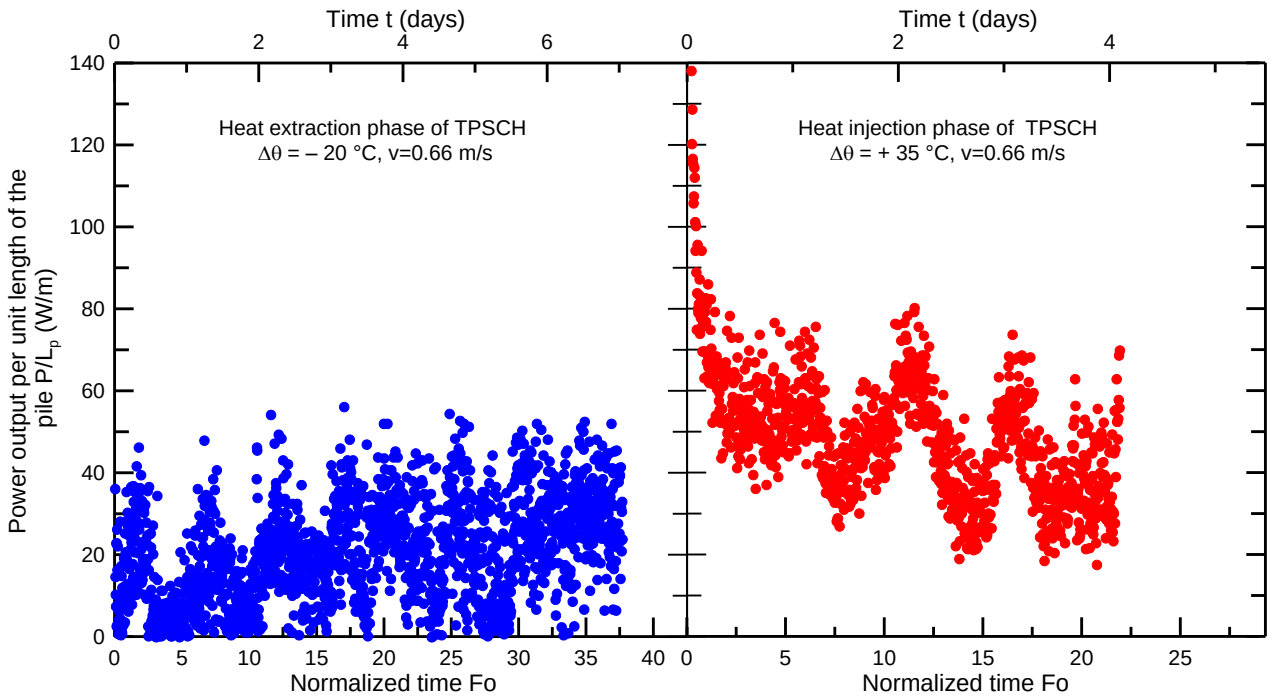

Figure 3-23 **Effect of sequential heat extraction and rejection on geothermal power output**

Mechanical load tests were performed on the model pile before and after the heat exchange operation. Free displacement condition was maintained at the pile head and pile head and base displacements were measured continuously during the load tests. A load increment of 0.1 kN was used for all tests. Figure 3-24 shows a small increase in limit load after the thermal load was applied for seven days. The initial pile head stiffness decreases after the thermal loading.

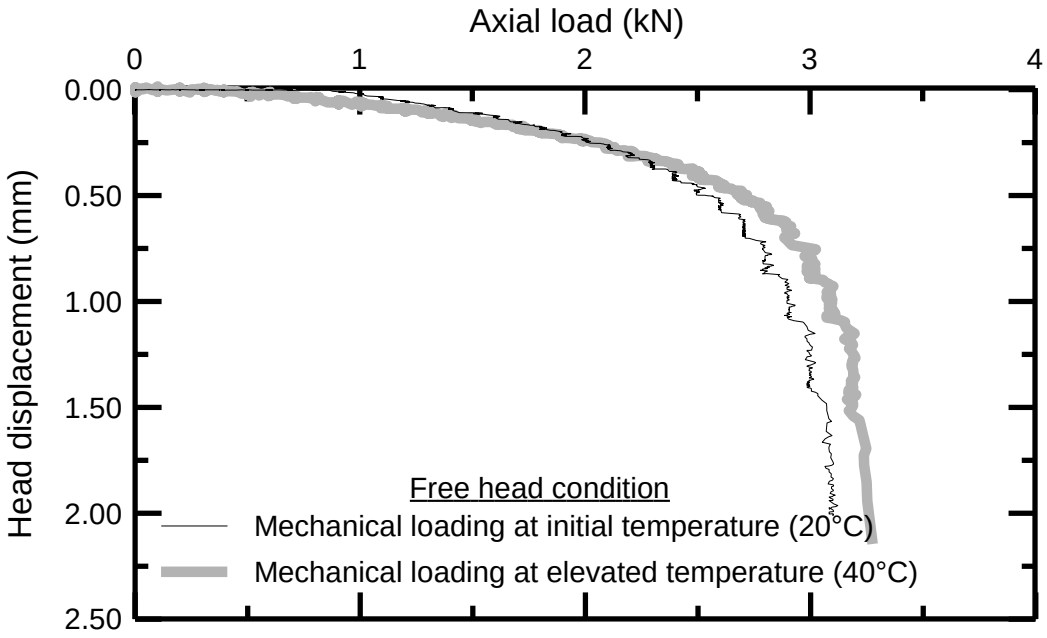

Figure 3-24 **Axial load-displacement behavior of the model geothermal pile before and after thermal loading**

3.7 Observations from thermal tests

A number of observations were made based on the data recorded during a series of thermal load tests on the model geothermal pile. It was observed that heat flow through geothermal piles occurs primarily in the radial direction. The heat dissipation raises the temperature of the soil in the vicinity of the pile within a 'thermal influence zone' that expands with time. When designing geothermal piles, particularly if they are to be installed as part of a pile group, the thermal efficiency of these piles will reduce if the zones of thermal influence overlap with one another.

Results show that increasing the flow rate of the heat carrier fluid will increase the energy output of the pile. The geothermal piles have high initial energy outputs that approach steady-state values as the soil surrounding the pile begins to change temperature. The steady-state energy output values should be used for design because such values represent long-term thermal behavior. However, running heating and cooling cycles in series does provide an increased short-term efficiency.

The model geothermal pile was subjected to a series of mechanical load tests at ambient conditions as well as during thermal loading. During all mechanical load tests, plunging of the pile, that signifies typical limit state behavior, was observed. Based on interpretation of the pile load tests performed, it appears that both limit- and ultimate-state capacities of geothermal piles are likely to be affected by thermal loading.

4. Laboratory-scale tests on bridge deck (concrete slabs)

To test the viability of a ground-source bridge deck deicing system, a field test setup was constructed at the Virginia Tech Geotechnical Research Facility. The setup consisted of a small-scale bridge deck connected to geothermal piles installed in the field. There were several purposes of the field test. The first of which is to provide proof of concept testing to demonstrate that ground-source bridge deck deicing is a viable concept. The second reason was to provide data for numerical model calibration.

4.1 Field test setup and construction

The field test setup consists of a total of five micropiles, four of which are equipped with circulation loops along the full pile length for heat exchange. Test piles, 25-cm (10 inches) in diameter, were installed to a depth of approximately 30.5 meters (100 feet) as part of a previous research project (Abdelaziz 2013). The energy piles are instrumented to measure strains and temperatures at about every 3m (10ft). The piles are embedded in a silty sand, which extends to a depth of 12.2m (42ft), after which is a weak shale layer. There are also four observation boreholes installed around the piles that can measure temperatures in the ground. The plan view of the pile and borehole locations is shown in Figure 4-1. Table 4-1 provides the depths at which temperature and strain (if applicable) were recorded in each of the boreholes and piles.

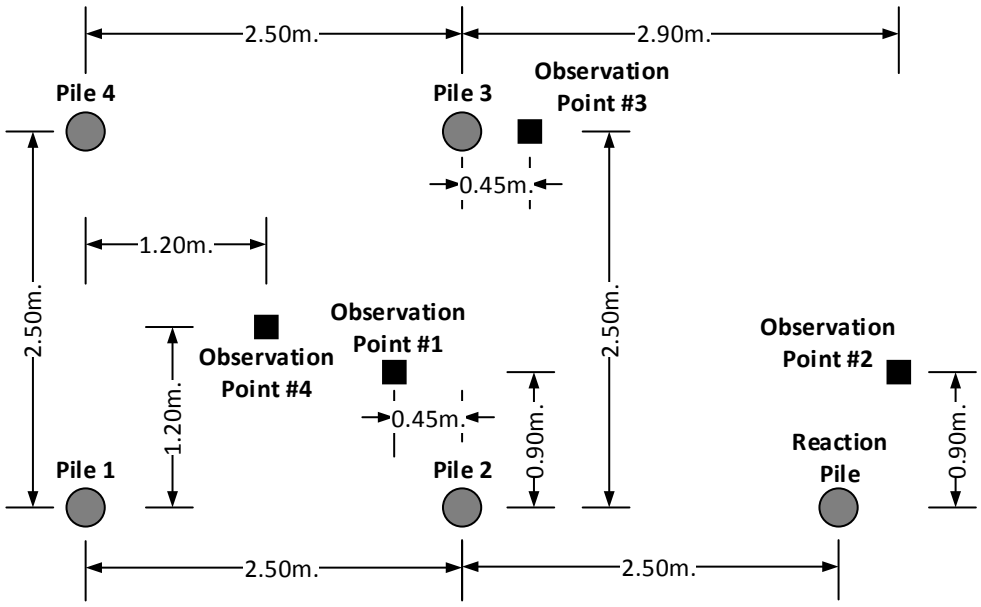

Figure 4-1 **Plan view of the energy pile and borehole locations**

Table 4-1 **Locations of recorded measurements in the energy piles and ground**

Location	**Depths Measured (m)**
Piles 2 and 3 (Temperature and Strain)	3.0, 6.1, 9.1, 12.2, 15.2, 18.2, 21.3, 24.3, 27.4, 30.4
Observation Points 1 and 2	3.0, 6.1, 9.1, 12.2, 15.2, 18.2, 22.8, 27.4, 30.4
Observation Point 3	3.0, 6.1, 10.6, 15.2
Observation Point 4	3.0, 6.1, 9.1, 12.2, 15.2, 18.2, 21.3, 24.3, 27.4, 30.4, 33.5, 36.5

A prototype 2.4 m x 3.0 m (8 ft. x 10 ft.) bridge deck was constructed as shown in Figure 4-2. The doubly reinforced 25 cm (10 inch) thick slab is elevated from the ground to simulate heat loss from the bottom face similar to a bridge deck. The test slab is divided into two 1.2 m x 3.0 m (4 ft. x 10 ft.) sections with an insulated separation in between. A 5 cm (2 inch) thick clear concrete cover is present on top of the upper level reinforcement. PEX tubes with 16 mm (5/8 inch) inner diameter (ID) are connected to the upper level reinforcement with 20 cm (8 inch) and 30 cm (12 inch) horizontal spacing in each section. Insulation has been added to the sides to simulate an adiabatic surface. The slab is heavily instrumented with 36 thermistors to monitor the variation of temperature in both slab sections at different horizontal and vertical extents near the tubes.

Figure 4-2 **Prototype bridge deck slab during construction to show the circulation tubes connected to the top level of rebar reinforcement.**

4.2 Experimental tests and results

Presented are the results from three experimental tests conducted during 2013 and 2014. They include two episodes during January and February 2014 of bridge deck heating and one episode of ground recharge during the summer of 2013. In all the experimental cases presented in this report, only one of the four energy piles (Pile 3 from Figure 4-1) was used.

4.2.1 Bridge deck heating

4.2.1.1 Experimental test #1

Blacksburg, VA experienced extremely cold weather during January 6-8, 2014 where the ambient air temperature dropped as low as -20^{o}C (-4^{o}F) at night. Though there was no precipitation during this period, the bridge deck deicing system was turned on to test the ability of the system to perform in extremely cold weather. In this test, the side of the bridge deck slab containing the 20 cm spaced circulation tubes was operated while the other side was left alone as a control. Figure 4-3 shows the temperatures recorded in the center at the surface of both slabs as well as the ambient air temperature during this period.

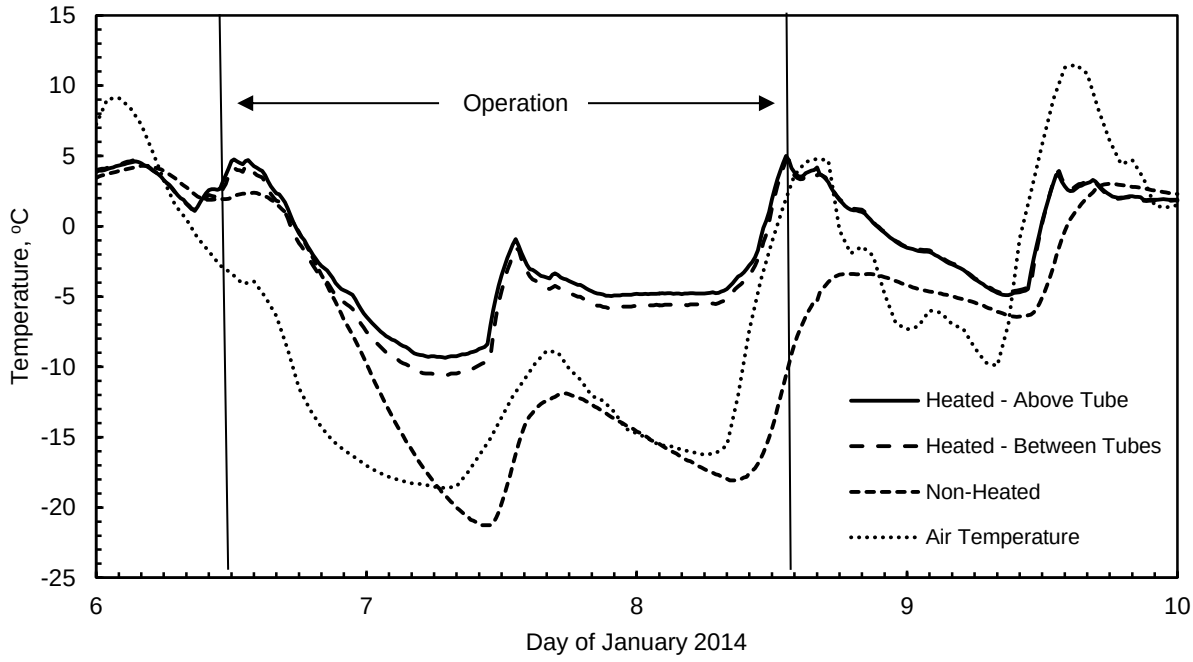

Figure 4-3 **Surface temperatures of the heated and unheated bridge deck slabs during bridge deck heating.**

From Figure 4-3, several observations can be made. The first is that the bridge deck deicing system was able to significantly heat the slab, causing the surface temperature of the heated slab to be as much as 15°C (27°F) higher than the unheated slab. However, despite the significant difference between the performances of the two slabs, the system was not able to keep the surface temperature of the heated slab above 0°C (32°F) meaning that if any precipitation were to accompany this extreme cold weather event, it would accumulate on the surface of the deck. It should be noted, however, that these extreme environmental conditions are well outside the range of those expected during normal operation.

4.2.1.2 Experimental test #2

Another test of the deicing system occurred on January 21, 2014. Beginning around 11AM and continuing until 4PM, approximately 2.0 cm (0.8 in) of snowfall occurred. The system was turned on in advance of the storm at 7AM. Figure 4-4shows the ambient air temperature, the temperatures of the surface of both the heated and unheated decks, as well as the cumulative amount of precipitation that fell. Note that the system was turned on when temperatures of both the heated and unheated surfaces of the deck were decreasing. After the beginning of operation, the heated deck surface temperature increased to approximately 4°C (39°F) by the time the snow started to fall and maintained a temperature above 4°C for the duration of the event. The

unheated deck maintained a temperature around 0°C (32°F). The system was able to keep the deck completely snow free for the entire duration of the test, whereas snow accumulated on both the unheated side and the control slab (Figure 4-5).

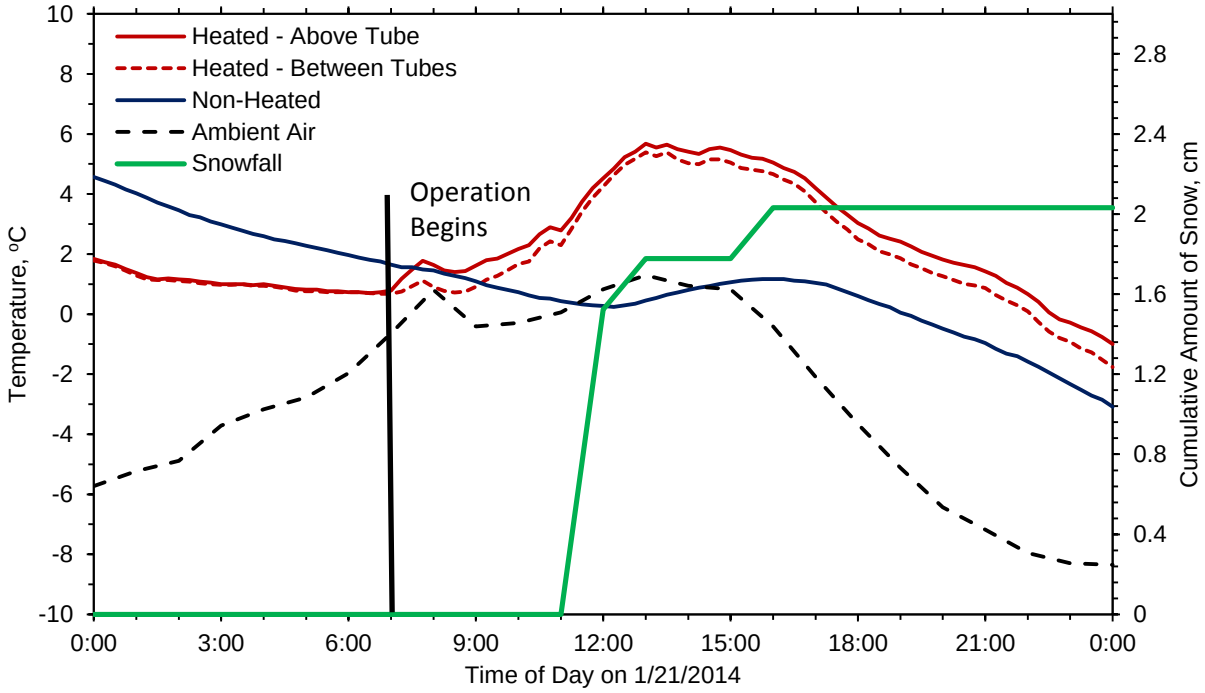

Figure 4-4 **Ambient air temperature, precipitation, and temperature at the surface of the heated and unheated decks during bridge deck deicing.**

Figure 4-5 **Photographs comparing performance of the heated deck vs. unheated deck (left) and the control slab (right).**

4.2.1.3 Experimental test #3

The capabilities of this system were tested again during a winter storm that occurred on February 21, 2015. This winter storm consisted of 16.5cm (6.5in) of snow that began falling while the

ambient air temperature was -13°C (8°F). Furthermore, these extremely cold temperatures (atypical for Blacksburg, VA) had persisted for several days, becoming as low as -20°C (-4°F). Thus, the slab was -18°C when the system was turned on the day before in anticipation of the storm. Again, only one half of the slab was operated. The surface temperatures of the heated slab, non-heated slab, and the ambient air temperature are shown in Figure 4-6.

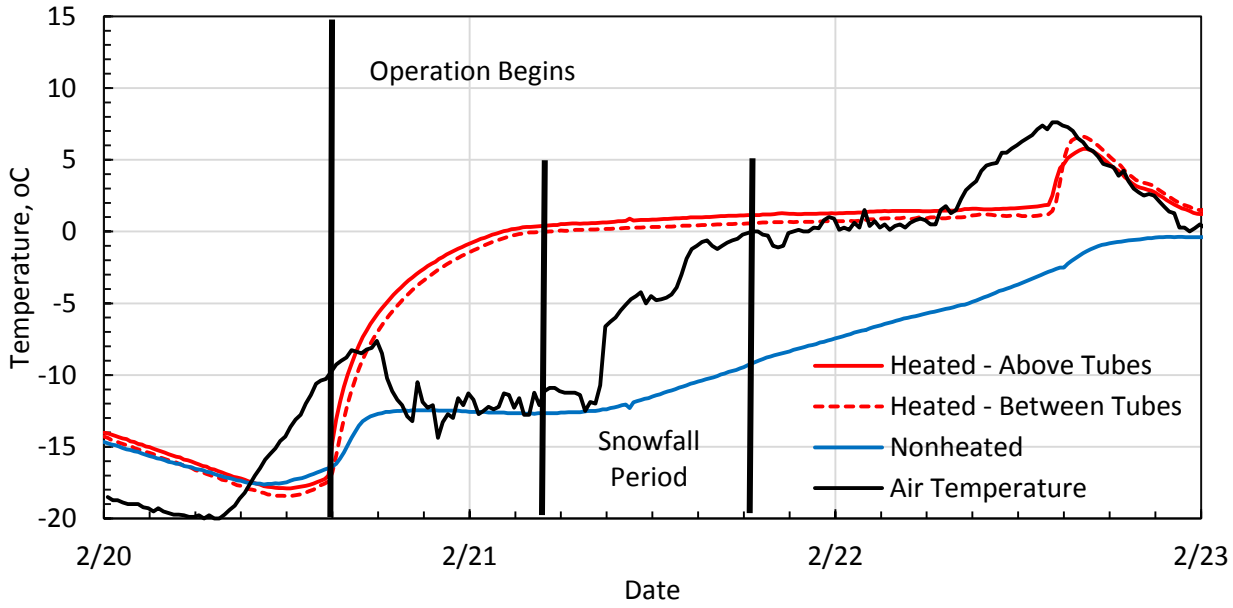

Figure 4-6 **Ambient air temperature and surface temperatures of the heated and nonheated slabs**

From this test, several observations can be made. The first of which is that using only the thermal energy from the ground as extracted from one energy pile, the system was able to heat the 20cm side of the bridge deck over 18°C before the start of the storm. This both exemplifies the capabilities of these systems and demonstrates how important it is to preemptively turn these systems on in anticipation of a storm so that they can adequately heat the deck. The second observation is that the surface temperatures of the heated deck were heated to values greater than 0°C. Though this system was not able to keep the deck completely free from snow, it was able to maintain a surface temperature greater than 0°C indicating that when combined with mechanical removal (which will be required anyway for 16.5cm of snow), a snow-free deck surface will result.

4.2.2 Ground response to bridge deck heating

Figure 4-7 displays the temperatures along the pile at different points during operation of the system during the experimental test presented in section 4.2.1.1. Though temperature was measured at 3m intervals, not all are shown to reduce clutter in the graphs. Rather, two locations from each soil layer (the silty sand and the shale) are plotted to develop the temperature profile vs depth.

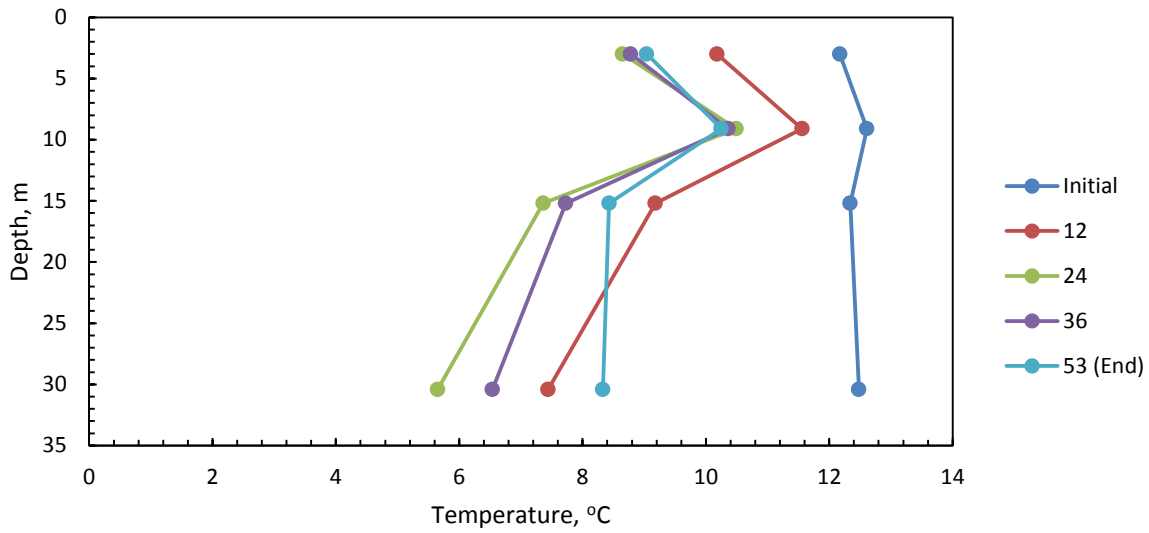

Figure 4-7 **Temperatures along the pile at different times during operations**

In Figure 4-7, one can observe that the starting temperatures are not the same for each depth indicating a non-uniform temperature distribution with depth in the ground. In fact, the 9.1 m depth is the highest of all observed temperatures and the 3.0 m depth is the lowest. This is expected as explained in Kusuda and Achenbach (1965). The depths closer to the surface will experience greater temperature variation as the mean ambient air temperature fluctuates throughout the year. As one moves deeper in the soil profile, the amplitude of temperature variations are not as great and are somewhat 'lagging' with respect to the temperatures in the soil above.

One can also observe that temperatures in the pile decrease after operation of the system begins, with the 30.4m depth exhibiting an almost 5^{o}C temperature decrease. Temperatures continue to decrease from 12 to 24 hours of operation, but here a distinction can be made. The two depths in the silty sand (3.0m and 9.1m) do not experience much, if any, temperature change after 24 hours whereas the depths in the shale (15.2m and 30.4m) experience temperature fluctuations after 24 hours. More will be explained later regarding this. For all depths except the 9.1m, the lowest temperatures in the pile occurred at 24 hours.

Figure 4-8 records the temperatures along the pile after the system operation has ended, thus characterizing the recovery period. For reference, it includes the initial temperature profile along the pile before operation began. The temperatures recover very quickly in the first 24 hours, with every location except the 3.0m depth recovering at least half of their temperature loss at the end of operation. The 30.4m and 15.2m depths recover the fastest and after 120 hours all depths except the 3.0m have been restored to their initial values.

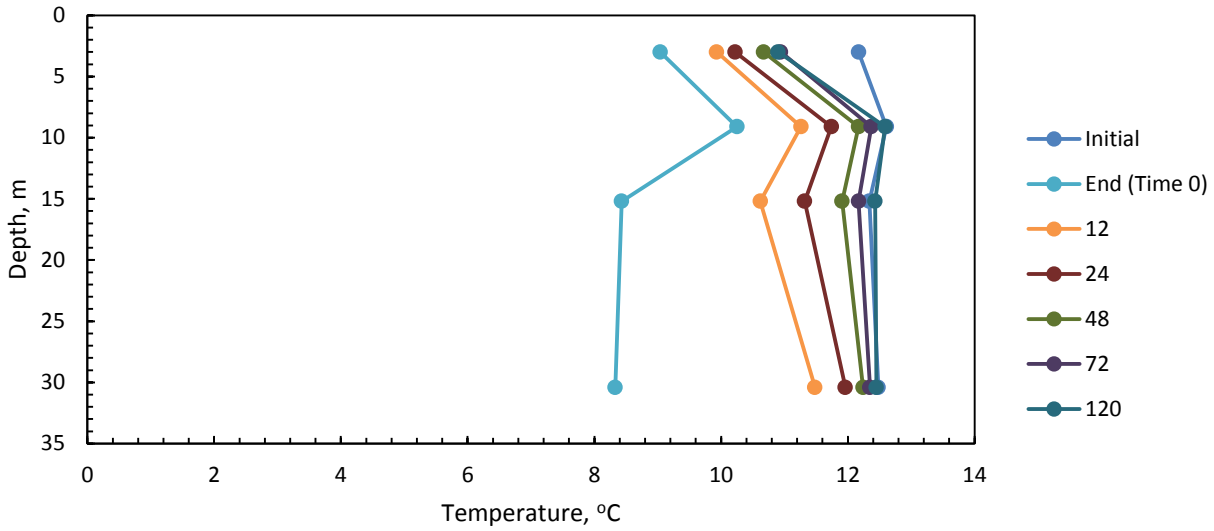

Figure 4-8 **Temperature vs depth along the pile for different instances in time after operation ended.**

To better understand how the temperatures in the pile and ground change over time, the temperature change in the locations mentioned previously were plotted vs time and are shown in Figure 4-9. The ground temperatures were recorded in Observation Well 1, which is a distance of 1.7 m (5.7 ft) away from Pile 3.

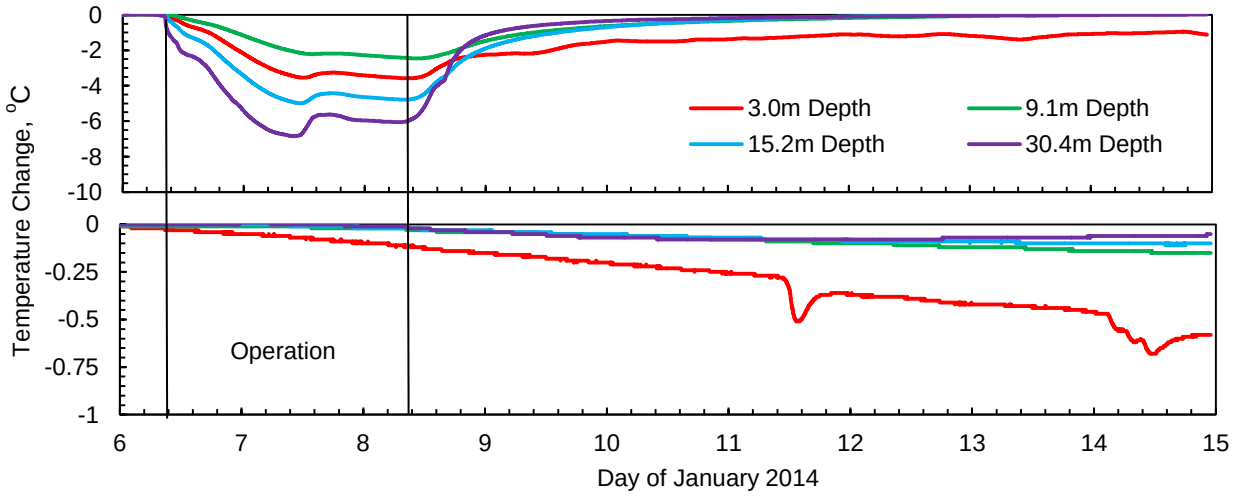

Figure 4-9 **Temperatures in the pile (top) and ground (bottom) as recorded at Observation Point 1**

After operation begins, the temperatures in the pile immediately decrease, as can be seen in Figure 4-9. This decrease, however, is not uniform with depth as seen in Figure 4-7. The 30.4 m depth experiences the greatest decrease in temperature, followed by the 15.2 m depth, the 3.0 m depth, and the 9.1 m depth. There are a couple of possible explanations. The first is that several of the sensors may be closer to the circulation tubes than the other. If the location of the sensors was the only factor, one would expect that once the pile reaches steady-state (roughly the period of time between day 7.5 and 8.5), the temperatures would be about the same value, and they are

not (Loveridge and Powrie 2014). Furthermore, after the system is turned off around day 8.5, the recovery curves (the portion of the curves that occur after day 8.5 when the system is recovering) are different.

To explain this, consider the site stratigraphy. The top 12 m (40 ft) of the site is a silty sand. Underlying the silty sand is a shale and the water table is located at this boundary. When giving design recommendations on geothermal systems, ASHRAE (2011) states that the thermal conductivity of light sand with 5% water is 1.0 to 2.1 W/mK (0.5 to 1.1 Btu/h-ft-^{o}F) whereas the thermal conductivity of wet shale is 1.4 to 2.4 W/mK (0.8 to 1.4 Btu/h-ft-^{o}F) meaning heat transfer can occur more easily in the shale layer than in the silty sand. Thus, more energy would be drawn from the shale layer than the silty sand resulting in lower temperatures in the shale layer. The top plot in Figure 4-9 shows that this is the case with both the 30.4 m and 15.2 m depth curves showing lower temperatures than the curves from the depths in the silty sand. Further evidence of this is the fact that the recovery curves for the lower two depths show a faster recovery than those for the higher depths, meaning that heat is flowing more quickly into those parts of the system, possibly due to the higher thermal conductivity. Another factor for the shape of these curves is the boundary conditions at either end of the pile. The ground at the top of the pile is subjected to atmospheric conditions (which are very cold as can be seen in Figure 4-3), whereas the ground below the pile is a more or less constant temperature of 13^{o}C (55.4^{o}F). Thus, the higher temperature at the lower boundary and the higher thermal conductivity in the lower layer combine to produce a sharper (or quicker) recovery curve.

Also notice the slopes of the temperature curves in the bottom plot of Figure 4-9 and how they vary with time. It should be noted that some variation with time is expected as the temperatures fluctuate in the ground naturally at the 3.0m depth. At the end of the observation period (day 15), the temperatures in the ground for the 3.0 and 9.1 m depths are still decreasing whereas the temperatures in the ground for the 15.2 and 30.4 m depths have either stopped decreasing (15.2 m) or begun to increase again (30.4 m). Operation of the system creates a negative temperature gradient around the pile, which drives heat flow towards the pile. A higher thermal conductivity would allow the temperature gradients around the pile to stabilize more quickly, as evidenced by this plot.

4.3 Ground Thermal Recharge

While the previous experimental tests focused on bridge deck heating, experimental tests were also conducted for ground recharge – to see if the temperature in the ground could be increased and, in effect, store heat in the ground for use in the winter. A series of recharge operations were performed over several warm days in June of 2013. Figure 4-10 contains the plots of the temperatures in the pile and in the ground for depths of 3.0, 9.1, 15.2, and 30.4 m. Note that in the top of Figure 4-10, each spike in the temperature curve corresponds to a recharge operation. Several observations can be made. The first is that during heat injection, the temperatures near the bottom of the pile increase more than the temperatures at the top, just as they decreased more

during bridge heating. Furthermore, the recovery curves at the end of each heating cycle are steeper for both of the lower depths, which are located in the shale. This again indicates a higher thermal conductivity for the shale layer.

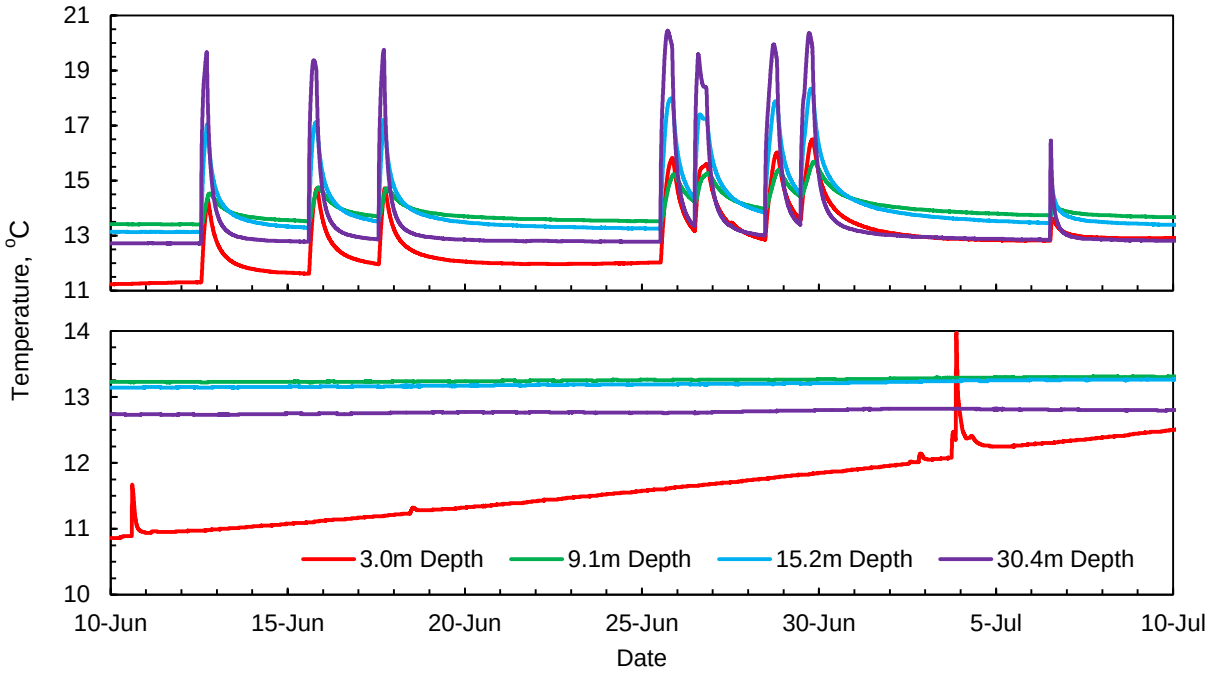

Figure 4-10 **Temperatures in the pile (top) and ground (bottom – measured in observation well 1) during ground thermal recharge.**

Observe the relative increase in the temperatures of the ground at each depth (bottom of Figure 4-10). At the end of the observation period (July 10), the temperatures in the ground for the 3.0 and 9.1 m depths are still increasing whereas the temperatures in the ground for the 15.2 and 30.4 m depths have either stopped increasing (15.2 m) or begun to decrease (30.4 m). During recharge operations, the system creates a positive temperature gradient around the pile, which drives heat flow outwards from the pile. Similar to bridge deck heating, the higher thermal conductivity of the shale layer results in quicker temperature stabilization at the lower depths.

The question still remains as to whether any heat was successfully stored in the ground for use in the winter. To answer this question, some idea of what the temperatures in the ground should be with no heating is needed. Observation well 2 is located 3.5 m (10.7 ft) from the test pile. Although the effects from heating could still affect the temperature of the ground at this distance, the effect will be less pronounced than at the energy pile and at observation well 1, which is only 1.7 m from the pile. Thus, the observation well further away can serve as a control. The net temperature difference between observation well 1 (which is representative of the ground), the energy pile, and the observation well 3.5 m from the energy pile is shown in Figure 4-11.

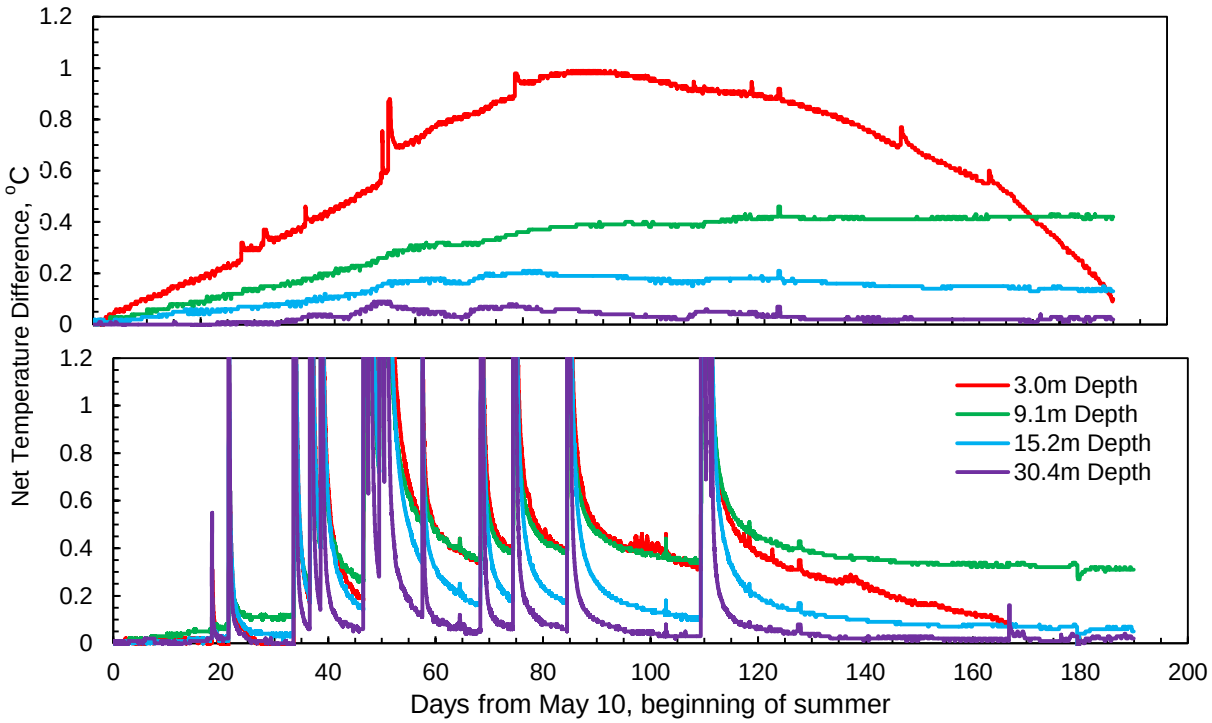

Figure 4-11 Net temperature difference in the ground over time after ground thermal recharge between OW-A (top) and the energy pile (bottom) relative to OW-B.

From Figure 4-11, it is clear that at every depth there was a positive temperature increase in the ground at OW-A relative to OW-B, and in the pile relative to OW-B. The largest increase in temperature occurs at the top two depths, which is where the soil with the lower thermal conductivity is located. The highest sustained temperature increase appears to be in the middle two depths (9.1 m and 15.2 m). This is most likely due to the fact that the 3.0 m and 30.4 m depths experience heat loss through the ground surface and to the ground below, respectively.

Table 4-2 summarizes the measured difference in temperature for the pile and ground relative to the temperature difference of the ground at a distance of 3.5 m from the pile during this period of time. For every depth except the 3.0 m depth for the ground 1.7 m from the pile, there was a positive temperature difference between it and the ground 3.5 m from the pile. The same is true for the pile. Thus, it does appear that heat was successfully stored in the ground; however, the relative temperature differences are very small. The small temperature difference may be due to the fact that there were only 8 recharge operations conducted during the summer of 2013. If summer recharge operations were conducted more consistently throughout the summer, a greater temperature increase may be able to be achieved.

Table 4-2 **Temperature difference in the ground and pile relative to the temperature difference of the ground at a distance of 3.5 m from the pile.**

Depth (m)	Temperature Difference (^{o}C)	
	1.7 m (Ground)	0 m (Pile)
3.0	0.10	0.00
9.1	0.42	0.31
15.2	0.13	0.05
30.4	0.02	0.02

5. Structural performance evaluation of a concrete bridge deck overlay

A preliminary investigation was performed to ascertain whether or not a ground-source bridge deck deicing system will impose any significant structural challenges to the bridge deck overlay. There are two primary ways in which these systems could affect the bridge deck. The first is through the physical inclusion of the circulation tubes, and the second is through the temperature gradients created from the operation of these systems. The primary focus here is the temperature gradients that were created and how they relate to current design guidelines.

5.1 Current design methodology

The structural performance of a concrete bridge deck overlay is going to be affected by thermal stresses resulting from temperature gradients. Currently, the AASHTO LRFD Bridge Design Specifications (6th Edition, 2012) outlines two methods to use in determining design thermal movements from uniform temperature ranges. Method A yields a temperature range depending on if the climate is ‘cold’ or ‘moderate’. In this case, Blacksburg, VA would classify as a ‘cold’ climate because there are 14 or more freezing days per year (defined as days with the average temperature less than 32^{o}F) and the temperature range would be 0^{o} to 80^{o}F. Procedure B uses charts to determine minimum and maximum design temperatures based on the site’s geographical location in the United States. Based on the location of Blacksburg, VA, the temperature range is 0^{o} to 110^{o}F.

The temperature gradient in the bridge deck then follows a given profile with the points specified based on the zone of the United States the site is located (Figure 5-1). Virginia is in the 3rd solar

radiation zone. Thus two scenarios can be obtained as shown below, one is positive temperature gradient which occurs during the summer when the top of the slab is warmer than the bottom; the other is negative temperature gradient which reflects temperature change mostly during winter when the bottom temperature is higher. Thus the profile looks like the following, with $T_1 = 41^oF$, $T_2 = 11^oF$, and $T_3 = 0^oF$ for positive values and $T_1 = -12.3F$, $T_2 = -3.3^oF$, and $T_3 = 0^oF$ for negative values. These temperatures should be thought of as values from the strain reference temperature, rather than absolute values. That is, T_1 is 41^oF from the strain reference temperature. Thus, if the strain reference temperature is 60^oF, T_1 would actually be 101^oF. Also note the temperature gradients that are specified. In the upper 4in of the deck, the gradient can be any greater than 10.25^oF/in for positive temperature gradients ($T_1 > T_2$) nor any greater than 2.25^oF/in for negative temperature gradients ($T_1 < T_2$).

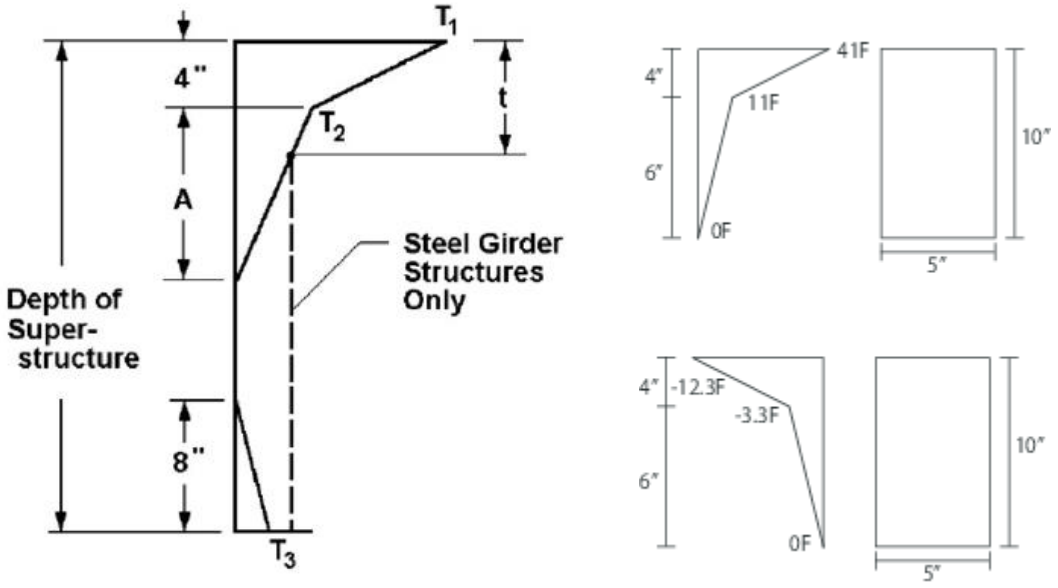

Figure 5-1 **Temperature profiles for a bridge located in Blacksburg, VA as specified by AASHTO**

Note that no consideration is given to uneven heating along the deck in the transverse or longitudinal directions.

5.2 Observed temperature gradients from experimental heating tests

A ground-source bridge deck deicing system will create changes to the naturally occurring temperature gradients in the bridge deck. To better understand the changes in temperature gradients that bridge deck deicing systems can cause, cross-sectional temperature profiles were examined from several of the experimental studies performed (as explained in Section 4). The temperature profiles from the experimental slab were compared against the temperature profiles from the control slab, and is shown in Figure 5-2. For each test, the maximum temperature gradient is plotted, with the values given in Table 5-1 alongside the design value.

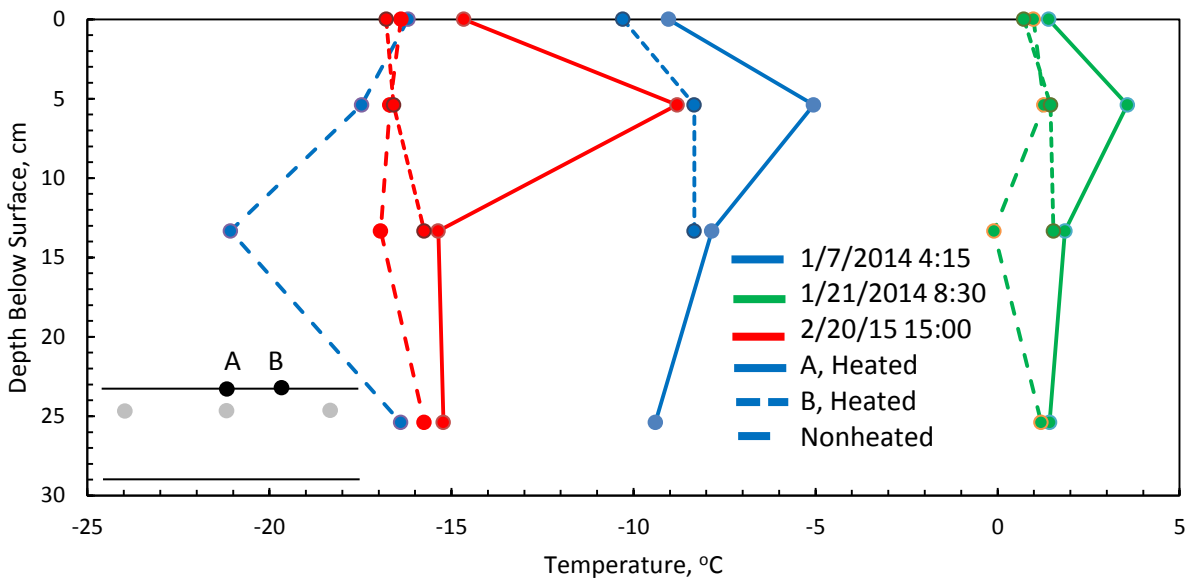

Figure 5-2 **Cross sectional temperature profiles with the most extreme temperature gradients during each experimental heating test compared with the profiles from the non-heated deck**

Table 5-1 **Maximum observed temperature gradients**

Date	Gradient (°C/cm)	
	Tube	Between
Max (Design)	0.49	
1/7/14 4:15	0.74	0.36
1/21/14 8:30	0.40	0.14
2/20/15 15:00	1.08	0.04

A few general comments will be made then each case will be examined individually. For all tests, the maximum gradient occurred between the surface and the tube, which consists of the top 5cm (2in) of the slab. This could be problematic in that extreme temperature gradients could lead to thermal stresses that induce cracking in the top 5cm. Another observation is that for two of the tests (#2 and #3), the maximum stresses occurred shortly after operation of the system began (1.5 hours for #2 and almost immediately after beginning operation for #3). This makes sense, especially when looking at the nonheated temperature profiles for these two tests. The nonheated profiles are relatively uniform. After the system begins operation, the slab starts heating at the level of the tubes, inducing a temperature gradient to the uniform profile.

During experimental test 1, the maximum gradient occurred on 1/7/2014 at 4:15. This was approximately 21.25 hours after the system was turned on and occurred during a time of extremely cold ambient temperature (see Figure 4-3). In this case, the system was not able to produce enough heat to combat the energy loss to the environment. Though the heated deck is considerably warmer than the unheated deck (as can be seen from their profiles), the temperature

decreases above and below the tube in the heated deck. Thus, during extreme weather conditions that create a demand beyond the ability of the system, operation of the system seems to result in extreme temperature gradients at the surface.

During experimental test 2, where the system performed quite well (see Section 4.2.1.2), the highest temperature gradient was less than the maximum allowed. As mentioned previously, it occurred shortly after operation of the system began and was a result of disturbing the relatively uniform temperature profile.

During experimental test 3, the highest temperature gradient was recorded shortly after operation of the system began. This was the highest temperature gradient recorded of all the experimental tests presented. It also resulted from 'disturbing' the uniform temperature profile.

From numerical studies, it is known that the temperature profile is not the same throughout the deck as thermal energy first enters the deck around the tubes, meaning the areas between the tubes do not experience as sharp of temperature changes. Figure 5-2 also compares the experimental temperature profiles at the cross-section containing the circulation tube with the profile between two tubes. It can be seen that the profile between the tubes does not exhibit the sharp gradients, indicating the high temperature gradients are localized around the tube.

5.3 Observed temperature gradients from experimental bridge deck cooling tests

These results are from the thermal recharge operations discussed previously. Two specific days were chosen to analyze because the time the system was turned on was different in both cases, however the two days had similar ambient temperatures and amounts of solar radiation. The first day is 6/26/2013 where the start time was 12:00. The second day is 8/28/2013 where the start time was 8:00. In both cases the maximum temperature gradient occurred in the top of the slab around the same time of day, as shown in Figure 5-3. And as shown in Table 5-2, the maximum gradients were well within the design value. Both halves of the deck were operated, thus no control exists to compare temperature profile measurements. But the temperature profiles between the tubes are also plotted.

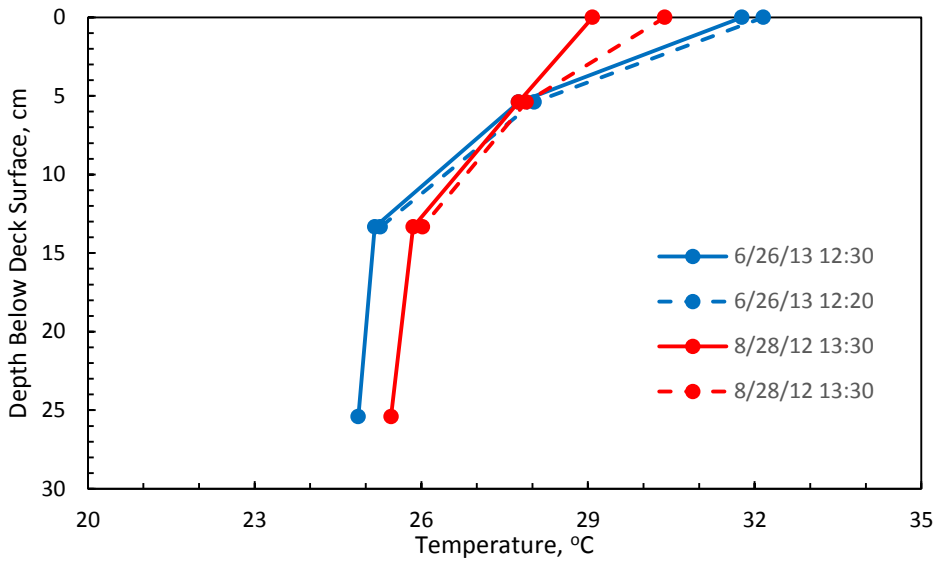

Figure 5-3 **Temperature profiles in the heated bridge deck during thermal recharge (bridge deck cooling)**

Table 5-2 **Maximum observed temperature gradients**

Date	Gradient (°C/cm)	
	Tube	Between
Max (Design)	1.64	
6/26/2013	0.74	0.76
8/28/2013	0.25	0.46

In both cases the higher gradients occurred between the tubes during early afternoon. This makes sense because that is the point where the sun starts to heat the surface of the deck but the interior of the deck is still cool, both from losing energy during the night and in the cases presented here, from active cooling by the ground. The sun is able to more quickly heat the surface of the deck between the tubes, resulting in higher temperature gradients at those locations. But the difference in the temperature gradients is minimal.

The temperature gradients were lower on 8/28/2013 than on 6/26/2013. This is most likely due to the fact that the upper portion of the deck had more energy extracted from it on 8/28 due to the earlier system operation start time, which in this case indicates that the deicing system can have a positive effect on temperature gradients.

5.4 Conclusions and future analysis considerations

The bridge deck heating experimental tests have shown that the bridge deck experiences high temperature gradients in the immediate vicinity of the deicing tubes, often shortly after operation of the system begins. This is due to imposing higher temperatures to a relatively uniform

temperature profile. The highly localized effect of these temperature gradients make it difficult to analyze the resulting stresses for several reasons:

- On a small scale, the circulation tubes are often connected directly to the top layer of reinforcement, which runs in the longitudinal and transverse directions. Because the higher temperature gradients exist in the immediate vicinity of the deicing tubes, they will also exist in the vicinity of the rebar reinforcement if the tubes are attached. Thus, the typical assumption that a bridge deck is a homogenous concrete slab that behaves according to modified properties that account for the respective volumetric percentages of concrete and rebar is not valid. In terms of thermal properties, steel and concrete are remarkably different. Furthermore, the circulation tubes are composed of a different material (often some type of polymer based plastic), with different thermal properties and add an additional level of complexity.
- On a macro scale, resulting stresses will not only depend on temperature gradients in the deck, but on the bridge deck restraint conditions.

However, despite these uncertainties a few preliminary conclusions can be drawn:

- During moderate weather conditions, the highest temperature gradients observed were well within design values. The extreme temperature gradients occurred during periods of severe weather conditions, which do not occur very frequently throughout the year.
- The severe temperature gradients often occurred due to changing the uniform temperature gradient of the slab. This could be avoided by selecting a start time such that a uniform temperature gradient does not exist in the slab. In the case of bridge deck heating, late afternoon and early evening are often good times to turn on a system following a sunny day as the top several centimeters of the deck will be warmer, meaning a less extreme temperature gradient will be created in the immediate vicinity of the circulation tubes when warm fluid is circulated.
- Despite the extreme temperature gradients that occurred, they were relatively transient in nature and did not exist for a very long period of time as the heat propagated from the tubes throughout the deck.

In examining bridge deck cooling, which occurs during thermal recharge operations during the summer, temperature gradients larger than the design values were not observed. In fact, it appears from preliminary results that the circulation system can serve to reduce the temperature gradients in the upper portion of the bridge deck. These effects are also less localized around the tubes than those of bridge deck heating, and appear to be rather uniform in the longitudinal and transverse bridge deck directions.

6. Finite difference analysis of heat exchange through geothermal piles

Two different numerical modeling approaches have been adopted in this research to model pile-soil heat exchange. The first modeling approach utilizes finite difference solution technique. A finite difference code developed by Ghasemi-Fare and Basu (2013a, 2013b, 2015) is used for solving a system of partial differential equations which describe heat flow through heat carrier fluid and heat conduction in soil and concrete. In the later part of this research, the first generation FD model was extended to a more rigorous second generation model that can essentially capture the effects of different design, operational and site-specific variables on time-dependent variation of ground and circulation fluid temperature.

6.1 Annular cylinder model

Heat transfer through a concrete geothermal pile with an embedded U-shaped circulation tube is first modeled using an annular cylinder approximation. Half of the pile is modeled exploiting the approximately axisymmetric heat flow condition in the medium surrounding the pile (Figure 6-1a). Note that the location and arrangement of the circulation tubes within a geothermal pile does not strictly satisfy the condition of an axisymmetric geometry. However, the diameter of the circulation tube (heat source) is two orders of magnitude smaller than the expected thermal influence zone surrounding the pile. Therefore, the assumption of axisymmetric heat conduction in the media (i.e., concrete and soil) surrounding the heat source is not far from reality.

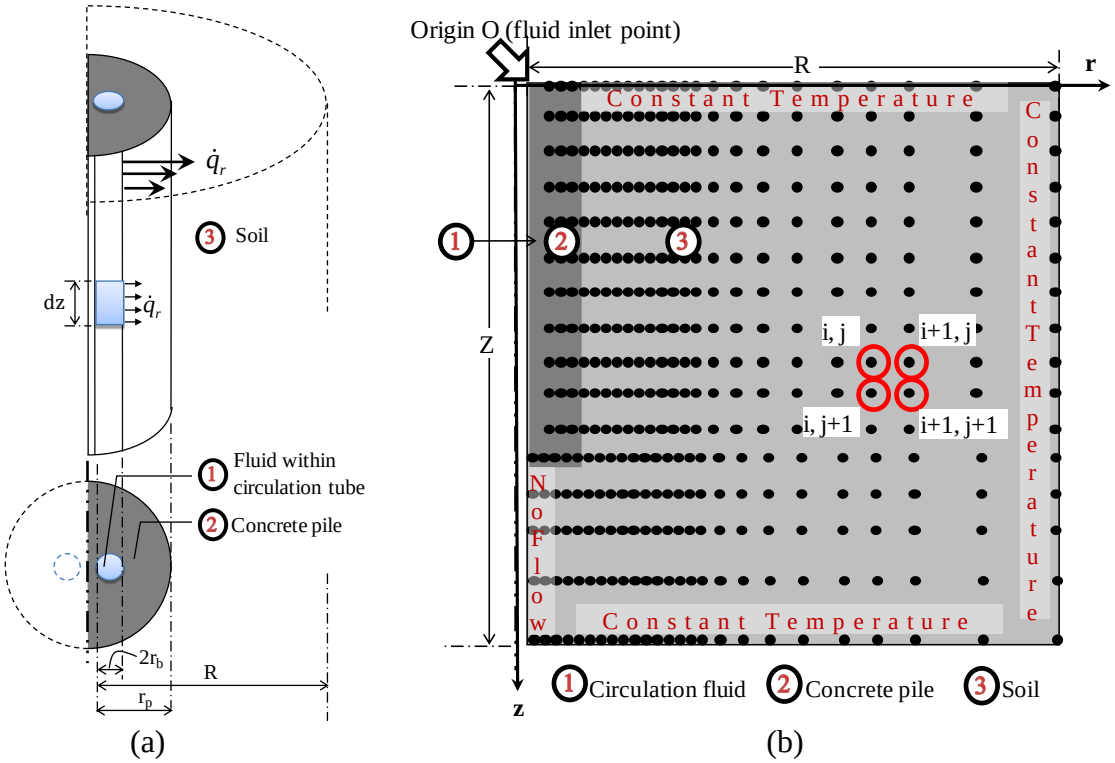

Figure 6-1 **Annular cylinder heat source model (a) isometric and plan view and (b) finite difference grid and boundary conditions**

Thus time-dependent evolution of temperature T (r, z, t) due to heat conduction within the analysis domain can be expressed as:

$$\frac{1}{\alpha}\frac{\partial T}{\partial t} = \frac{\partial^2 T}{\partial z^2} + \frac{\partial^2 T}{\partial r^2} + \frac{1}{r'_{\mathrm{m}}}\frac{\partial T}{\partial r} \tag{6-1a}$$

$$\alpha = \frac{k}{\rho C_p} \tag{6-1b}$$

where α, k, ρ and C_p are, respectively, thermal diffusivity, thermal conductivity, mass density and specific heat capacity of the heat conduction medium and t is time.

Equation (6-1) alone cannot describe heat transfer through a geothermal pile because it does not capture heat flow within the circulation tube. Considering that average temperature of an element A (Figure 6-1a) within the circulation tube increases by an amount dT over time dt and assuming an average heat flow rate q (from element A to concrete pile) over the length dz, the heat balance equation for element A can be written as:

$$\frac{\partial T}{\partial t} = v\frac{\partial T}{\partial z} + \frac{2k_{\mathrm{c}}}{\rho_{\mathrm{f}} C_{\mathrm{p_f}} r_{\mathrm{t}}}\frac{\partial T}{\partial r} \tag{6-2}$$

where dT is the temperature difference (over the length dz) between top and bottom of element A, v and C_{pf} are, respectively, velocity and specific heat capacity of heat carrier fluid circulating through the tube, and r_{t} is radius of the circulation tube.

6.1.1 Validation of the developed finite difference code

The FD code is developed for solving PDEs associated with the proposed annular cylinder heat source model; however, with certain adjustments in boundary and initial conditions, this code can also produce solutions for idealized heat source models available in literature. The FD code was verified by comparing available analytical solutions for finite line and infinite hollow cylinder heat sources (Zeng *et al*. 2002, and Carslaw and Jaeger 1947) with the respective solutions obtained using the developed code. Note that both finite line and infinite hollow cylinder heat source models use constant heat flux (an input parameter for these models) along the entire length of the heat source. Additionally, both of these models consider a single value of thermal conductivity k for the homogeneous medium around the heat source. Hence, the

following modifications are required in order for the developed FD code to capture the constant-heat-flux condition at $r = 2r_t$:

$$\left.\frac{\partial T}{\partial r}\right|_{r=2r_t} = -\frac{q_l}{2\pi r_t k} \tag{6-3}$$

$$\left.\frac{\partial^2 T}{\partial r^2}\right|_{r=2r_t} = \frac{\left(\frac{\partial T}{\partial r}\right)_{i+1} - \left.\frac{\partial T}{\partial r}\right|_{r=2r_t}}{\Delta r_{i+1}} = \frac{\frac{T_{i+1,j} - T_{i,j}}{\Delta r_{i+1}} + \frac{q_l}{2\pi r_t k}}{\Delta r_{i+1}} \tag{6-4}$$

where q_l is the constant heat flux per unit length of the heat exchanger. **Error! Reference ource not found.** shows that the developed FD code can successfully predict analytical heat transfer solutions for finite line source (q_l = 100 Wm^{-1}, r_b = 0.025 m, L_b = 5 m and R_b = r_b/ L_b = 0.005; r_b and L_b are, respectively, radius and length of the idealized heat source) and infinite hollow cylinder source (q_l = 100 Wm^{-1}, r_b = 0.3 m and L_b /r_b = 100).

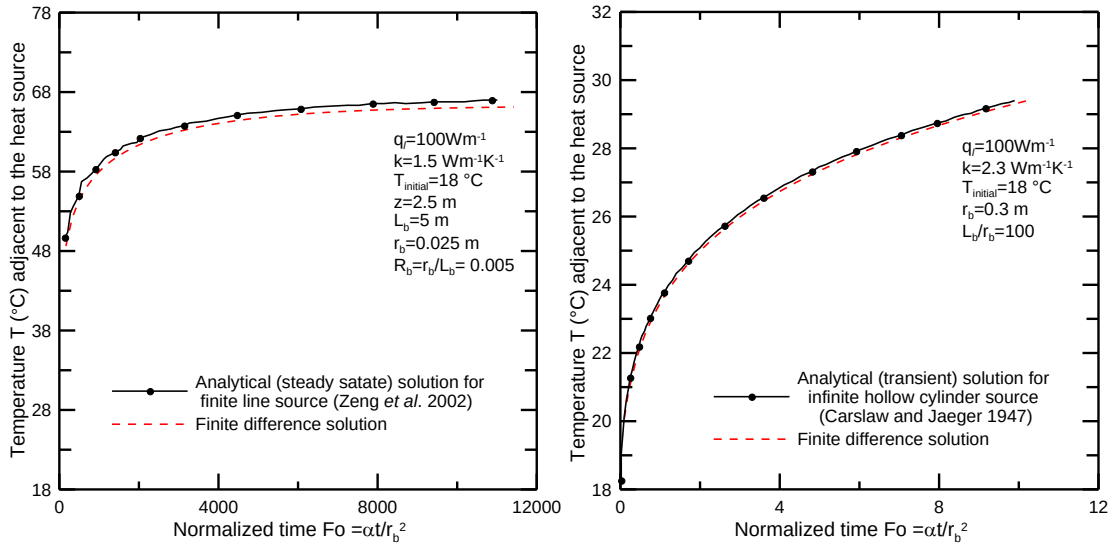

(a) (b)

Figure 6-2 **Comparison between analytical solutions and results obtained using the developed Finite Difference code (with appropriate modifications) for (a) finite line heat source (steady-state solution) and (b) infinite hollow cylinder heat source (transient solution)**

6.1.2 Analysis results

Analyses are performed using the developed FD code to quantify heat transfer through a 30-m-long, 0.6-m-diameter (r_p=0.3 m) geothermal pile under different thermal loading conditions. A

soil domain with radius R = 10 m and height Z = 35 m is considered around the pile. Thermal properties for concrete and soil, as used in the analyses, are given in Table 6-1; specific heat of the heat carrier fluid C_{pf} is assumed to be equal to 4190 $Jkg^{-1}C^{-1}$. Few additional analyses are performed to identify the effects of some important input variables on thermal efficiency of heat exchanger piles and on time-dependent evolution of ground temperature T_g.

Table 6-1 **Thermal properties of concrete and soil used in the analyses**

Thermal Properties	Concrete	Soil
Diffusivity α (m^2s^{-1})	$\alpha_c = 0.66\times10^{-6}$	$\alpha_s = 1.02\times10^{-6}$
Conductivity k ($Wm^{-1}K^{-1}$)	$k_c = 1.5$	$k_s = 2.3$

Figure 6-3 shows that the thermal influence zone around the heat exchanger pile extends approximately up to a radius of $160r_t$ (= 3.2 m ≈ $11r_p$) after 60 days of heat rejection from the pile to the ground (a thermal loading condition that simulates operation of a geothermal pile during summer). Note that the thermal influence zone continuously grows with time after heat rejection starts. Nevertheless, two months of continuous heat rejection from a geothermal pile to the ground (as simulated in this analysis) can be considered as an extreme scenario for thermal operation of such a pile during summer in most part of the world and thus $160r_t$ (≈ $11r_p$) would practically be an upper bound of thermal influence zone around a heat exchanger pile. Except in the vicinity of pile head and base, radial heat transfer is observed for the entire length of the pile. Such radial heat transfer is also observed in previous numerical studies of heat exchanger piles (Laloui *et al*. 2006, Abdelaziz *et al*. 2001). Even after 60 days of heat exchange operation, change in ground temperature is negligible (less than 1°C) beyond a depth of $6r_p$ below the pile base (Figure 6-3).

Thermal conductivity of soil k_s (and consequently, thermal diffusivity α_s) depends on various factors such as dry density, water content, and soil texture. For coarse- and fine-grained soils, the range of k_s varies, respectively, from 0.9 to 4.2 $Wm^{-1}K^{-1}$ and from 0.3 to 2.1 $Wm^{-1}K^{-1}$ (Brandl 2006). The value of k_s reduces with decrease in soil water content; k_s is minimum for dry soil (usually 0.2-0.4 W/mC; Tarnawski *et al.* 2011). Soil near the ground surface is often not fully saturated and a low value of k_s (and thus α_s) is expected within this desiccated zone. Heat transfer performance of a geothermal pile is investigated in the presence of a 5 m desiccated zone of soil (with k_s =0.38 $Wm^{-1}K^{-1}$ and $\alpha_s = 1.7\times10^{-7}$ m^2s^{-1}) just below the ground surface. Figure 6-4 shows that the thermal influence zone is smaller within the top desiccated soil layer; however, increase in ground temperature T_g adjacent to the pile is greater in the desiccated soil layer with lower value of α_s than that in the soil layer with higher value of α_s.

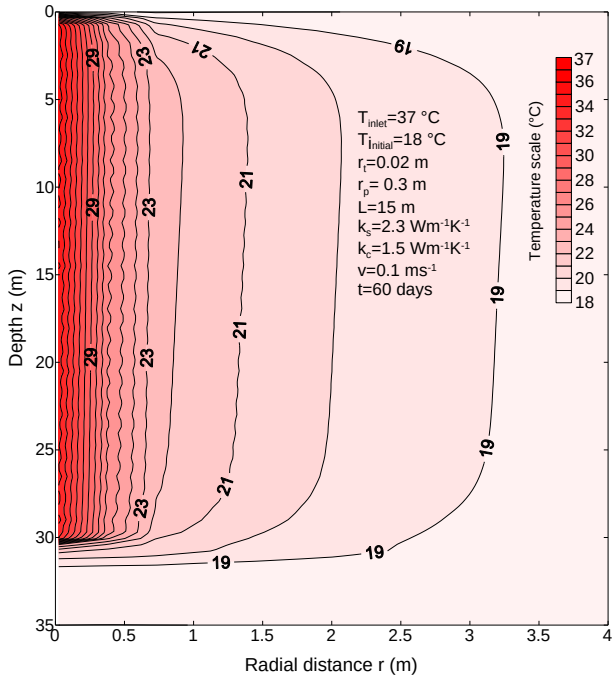

Figure 6-3 **Temperature (°C) profile in homogeneous ground surrounding a geothermal pile after 60 days of heat rejection**

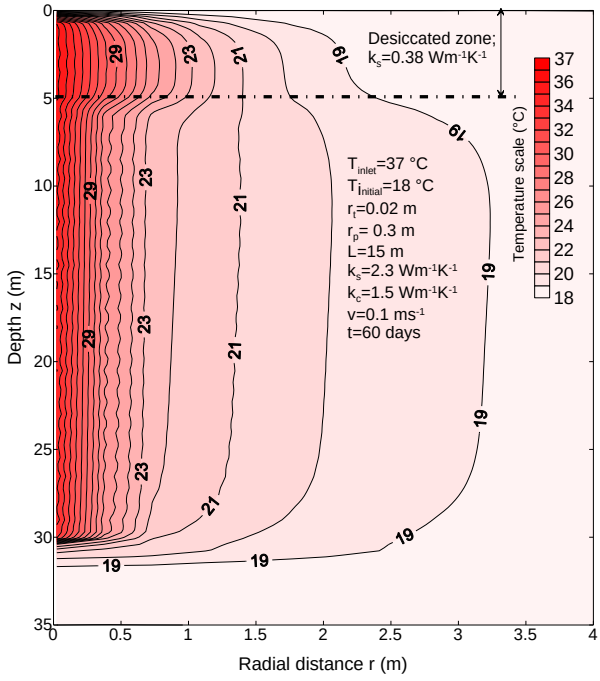

(b)

Figure 6-4 **Temperature (°C) profile (after 60 days of heat rejection) around a geothermal pile installed in ground with a top 5 m desiccated zone**

6.1.3 Effect of operational parameters

Velocity of fluid circulation through the embedded circulation tube and fluid temperature at the inlet point are expected to play key roles on ground temperature response and energy exchange efficiency of the pile-soil system. Hence, the effects of inlet fluid temperature T_{inlet} (which implies thermal gradient based on the difference $\Delta\theta$ between inlet and initial ground temperature) and fluid circulation velocity v on ground temperature response are investigated.

The effects of initial temperature difference $\Delta\theta$ (= $T_{inlet} - T_{initial}$) and fluid circulation velocity v on ground temperature T_g is shown in Figure 6-5. It is observed that at any given time t after the start of the heat transfer operation, the thermal influence zone is independent of $\Delta\theta$ and v. Ground temperature T_g within the thermal influence zone increases with increase in both $\Delta\theta$ and v. Figure 6-6 shows (for v = 0.02 and 0.1 ms^{-1}) the variation of temperature T along depth z at different radial distances; temperature gradient along depth (dT/dz) increases as v decreases.

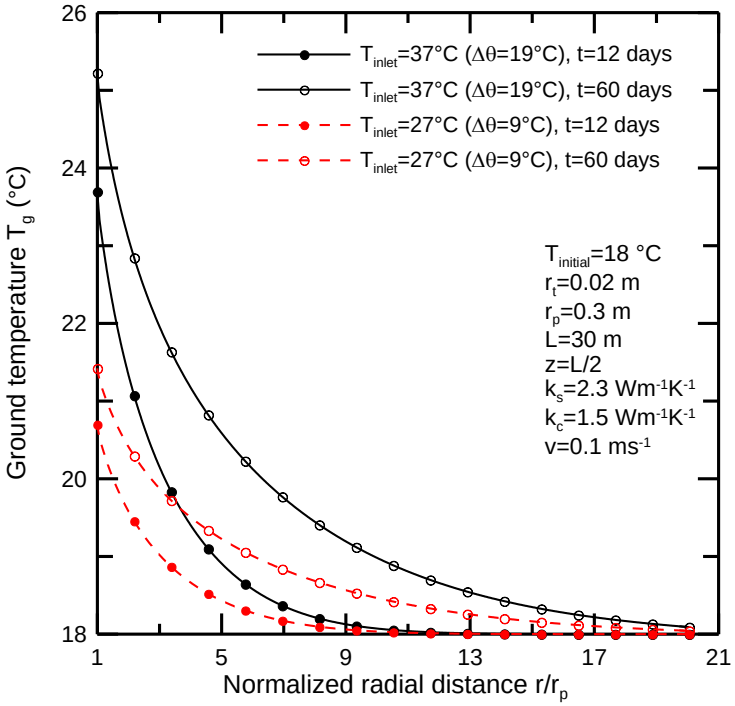

Figure 6-5 (a)

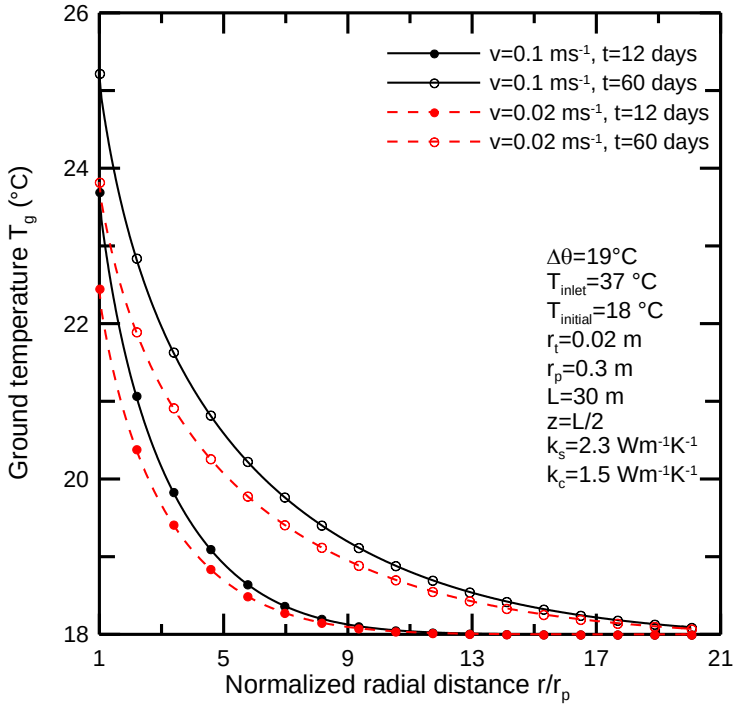

Figure 6-5 (b)

Figure 6-5 **Variation of ground temperature T_g for different values of (a) initial temperature difference $\Delta\theta$ (= $T_{inlet}-T_{initial}$) and (b) fluid circulation velocity v**

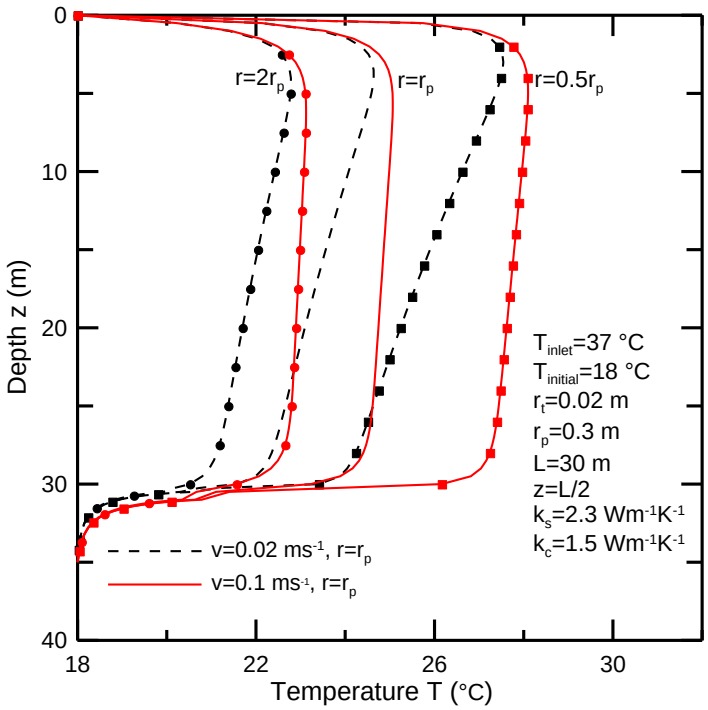

Figure 6-6 **Effect of fluid circulation velocity v on temperature T along depth z**

6.1.4 Variation of heat flux and fluid temperature

The time-dependent evolution of heat flux (per unit length) q_l along the length of the circulation tube is shown in Figure 6-7. Heat flux q_l decreases linearly along the length of the circulation tube. Over a heat rejection period of 60 days, q_l at the middle of the pile (i.e., at z = 15 m) reduces by almost 30% from its value at the end of the first day of operation. Therefore, the use of idealized heat transfer models with constant values of q_l along the entire length of the heat source would introduce significant errors in the quantification of heat transfer through a geothermal pile.

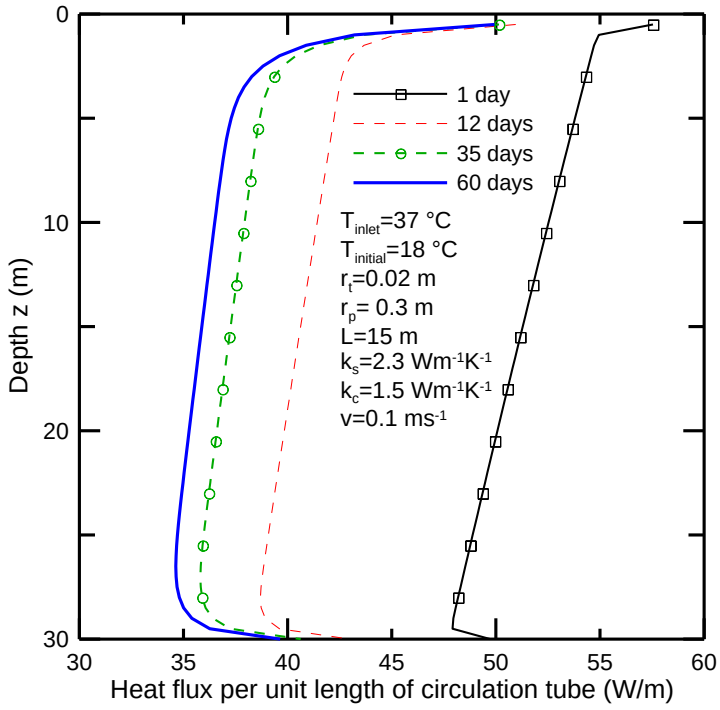

Figure 6-7 **Variation of heat flux q_l (per unit length) with depth z at different instants of heat rejection operation**

Transient variation of fluid temperature T_f along the length of the circulation tube is shown in Figure 6-8. Only few minutes after the heat transfer starts, T_f varies linearly with depth z. From in-situ performance tests on geothermal piles, Gao *et al.* (2008a and 2008b) observed similar linear distribution of fluid temperature along the length of circulation tubes. The distribution of T_f along the length of the circulation tube stabilizes (i.e., reaches steady state) after 12 days of heat exchange operation.

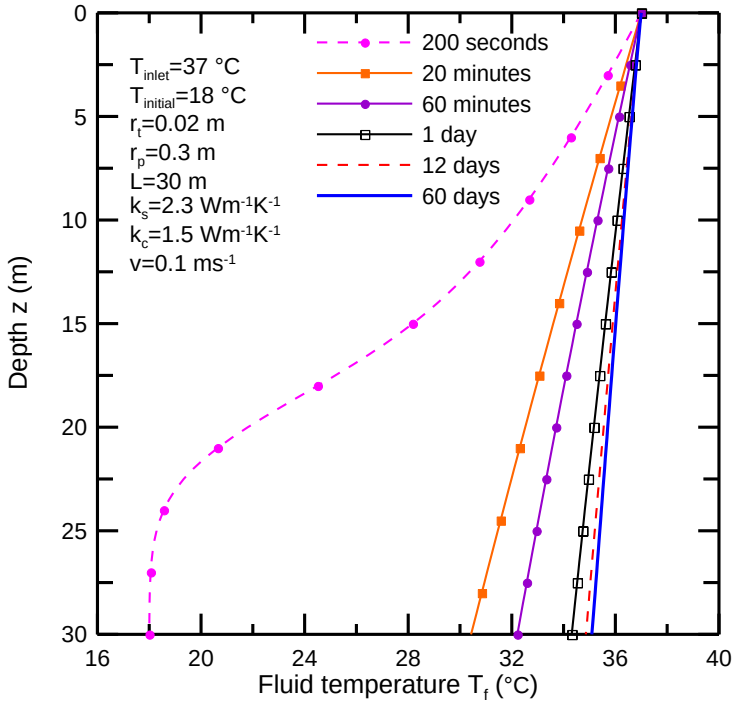

Figure 6-8 Variation of fluid temperature T_f (C) along the length of the circulation tube

In order to investigate the effect of variable heat flux on evolution of temperature within the heat exchanger pile and that in soil surrounding the pile, result obtained using the proposed annular cylinder heat source model is compared with finite line source solution (Figure 6-9). For such a comparison, a constant value of heat flux q_l needs to be assigned for the finite line source. However, the choice of q_l for use in the finite line source model introduces significant uncertainty in the prediction because q_l varies along the length of a real geothermal pile and such variation of q_l changes with time during heat exchange operation (Figure 6-7). The values of q_l used for finite line source solutions plotted in Figure 6-9 are the maximum and minimum heat flux values (i.e., $q_{l,\,max}$ and $q_{l,\,min}$, respectively at points near the top and bottom of the circulation tube) obtained from simulations of one hour, one day, and one week of heat exchange operation using the proposed annular cylinder model. It is observed that finite line source solutions (i.e., the use of a constant value of q_l along the entire length of the heat source) can significantly misinterpret the increase in temperature within both pile and soil. The maximum difference between predictions using the proposed annular cylinder model and the idealized finite line source model can be as high as 17°C at a point adjacent to the heat source and 12°C at the pile-soil interface. While the use of finite line source model with high values of constant q_l would result in significant overprediction for pile and soil temperature, the use of low values of q_l in finite line source model may consistently underpredict such temperature (Figure 6-9).

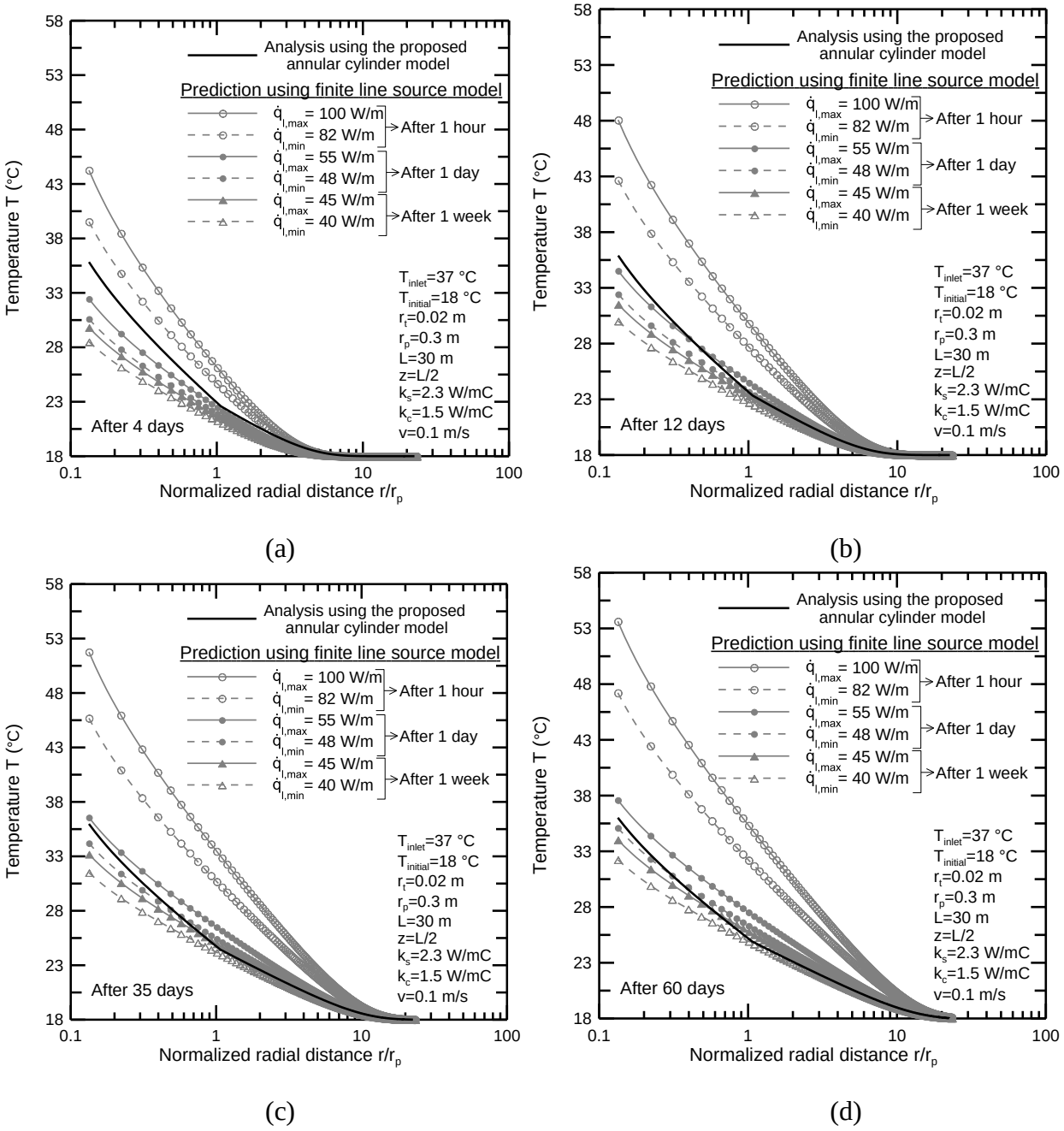

Figure 6-9 **Effect of variable heat flux on temperature within pile and soil at different times after the start of heat exchange operation for (a) *t* = 4 days, (b) *t* = 12 days, (c) *t* = 35 days and (d) *t* = 60 days**

6.2 U-tube model

A finite difference (FD) model has been developed at PSU to investigate the heat transfer from the heat carrier fluid to the surrounding media considering a vertical plane that passes through the pile and contains both branches of the U-shaped circulation tube embedded within the heat exchanger pile (Ghasemi-Fare and Basu 2013a, 2013b, 2015; Ghasemi-Fare 2015). The model is capable to predict the outlet fluid temperature as well as soil and concrete temperature. The

model simultaneously solves partial differential equations for (i) heat conduction within the concrete pile and soil (ii) heat balance within the circulation tube and. Except than the aforementioned partial differential equations, heat flow continuity equations should also be considered to predict time dependent temperature evolution of the fluid, concrete, and soil. Two individual heat sources are considered in the developed model. Schematic view of the domain is presented in Figure 6-10. Temperature increments in any arbitrary point in the media due to both downward and upward branches of U-tube can be calculated using:

$$\rho\pi\Delta z\left[\left\{\left(r_{i+1}^{L}\right)^2-\left(r_i^{L}\right)^2\right\}+\left\{\left(r_{i+1}^{R}\right)^2-\left(r_i^{R}\right)^2\right\}\right]C_p\Delta T^{ij}=\left(Q_{i,j}^{in}-Q_{i,j}^{out}\right)^{L}+\left(Q_{i,j}^{in}-Q_{i,j}^{out}\right)^{R} \tag{6-5}$$

where r^{R} [= $\{r-0.5\mathrm{s_t}-(r_\mathrm{t}+t_\mathrm{t})\}$] and r^{L} [= $\{r+0.5\mathrm{s_t}+(r_\mathrm{t}+t_\mathrm{t})\}$] are radial distances measured, respectively, from the center of the downward (left) and upward (right) branches of the circulation tube, Δz is the distance between the top and bottom surfaces of the FD stencil, ρ and C_p are, respectively, mass density and specific heat capacity of the medium in which the FD stencil is located. $\left(Q_{i,j}^{in}-Q_{i,j}^{out}\right)^{L}$ and $\left(Q_{i,j}^{in}-Q_{i,j}^{out}\right)^{R}$ are net heat flow into the stencil, respectively, due to the left (designated by the letter *L*) and right (designated by the letter *R*) branches of the circulation tube..

Considering the radial convection resistance of the fluid circulating inside the circulation tube, heat balance equation for any element within a branch of the U-tube can be expressed as:

$$\frac{\partial T}{\partial t}=v\frac{\partial T}{\partial z}+\frac{2k_\mathrm{t}}{\rho_\mathrm{f}C_\mathrm{pf}r_\mathrm{p}}\frac{\partial T}{\partial r}\Big|_{r=r_\mathrm{w}} \tag{6-6}$$

where v is average velocity of fluid circulation and r_t is inner radius of the circulation tube), ρ_f is mass density of circulation fluid, C_pf is specific heat of circulation fluid, T_avg is the average fluid temperature at any cross section and can be calculated as $T_\mathrm{avg}=\dfrac{2}{v_m r_\mathrm{t}^2}\displaystyle\int_0^{r_\mathrm{t}} rvTdr$; v_m is the mean fluid velocity at the cross section under consideration. The variation of flow velocity at any depth within the circulation tube is not considered in this study, therefore, $v = v_\mathrm{m}$.

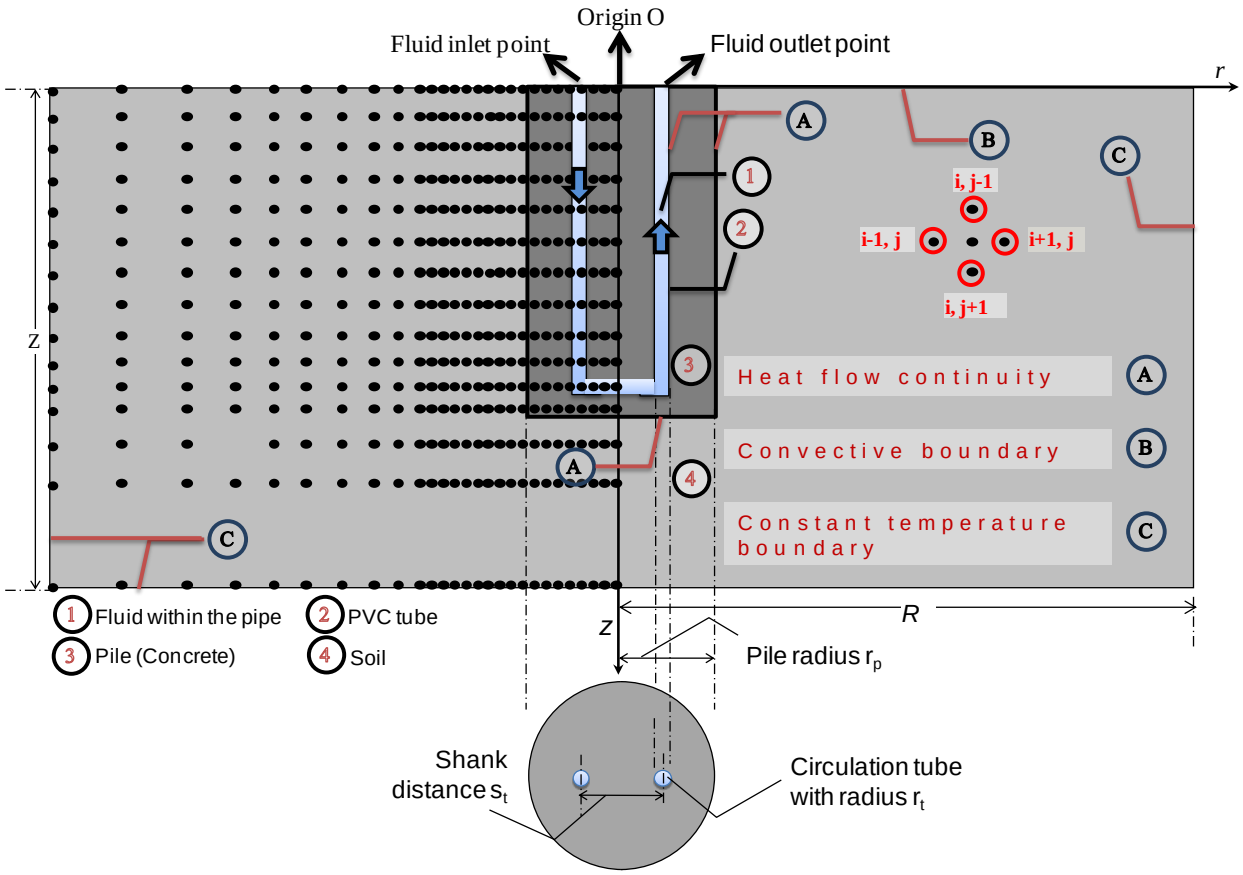

Figure 6-10 **Schematic domain of the numerical model developed at PSU**

Coupling of equations (6-5) and (6-6) at the fluid–tube (PVC) interface [i.e. at $r = \pm(0.5s_t+t_t)$, $\pm(0.5s_t+2r_t+t_t)$; t_t is the thickness of the PVC tube] is achieved through heat flux continuity condition imposed at the fluid-PVC interface.

$$h_f\left(T_{fm}-T_{fw}\right)=-k_t\left(\frac{\partial T}{\partial r}\right)\Bigg|_{\text{fluid-PVC interface}} \tag{6-7}$$

where k_t is the thermal conductivity of the PVC tube.
Coupled solution of equations (6-5) and (6-6) can capture heat transport along the length of the circulation tube branches and the heat conduction within the soil and the pile.

6.2.1 Finite difference formulation

Using an explicit solution scheme for two consecutive time steps, finite difference form of the governing partial differential equation (6-5) can be written as:

$$\frac{1}{\alpha}\left(\frac{\partial T}{\partial t}\right)=\left[\frac{\left(-2r_{i,j}^{\mathrm{L}}\left.\frac{\partial T}{\partial r}\right|_{r=r_{i,j}^{\mathrm{L}}}+2r_{i+1,j}^{\mathrm{L}}\left.\frac{\partial T}{\partial r}\right|_{r=r_{i+1,j}^{\mathrm{L}}}\right)+\left(-2r_{i,j}^{\mathrm{R}}\left.\frac{\partial T}{\partial r}\right|_{r=r_{i,j}^{\mathrm{R}}}+2r_{i+1,j}^{\mathrm{R}}\left.\frac{\partial T}{\partial r}\right|_{r=r_{i+1,j}^{\mathrm{R}}}\right)}{\left[\left(r_{i+1}^{L}\right)^2-\left(r_i^{L}\right)^2\right]+\left[\left(r_{i+1}^{R}\right)^2-\left(r_i^{R}\right)^2\right]^2}\right]+\left.\left(\frac{\partial^2 T}{\partial z^2}\right)\right|_{(i,j)} \tag{6-8}$$

Combination of Equations (6-6)-(6-7) provides fluid temperature variation within a cross section of the circulation tube at any depth. The finite difference form of the resulting equation is:

$$T_{i,j}^{t+1}-T_{i,j}^{t}=v\frac{\Delta t}{\Delta z_j}\left(T_{i,j-1}^{t}-T_{i,j}^{t}\right)+\frac{2k_g\Delta t}{\rho_{\mathrm{f}}C_{\mathrm{pf}}r_p\Delta r_i}\left(T_{i+1,j}^{t}-T_{i,j}^{t}\right) \tag{6-9}$$

As values of thermal conductivity (and consequently, thermal diffusivity) of soil, concrete and pipes are different, heat flow continuity conditions are required at the pipe-concrete interface (i.e. at $r = \pm (0.5s \pm r_{\mathrm{p}})$; r_{p} is the radius of the pipe and s is the shank spacing) and at the pile-soil interface (i.e. at $r=\pm r_b$; r_{b} is the radius of the borehole heat exchanger).

The finite difference form of the heat flow continuity condition at the grout-soil interface is presented below. Similar continuity condition is used at the pipe-concrete interface as well.

$$\left(\frac{T^{t+1}-T^{t}}{\Delta t}\right)\left[\frac{\left(r_i^2-r_{i-1}^2\right)\left(\frac{k_{\mathrm{c}}}{\alpha_{\mathrm{c}}}\right)+\left(r_{i+1}^2-r_i^2\right)\left(\frac{k_{\mathrm{s}}}{\alpha_{\mathrm{s}}}\right)}{\left(r_{i+1}^2-r_{i-1}^2\right)}\right]=$$
$$\frac{1}{r_i}\left[\frac{k_{\mathrm{s}}r_{i+1}\left(\frac{T_{i+2}^{t}-T_{i+1}^{t}}{r_{i+2}-r_{i+1}}\right)-k_{\mathrm{g}}r_{i-1}\left(\frac{T_i^{t}-T_{i-1}^{t}}{r_{i+2}-r_{i+1}}\right)}{\left(r_{i+1}-r_{i-1}\right)}\right]+k_{\mathrm{s}}\left(\frac{r_{i+1}^2-r_i^2}{r_{i+1}^2-r_{i-1}^2}\right)\frac{\partial^2 T}{\partial z^2}+k_{\mathrm{g}}\left(\frac{r_i^2-r_{i-1}^2}{r_{i+1}^2-r_{i-1}^2}\right)\left(\frac{\partial^2 T}{\partial z^2}\right) \tag{6-10}$$

Convective boundary condition is used for the top boundary of the analysis domain, and constant temperature boundary condition is used for the left, right and bottom boundaries (Figure 6-10). Convective boundary condition for the ground surface and constant temperature boundary for the bottom side are defined in equations (6-11a) and (6-11b) respectively.

$$T_{i,j}^{t+1} - T_{i,j}^{t} = \alpha_{i,j}\Delta t\left[\frac{\partial^2 T}{\partial r^2} + \frac{1}{r_i}\frac{(T_{i+1,j}^{t} - T_{i,j}^{t})}{\Delta r} - \frac{1}{\Delta z}\left(\frac{(T_{i,j+1}^{t} - T_{i,j}^{t})}{\Delta z} + h_{\text{tg}}(T_{i,j}^{t} - T_{\text{ag}})\right)\right] \quad \text{for} \quad -R < r < R,\ z = 0 \tag{6-11a}$$

$$T = T_{\text{initial}} \qquad \text{for} \quad -R \le r \le R,\ z = Z \tag{6-11b}$$

where h_{tg} is a convective heat transfer coefficient through the top boundary of the analysis domain and T_{ag} is the temperature of the medium above ground surface.

6.2.2 Stability condition

Time step size Δt that can be used in the FD formulation depends on the grid density. To avoid solution instability, maximum time step used in the analyses was restricted to that derived using Courant-Friedrichs-Lewy stability criterion (Courant et al. 1967). For the given problem, Δt is decided based on the following expression:

$$\Delta t \le \min\left\{\frac{1}{\frac{2\alpha}{\Delta r^2} + \frac{2\alpha}{\Delta z^2} + \frac{\alpha}{r_t \Delta r}},\ \frac{1}{\frac{v}{\Delta z} + \frac{2k_{\text{p}}}{\rho_{\text{f}} C_{\text{p}_{\text{f}}} r_p \Delta r}}\right\} \tag{6-12}$$

6.2.3 Verification

The accuracy of the finite difference model developed at PSU was studied by comparing the numerical model predictions with the results obtained from the available analytical solution for a finite line source (FLS) model (Zeng *et al*. 2002). The accuracy of the model for both short term (a couple of hours) and long term (2 months of operation) was investigated using the analytical solution. In order to compare the FD model a single value of thermal conductivity and diffusivity is used for all the materials (soil, pile, and PVC tube).

In order to verify the model, the heat source was assumed to be the FLS model with length equal to that of the pile placed along the center of the pile. An equivalent amount of constant power per unit length q_{l} (= Q/L; where Q is constant power injected at the inlet point and L is pile length) is used in the FLS model. The fluid inlet temperature of the model depends on the output temperature and the applied temperature differences calculated from the heat injection power.

$$T_{\text{in}}(t) = T_{\text{out}}(t) + \frac{q}{\left(\rho_{\text{f}} v \pi r_t^2 c_{pf}\right)} \tag{6-13}$$

Results from a trial analysis (for q = 2500 W and L = 25 m) using the developed FD model show that, even for constant rate of power injection, heat rate varies from 55 Wm^{-1} at the inlet point to 45 Wm^{-1} at the outlet point of the circulation tube (Figure 6-11 a). Nevertheless, both short- and long-term ground temperature response obtained from analysis using the FD model agrees well with that predicted by the FLS model (Figure 6-11 b and Figure 6-11 c).

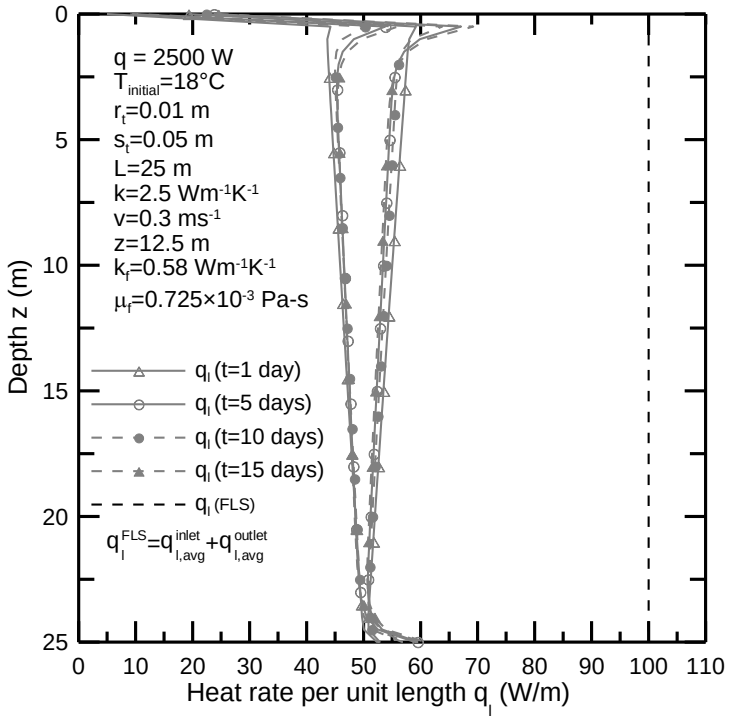

Figure 6-11 (a)

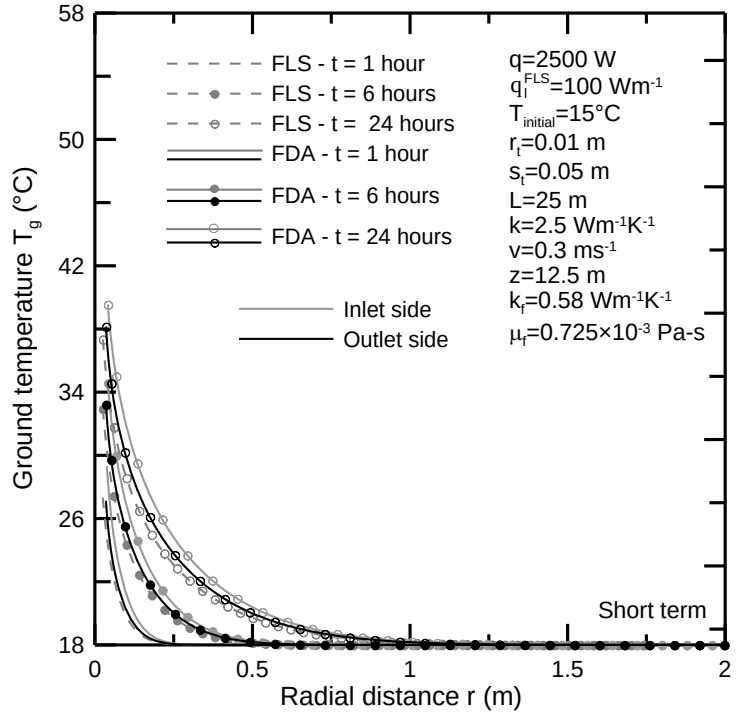

Figure 6-11 (b)

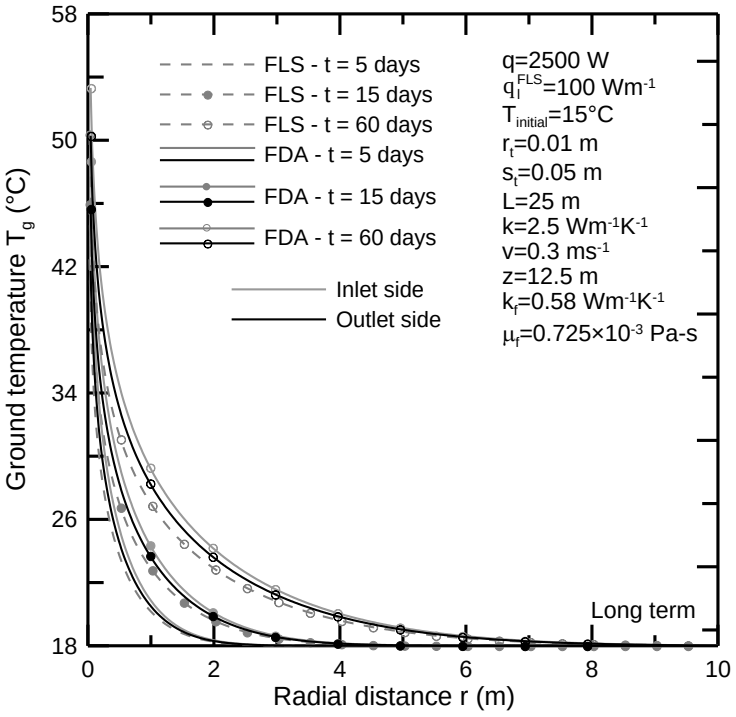

Figure 6-11 (c)

Figure 6-11 **Comparison of the results obtained using FD and FLS models: (a) variation of q_l with depth, (b) radial variation of soil temperature at short-term (c) radial variation of soil temperature at long-term**

6.2.4 Comparison with published field test data

The developed FD model is also verified by comparing model predictions with recorded field test data reported by Geo *et al*. (2008a and 2008b), Jalaluddin *et al*. (2011), Javed and Fahlen (2011), and Abdelaziz (2013). The short-term thermal test reported by Gao *et al*. (2008a, and 2008b) on a 25-m-long geothermal pile with an embedded circulation tube (with radius r_t=1cm) is simulated using the FD model. Boundary conditions and values of different input parameters (k_s = 1.3 $Wm^{-1}K^{-1}$, α_s = 5.86×10^{-7} m^2s^{-1}, k_c = 1.63 $Wm^{-1}K^{-1}$ and α_c = 7.78×10^{-7} m^2s^{-1}, μ_f = 0.725×10^{-3} Pa-s, $T_{initial}$ = 18.2 °C, T_{inlet} = 35.13 °C and t = 3 hours) are adopted from Gao *et al*. (2008a, and 2008b). Figure 6-12 shows that the outlet temperature T_{outlet} predicted using the developed FD model compares very well with the recorded field data. Difference between recorded field data and predicted value of T_{outlet} is only 0.06 °C. Figure 6-12 also shows that the annular cylinder model described in Chapter 3 underpredicts fluid temperature along the length of the circulation tube because the interaction between two branches of the tube is not considered in the annular cylinder model. In absence of any recorded temperature data along the length of the circulation tube, only the predicted distribution of fluid temperature along the circulation tube is shown in Figure 6-12. The predicted linear variation of fluid temperature along the length of the circulation tube is consistent with fluid temperature variation reported by Gao *et al*. (2008a, and 2008b).

Jalaluddin *et al*. (2011) conducted field thermal performance tests on a 20-m-long steel geothermal pile filled with silica sand. Different configurations of circulation tubes (single U-tube, double-tube and multi-tube) were used in the field study. Results obtained for the single U-shaped circulation tube (with inner radius r_t = 1.3 cm) is used to gage the prediction capability of the FD model. Field tests with two different values of fluid circulation (flow) rate q_f = 6.67×10^{-5} and 1.33×10^{-4} m^3s^{-1} (corresponding to fluid circulation velocity v = 0.126 and 0.251 ms^{-1}, respectively) are simulated using the FD model. All input parameters (r_t = 0.013 m, k_s = 1.2 $Wm^{-1}K^{-1}$, k_f = 0.58 $Wm^{-1}K^{-1}$, μ_f = 0.798×10^{-3} Pa-s, $T_{initial}$ = 18 °C, T_{inlet} = 26.5 °C for q_f = 3.33×10^{-5} m^3s^{-1}, and T_{inlet} = 26.3 °C for q_f = 1.33×10^{-4} m^3s^{-1}) are adopted based on the information provided in Jalaluddin *et al*. (2011). The thermal conductivity of the grout (silica sand), as reported by Jalaluddin *et al*. (2011), is used as the value of k_c (= 1.4 $Wm^{-1}K^{-1}$). Figure 6-13 shows that values of outlet fluid temperature T_{outlet} obtained from FDAs at both transient and steady state are in good agreement with field data reported by Jalaluddin *et al*. (2011). The maximum difference observed between recorded and predicted values of T_{outlet} is within 0.5% (0.08 °C, and 0.12 °C temperature differences, respectively, for 8 and 4 lit/minutes).

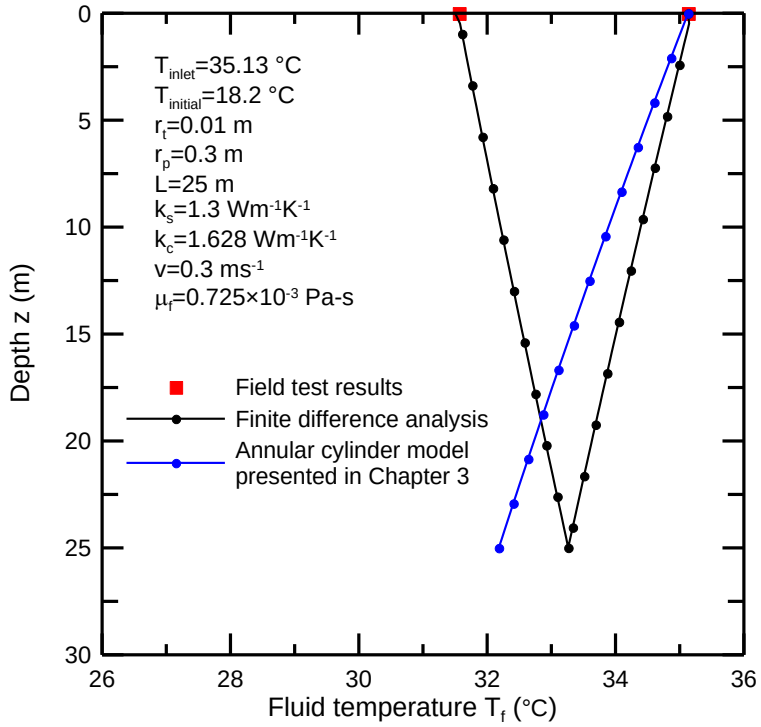

Figure 6-12 **Comparison of FD model prediction with circulation fluid temperature reported by Gao *et al*. (2008a, and 2008b)**

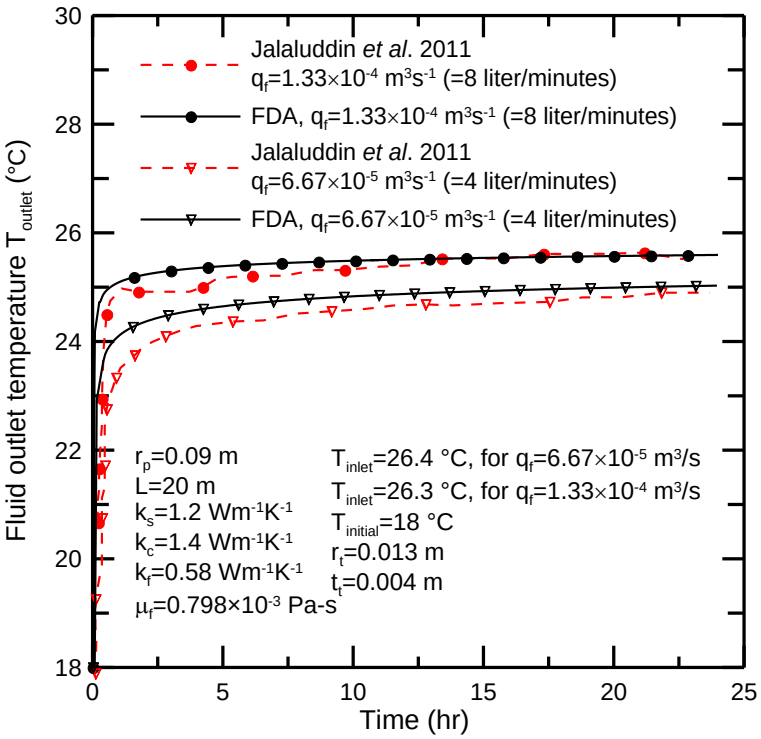

Figure 6-13 **Prediction of fluid outlet temperature during the first day of operation of a geothermal pile in field (Jalaluddin *et al*. 2011)**

6.2.5 Temperature Difference ΔT between Inlet and Outlet Points

To investigate the amount of power output obtained from the ground and estimate the thermal influence zone a heat exchange pile with real dimensions were considered in this research. A 25-m-long, 0.6-m-diameter concrete geothermal pile with an embedded U-shaped circulation tube was analyzed using the FD model described in this paper. A cylindrical soil domain (radius R = 12 m and depth Z = 30 m) with the pile in its center was considered for all analyses. Few trial analyses were performed (with different boundary distances) to ensure that the constant temperature boundary condition at the far boundaries was valid. An initial simulation, hereafter referred to as *base analysis*, was performed using a set of expected values for model input parameters (Table 6-2).

Temperature contour around the heat exchanger pile after 60 days of heat rejection from the pile to the surrounding ground is presented in Figure 6-14.

Table 6-2 **Input parameters used for base analysis**

Parameters	**Value**
Fluid circulation velocity	v = 0.1 m/s
Convective heat transfer coefficient (from ground surface)	h_g = 5 W/(m^{2}K)
Convective heat transfer coefficient (from top of the pile)	h_p = 0.01 W/(m^{2}K)
Initial temperature	$T_{initial}$ = 18˚C
Inlet temperature	T_{inlet} = 35˚C
Length of each vertical branch of the circulation tube	L_t = 24.8 m
Mass density of heat carrier fluid	ρ_f = 1000 kg/m^3
Pile length	L = 25 m
Pile radius	r_p = 0.30 m
Radius of circulation tube	r_t = 0.02 m
PVC tube thickness	t_t = 6 mm
Shank distance (i.e., center-to-center distance between two branches of the circulation tube)	s_t= 40 cm
Specific heat of heat carrier fluid	C_{pf} = 4190 J/(kgK)
Temperature in the medium above ground surface	T_{ag} = 23˚C
Thermal conductivity of concrete	k_c = 1.7 W/(mK)
Thermal conductivity of soil	k_s = 2.5 W/(mK)
Thermal conductivity of PVC tube	k_t = 0.41 W/(mK)
Thermal diffusivity of concrete	$\alpha_c = 0.9\times10^{-6}$ (m^2/s)
Thermal diffusivity of soil	$\alpha_s = 1.4\times10^{-6}$ (m^2/s)
Thermal diffusivity of PVC tube	$\alpha_t = 0.284\times10^{-6}$ (m^2/s)
Dynamic viscosity of fluid	μ_f = 0.725 m Pa. s
Thermal conductivity of fluid	k_f = 0.58 W/(mK)

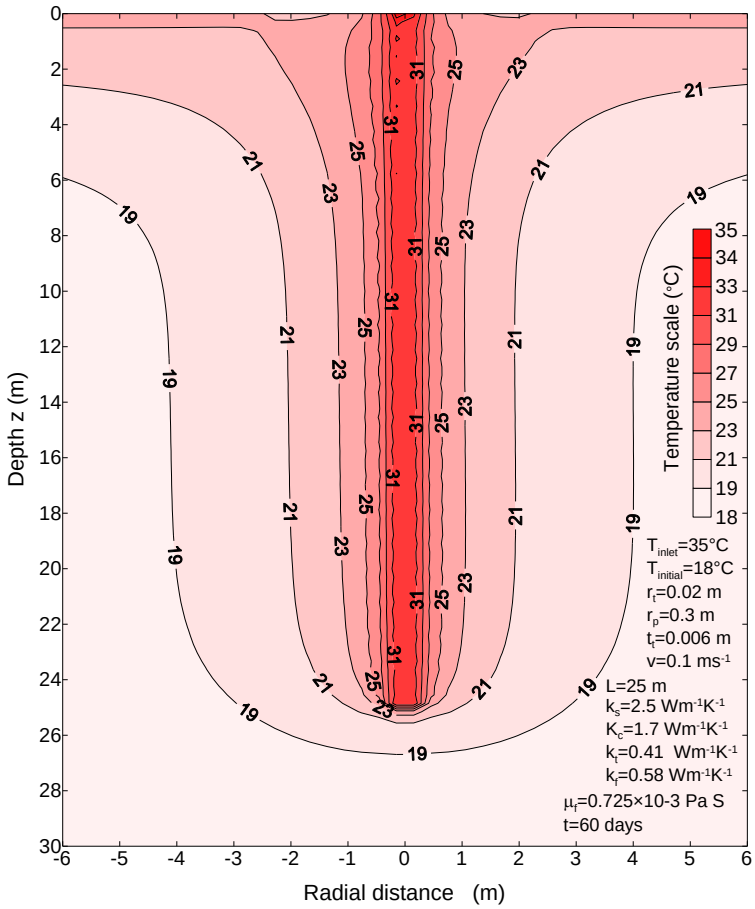

Figure 6-14 **Temperature contour (in °C) after 60 days of heat rejection from a geothermal pile**

The amount of heat transfer through a geothermal pile is related to the temperature difference ΔT (= $T_{inlet}-T_{outlet}$) between inlet and outlet points of the circulation tube. **Error! Reference source ot found.** shows the variation of ΔT with both real and normalized time expressed by Fourier number Fo (= $\alpha_s t/r_t^2$). Temperature difference ΔT, and thus the heat transfer rate, reduces sharply within a very short period of time (approximately 1 day) after the heat transfer starts and reaches nearly a constant value after 20 days of continuous heat rejection. Pile (concrete) and soil temperature increases with time as heat is rejected from heat carrier fluid to the surrounding media. Such temperature increase in the medium surrounding the heat source causes reduction in temperature gradient (heat flux) between the heat source and the medium surrounding it. The reduction in temperature gradient deters the rate of heat transfer from the heat carrier fluid and thus, temperature T_{outlet} at the fluid outlet point increases. Consequently, for a constant value of inlet temperature T_{inlet}, ΔT reduces with time and reaches a nearly constant value at a certain time (= 20 days for base analysis) after heat rejection starts.

Regression analysis is performed to describe a simple mathematical form for calculation of ΔT_b, i.e., the value of ΔT (in °C) as obtained from the base analysis, as a function of time t (in hours). **Error! Reference source not found.** (a) shows that Equation (6-14) can successfully predict result from the base analysis with a coefficient of determination $R^2 = 0.99$.

$$\Delta T_b(t) = 4.9(t)^{-0.12} \tag{6-14}$$

Note that Equation (6-14) is valid only for the set of input parameters used in the base analysis. The value of ΔT is expected to vary for any other combination of design, operational and site-specific parameters such as fluid circulation velocity v, radius of circulation tube r_t, pile radius r_p, initial temperature difference $\Delta\theta$ ($=T_{inlet}-T_{initial}$), thermal conductivity of concrete k_c, and thermal conductivity of soil k_s. Considering individual effects of the above parameters on ΔT, the following general expression is proposed for ΔT:

$$\Delta T(t) = \Delta T_b(t) \prod_N \left(\frac{x_N}{x_{Nb}} \right)^{a_N} \tag{6-15}$$

where N is an index that indicates total number of important input parameters (for this study N = 6), x_N takes the value of N^{th} input parameter (e.g., v, $\Delta\theta$, k_s, k_c, r_t, and r_p), x_{Nb} is the base value of the N^{th} input parameter (as reported in Table 6-2), and a_N is a regression coefficient for the N^{th} input parameter. In order to obtain the unknown coefficients a_N in Equation (6-15), additional FDAs are performed by varying one input parameter at a time while all other input parameters are kept constant at their base values reported in Table 6-2. The expression for a_N for each input variable x_N is determined through regression analyses of results obtained from these additional FDAs.

The resulting closed form expression for ΔT becomes:

$$\Delta T(t) = A(t)^{a_0} \left(\frac{v}{0.1} \right)^{a_1} \left(\frac{\Delta\theta}{17} \right)^{a_2} \left(\frac{k_c}{1.7} \right)^{a_3} \left(\frac{k_s}{2.5} \right)^{a_4} \left(\frac{r_p}{0.3} \right)^{a_5} \left(\frac{r_t}{0.02} \right)^{a_6} \tag{6-16}$$

The expressions for regression coefficients A, a_0, a_1, a_2, a_3, a_4, a_5 and a_6 in Equation (6-16) are summarized in Table 6-3.

Table 6-3 **Regression coefficients for different input variables**

Coefficients	Turbulent (*t* is in hours)	Laminar (*t* is in hours)
A	4.9	4.9
a_0	−0.12	−0.12
a_1	−0.9	−0.7
a_2	1	1
a_3	$0.35-0.02\ln t$	$0.35-0.02\ln t$
a_4	$\left(0.07+0.07\ln t\right)$	$\left(0.07+0.07\ln t\right)$
a_5	$-\left(0.05+0.01\ln t\right)\left(\frac{k_s/k_c}{1.47}\right)\left(\frac{r_p}{0.3}\right)$	$-\left(0.05+0.01\ln t\right)\left(\frac{k_s/k_c}{1.47}\right)\left(\frac{r_p}{0.3}\right)$
a_6	$-\left(1.15+0.05\ln t\right)$	$-\left(0.95+0.05\ln t\right)$

6.2.6 Geothermal Power Output

The total amount of heat exchange between a geothermal pile and ground over a certain period of thermal operation of the pile is defined as the energy output. Mathematically, the rate of energy extraction or rejection $P(t)$ (or power output) can be expressed as:

$$P\left(t\right)=\dot{m}C_{\mathrm{pf}}\Delta T\left(t\right)=\rho_{\mathrm{f}}v\pi r_{\mathrm{t}}^{2}C_{\mathrm{pf}}\Delta T\left(t\right) \tag{6-17}$$

Note that fluid circulation velocity v and radius of circulation tube r_t affect both $\dot{m}$ and $\Delta T(t)$. Therefore, the individual effects of v and r_t on $P(t)$ should be investigated separately. Although some field studies quantified the effect of circulation flow rate q_f (Gao *et al*. 2008a and 2008b, and Jalaluddin *et al*. 2011) on energy extraction (or rejection) rate $P(t)$, none of those studies could conclusively differentiate individual effects of v and r_t on $P(t)$. The circulation velocity v reversely affects $\dot{m}$ and $\Delta T(t)$ in Equation (6-17); an increase in v increases $\dot{m}$ but reduces $\Delta T(t)$. Figure 6-15(a) shows, for a set of input parameters, that power output (at time t= 7 days) per unit length of the pile increases with an increase in v and reaches to a constant value beyond a threshold value of v (= 0.3 ms^{-1}) that can be designated as an *efficient circulation velocity* for geothermal pile operation. P increases with increase in circulation tube radius r_t, and it is interesting to note that the value of *efficient circulation velocity* is independent of the value of r_t. Figure 6-15(b) shows power output (at time t = 7 days) per unit length of a geothermal pile as obtained from FDAs with a constant circulation flow rate q_f = 6.28×10^{-4} m^3s^{-1} (= 37.7 liter/minute). For a constant circulation flow rate q_f, different combinations of v and r_t can result in an increase (or decrease) in energy extraction (or rejection) rate. It is evident from Figure 6-15(b) that for a constant flow rate q_f, P increases as r_t increases, and thus, the effect of r_t on P is higher than that of v.

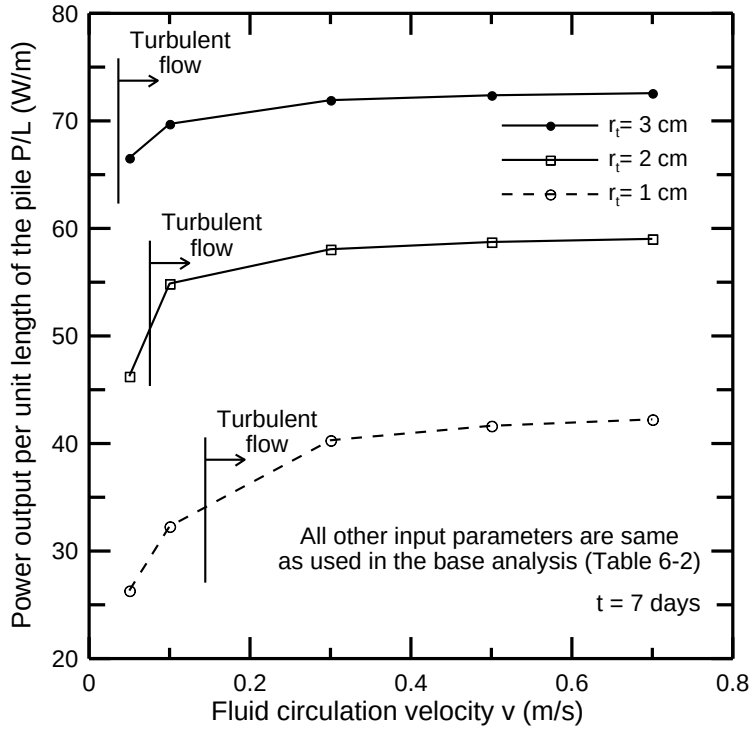

(a)

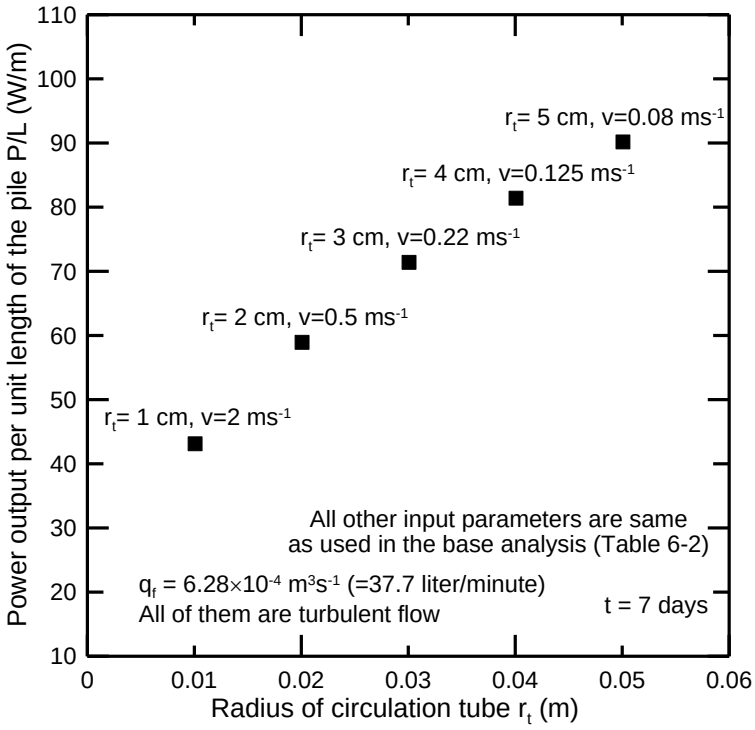

(b)

Figure 6-15 **Effects of circulation tube radius r_t and fluid circulation velocity v on power output: (a) variable circulation flow rate q_f and (b) constant circulation flow rate q_f**

The effect of flow characteristic (laminar or turbulent) on the amount of heat loss within the circulation fluid is also studied in this research (Figure 6-16). Figure 6-16 shows fluid temperature variation within a cross section (at the middle of the geothermal pile) of the inlet branch of the circulation tube. The high value of convective heat transfer coefficient in case of a turbulent flow results in minimal heat loss within the circulation tube; however, this is not the case for a laminar flow condition, which exhibits as much as a 10% (3.25°C) reduction of fluid temperature between the centerline and inside wall of the circulation tube.

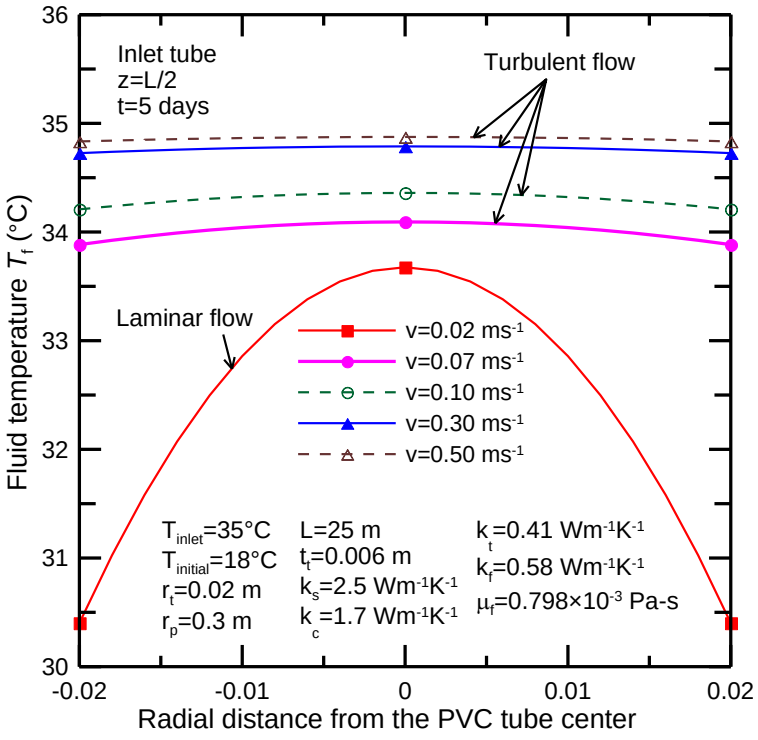

Figure 6-16 **Fluid temperature variations (within a cross section of circulation tube) with flow characteristics**

6.2.7 Closed-form expression to predict power output

The equations proposed for calculation of $\Delta T(t)$ [i.e., Equation (6-16) in combination with Table 6-3] can be used in conjunction with Equation (6-17) to predict energy output over a certain period of time of operation of a geothermal pile. Figure 6-17 compares power output (per unit length of the pile) values obtained from several FDAs (performed with different combinations of input parameters) and those predicted using proposed Equations (6-16), (6-17) and Table 6-3. The proposed equations can successfully predict (with a maximum difference of less than 10%) power output values for both short- and long-term operation (respectively, for t = 12 h and 60 days) of a geothermal pile with U-shaped circulation tube.

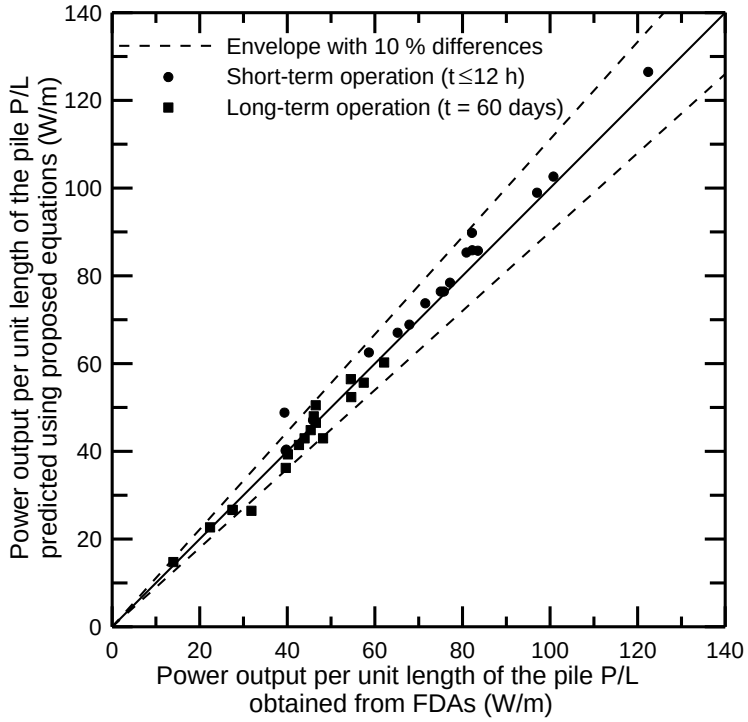

Figure 6-17 **Comparison between power output obtained from FDAs and that predicted using proposed equations [Equations (6-16), (6-17) and Table 6-3]**

6.3 Identification of sensitive uncertain parameters

The hierarchical effects of important design, operational and site specific parameters on increase in ground temperature at the pile-soil interface and on heat exchange efficiency of a geothermal pile at short- and long-term after the start of the thermal (heat rejection) operations are investigated through sensitivity analysis. Results from the sensitivity study are presented in the form of Tornado diagrams, which show relative influences of important model parameters on power output from a geothermal pile and on ground temperature increment (Figure 6-18 and Figure 6-19). Table 6-2 presents a set of expected input parameters. The maximum and minimum values considered for different input variables are shown in Figure 6-18 and Figure 6-19.

Figure 6-18(a) shows that the radius of circulation tube r_t, initial temperature difference $\Delta\theta$ and soil thermal conductivity k_s are, sequentially, the three most important parameters affecting the short-term thermal efficiency of a heat exchanger pile. The same three parameters, with a reverse hierarchy, are also found to be the most important parameters that affect long-term heat exchange efficiency of the system (Figure 6-18b). While the long-term heat exchange efficiency is most sensitive to k_s, this parameter has least influence among three most sensitive parameters on the short-term thermal efficiency of a geothermal pile. As can be seen from Figure 6-19, initial temperature difference $\Delta\theta$, soil thermal conductivity k_s, and radius of circulation tube r_t are the most sensitive parameters that affect ground temperature increment at the pile-soil interface. Note that k_s have opposite effects on energy output and ground temperature increment.

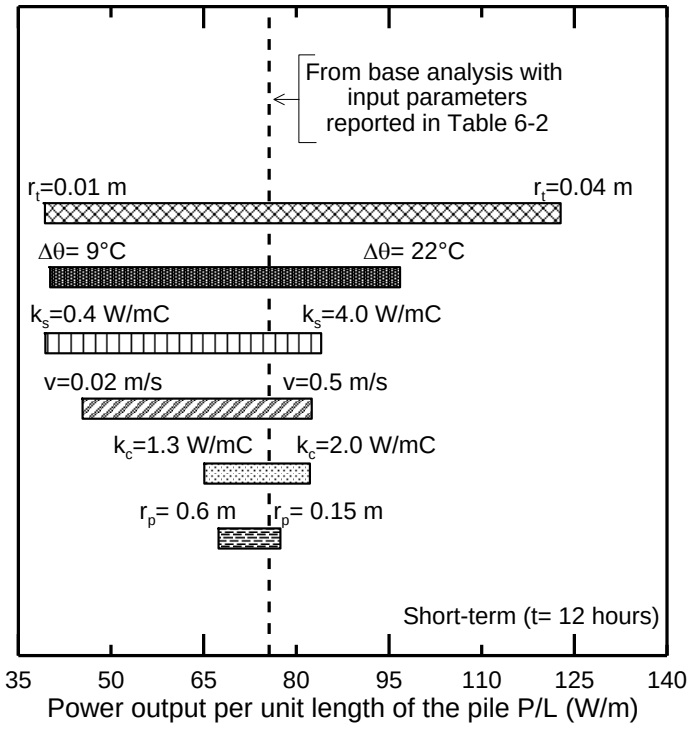

(a)

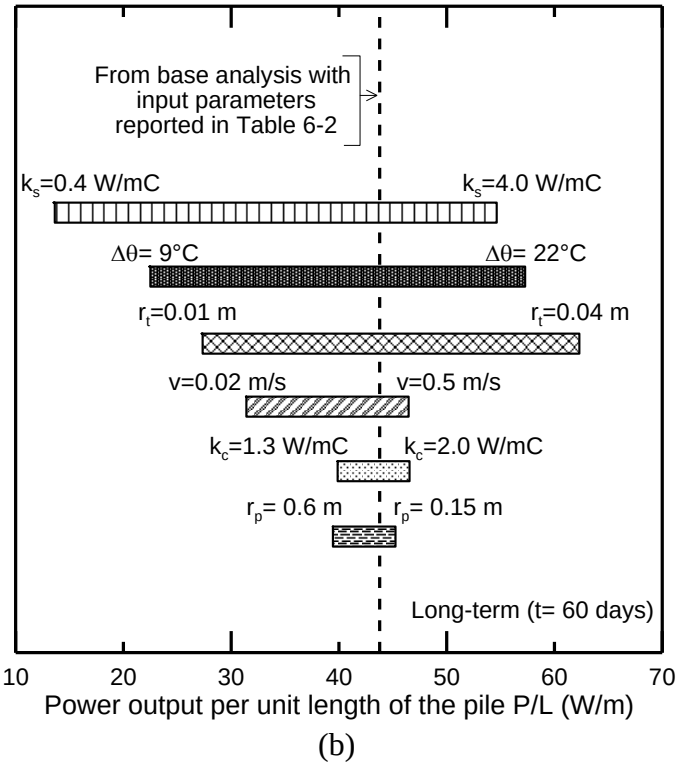

(b)

Figure 6-18 **Hierarchy of model parameters in affecting thermal efficiency of a geothermal pile: (a) after 12 hours of operation (short-term) and (b) after 60 days of operation (long-term)**

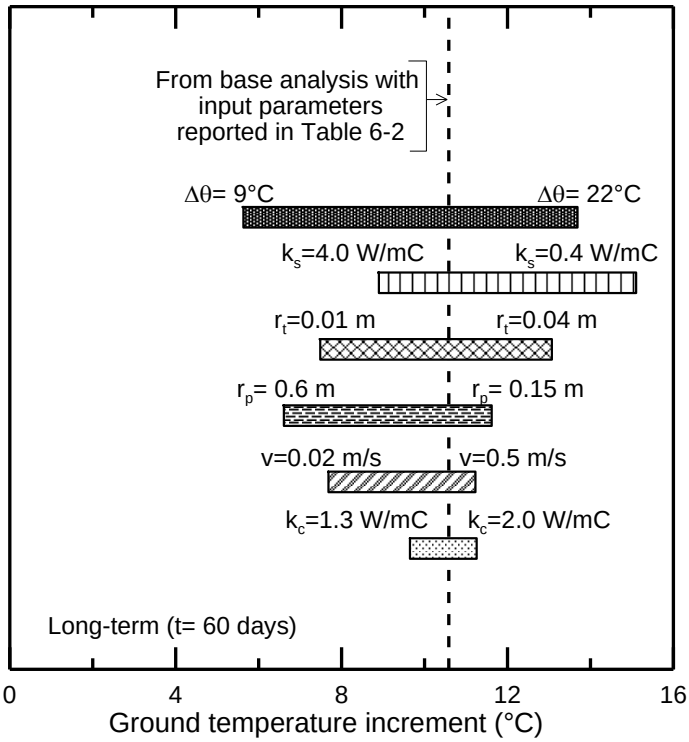

Figure 6-19 **Hierarchy of model parameters in affecting ground temperature increment at the pile-soil interface after 60 days of thermal (heat rejection) operation**

6.4 Summary and conclusion

Results from finite difference analyses presented in this chapter show that fluid circulation velocity and radius of circulation tube independently affect energy output from a geothermal pile. Beyond a short time after the start of heat transfer, thermal conductivity of concrete does not have any significant effect on heat exchange through geothermal piles; however, the effect of soil thermal conductivity on heat transfer efficiency increases with time. The effect of pile radius on energy output depends on the ratio k_s/k_c; increase in pile radius increases heat exchange efficiency for $k_s/k_c < 1$; the reverse is true when $k_s/k_c > 1$. A set of equations is proposed which can be used to calculate power output from a geothermal pile for any practical set of input variables. Comparison of heat loss within the fluid for laminar and turbulent flow shows that heat loss within the circulation tube is relatively higher in laminar flow and consequently thermal resistivity of fluid convection is higher in laminar flow. It is also evident from the results presented in this chapter that an increase in circulation velocity results in an increase in the harvested geothermal energy. Nevertheless, fluid circulation at higher velocity would require more electric power; therefore, optimum circulation fluid velocity would eventually depend on power efficiency of the circulation heat pump.

Effects of different design, operational, and site-specific variables on heat exchange efficiency of geothermal piles must be quantified for reliable and efficient design of geothermal piles. Although past studies focused on different aspects of heat exchange behavior of geothermal

piles, no theoretical or experimental studies have yet comprehensively quantified the relative variance of heat exchange efficiency and ground temperature increments due to individual or combined variation of different design, operational, and site specific parameters (Yavusturk 1999, Hamada *et al*. 2007, Gao *et al*. 2008a, and 2008b, Nam *et al*. 2008, Lamarche *et al*. 2010, McCartney *et al*. 2010, Abdelaziz *et al*. 2011, Suryatriyastuti *et al*. 2012, Rouissi *et al*. 2013, Ghasemi-Fare and Basu 2013a, 2013b, Ghasemi-Fare *et al*. 2014, and Jalaluddin *et al*. 2011). Sensitivity and reliability analyses show that thermal conductivity of soil, initial temperature difference between ground and circulation fluid, and radius of circulation tube are sequentially three most important parameters that affect long-term heat exchange performance of a geothermal pile.

7. Finite element analysis of heat exchange through geothermal piles

The second numerical modeling approach utilizes a finite elements (FE) simulation environment, COMSOL Multiphysics™ (COMSOL, 2013). Ozudogru *et al*. (2014a, 2014b) discusses the modeling methodology in detail along with the validation of the model. This numerical model utilizes 1D linear elements for simulating the fluid flow and heat transfer inside the circulation tubes, which in turn is fully coupled with the 3D geometry using the temperature field at the pipe exterior surface. The model can simulate the 3D transient and steady-state heat and mass transport processes in the borehole and heat exchanger pile with satisfactory accuracy and minimal computational effort.

7.1 Model development

The FE model considers several components of the GHE. These include the fluid in the pipes, the pipes, the grout, and the soil surrounding the heat exchanger. The lateral and bottom extents of the model are selected such that no thermal interaction occurs across the external boundaries. The diameter of the pipe elements is taken equal to the pipe outside diameter and these elements are identified as ‘pseudo pipes’. The actual physical representation of the pipes and the circulated fluid is modeled using linear elements that cross between the center-axes of pseudo pipes in each individual loop. Two dimensional elements are generated on a horizontal plane at the ground surface for all the model components and extruded downward to the bottom extent of the model. With the help of the linear pipe elements, the extrusion of the horizontal plane allows the creation of continuous line elements by establishing a connection between downward and upward pipes at the base of the GHE. Figure 7-1 provides more insight into the linear pipes and the pseudo pipe approach, presenting the 3D extruded geometry.

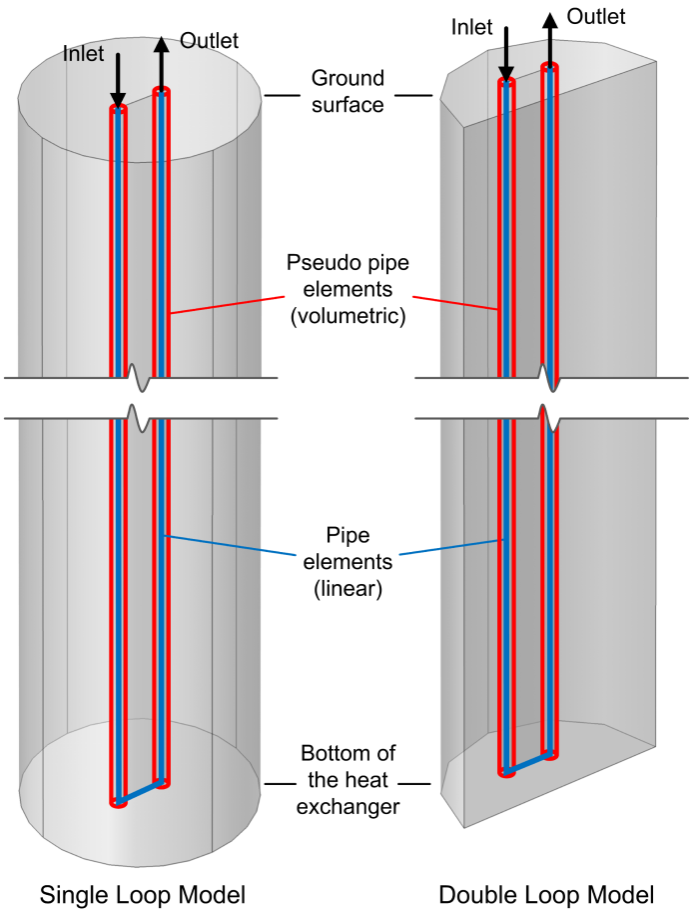

Figure 7-1 **The 3D geometry showing the linear and pseudo pipe elements**

The model utilizes swept finite element meshing in the vertical direction, and the mesh is optimized to minimize the number of elements. However, the reduction should not be done at the expense of obtaining numerical results with poor accuracy. Prior experience shows that, mesh refinement is required near the ground surface, soil/rock layer interfaces and the base of the heat exchanger, where larger vertical temperature gradients reside. Minimum refinement is necessary in mid-layers, where vertical temperature gradients are negligible. A similar meshing technique was used in a study by Marcotte and Pasquier (2008). In vertical GHE applications, since the heat transfer is predominantly in the radial direction and the vertical heat flow in the system is insignificant, it is a reasonable approach to distribute the swept mesh on the vertical axis with refinements only close to layer interfaces, or the depths where the extrusion of the 2D geometry was stopped. This procedure leaves coarser vertical mesh inside the soil layers. There may be exceptions to this approach in certain cases, such that, the first several meters below the ground surface should also be refined if the vertical temperature gradient caused by temperature variations near the ground surface will be considered in the model. The overall finite element mesh of a GHE with double loop configuration is shown in Figure 7-2.

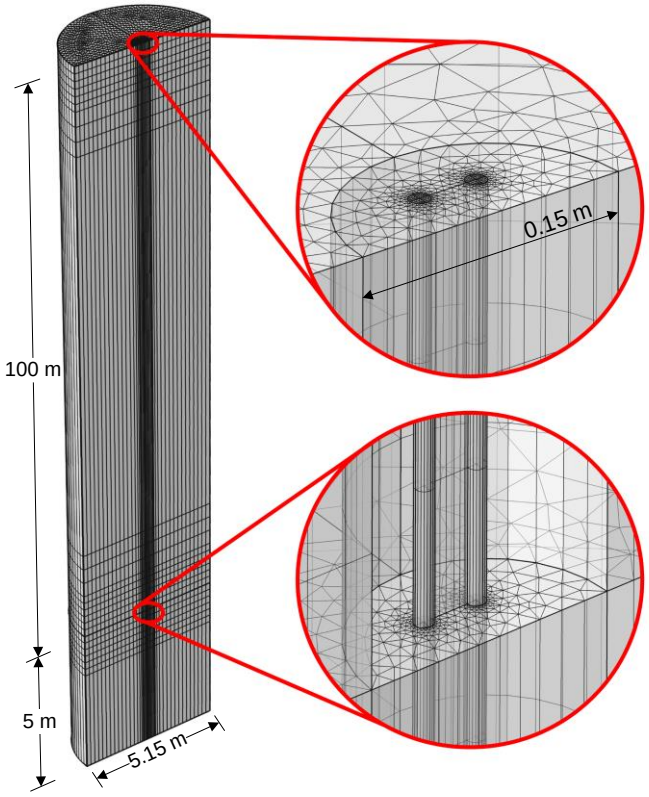

Figure 7-2 **Overall finite element mesh of a GHE with a double loop configuration**

7.2 Modifications

The FE model addresses the simulation of a GHE system by considering two problems: (1) the time dependent heat transfer problem in the volumetric domains, which is solved by calculating the temperature in each finite element mesh node; (2) the transient fluid flow and forced convection problems in the pipes, solved by evaluating the temperatures of the fluid and the pipe wall along the pipe axis. In the solid domains such as pseudo pipes, grout, and soil, pure conductive heat transfer is anticipated which is governed by the following equation assuming that there is no internal heat generation:

$$\rho c_p \frac{\partial T}{\partial t} + \nabla \cdot \left(-\mathbf{k} \nabla T \right) = 0 \tag{7-1}$$

Equation 7-1 is solved for temperature, *T*, making use of the temperature coupling between the solid domains and the linear pipe elements. Boundary conditions designate the behavior of the numerical model during runtime and are used to build the sparse matrix solved thereafter for estimating the temperature changes. Either no heat flux (insulation – Neumann), or prescribed

temperature (Dirichlet) boundary condition should be specified for the lateral and the bottom limits of the model. For the former case, it must be ensured that there is no temperature change at these boundaries while for the latter case, the heat flux on these boundaries must be zero throughout the runtime of the model. This can be achieved by setting the extent of the model at distances where heat exchange operations essentially have no effect. The Dirichlet boundary condition can only be used if the initial temperature of the ground is selected as a single value for all depths. For models with symmetrical geometry, no heat flux boundary condition is used on the symmetry plane.

The fluid flow and heat transfer problem in the pipes is physically modeled using linear elements, reducing the 3D flow problem to 1D. Modeling pipes as curves in 2D or 3D provides great advantage in computational efficiency over meshing and computing 3D pipes with finite diameter. The pipe flow problem is determined by solving the momentum and continuity equations given by Barnard *et al*. (1966). Heat transfer problem in the pipes is governed by the energy equation for an incompressible fluid flowing in a pipe:

$$\rho_{\mathrm{f}} A_{\mathrm{pi}} c_{pf} \frac{\partial T}{\partial t} + \rho_{\mathrm{f}} A_{\mathrm{pi}} c_{pf} \mathbf{u} \cdot \nabla T = \nabla \cdot A_{\mathrm{pi}} k_{\mathrm{f}} \nabla T + f_D \frac{\rho_{\mathrm{f}} A_{\mathrm{pi}}}{2 d_h} |\mathbf{u}|^3 + q'_{wall} \tag{7-2}$$

The second term on the right hand side corresponds to friction heat dissipated due to viscous shear. The radial heat transfer from the surroundings into the pipe is given by:

$$q''_{wall} = \frac{2\pi}{\frac{2}{\mathrm{Nu}\, k_{\mathrm{f}}} + \frac{\ln\left(d_{po}/d_{pi}\right)}{k_{\mathrm{p}}}} \left(T_{\mathrm{ext}} - T\right) \tag{7-3}$$

The Darcy friction factor in Equation 7-2 accounts for the continuous pressure drop along a pipe segment due to viscous shear, and it is estimated using the Churchill (1997) equation. Nusselt number is defined as the ratio of convective to conductive heat transfer across a boundary. For turbulent flow conditions, Nusselt number can be estimated using the correlation developed by Gnielinski (1976).

The external temperature outside of the pipes, T_{ext} corresponds to the temperature field computed in the volumetric domains that provides heat transfer coupling to the volumetric domains, considering the pipes as a line heat source. However, there is a limitation of this approach. Since the pipes are made of linear elements, the outer pipe wall temperature is coupled to the temperature field of the volumetric domains located at the pipe axis. This introduces estimation errors, because the temperature field of the volumetric domains to be coupled should be located at a distance of pipe outside radius from the pipe axis. Another downside of this simplification is that, it does not account for the heat capacity of the pipes. A ‘pseudo pipe’ approach was

developed as shown in Figure 7-1 to overcome these issues. The diameter of these cylindrical solid domains is equal to the pipe outside diameter. The assigned material properties are selected to ensure an accurate temperature coupling, while accounting for the heat capacity of the pipes, as well.

7.3 Model Performance

The FE model was validated using data recorded during one of the field thermal conductivity tests presented by Abdelaziz (2013). The test site was located at the Virginia Tech geotechnical testing facility. Four heat exchanger piles and a reaction pile were installed at the site and several thermal conductivity and thermo-mechanical loading tests were performed. Two types of thermal conductivity tests were conducted at the test site: (1) in accordance with ASHRAE method (Kavanaugh *et al*. 2001) and (2) following the Dutch perspective (Witte *et al*. 2002).

During the ASHRAE tests, the circulation fluid was heated with a constant heat rate using the electric heaters located at the testing trailer. Even though insulation was present, the piping above ground, (i.e. the pipes between the top of the pile and the trailer), was affected by variations in the ambient air temperature. This resulted in the application of a variable heat rate in the pile and requires advanced analysis techniques for estimating the thermal conductivity (Bandos et al. 2011). On the other hand, the Dutch test was conducted with a temperature controller device. The temperature difference between the inlet and outlet fluids was maintained at a constant value throughout the testing period, which provides a constant heat rate. The thermal conductivity test that followed the Dutch approach is considered in the verification study because such tests can be interpreted using available analytical heat transfer solutions, and thus provide a higher level of confidence in the verification study.

The test pile had a diameter of 25.4 cm and a length of 30.48 m. The pile was integrated with a single U-pipe, which had shank spacing (center-to-center) of 7.5 cm. The drilling log indicated that the first 12.8 m of the soil profile consists of a silty clayey sand layer, underlain by a shale layer. The shale layer extends beyond the depth of pile base. The subsurface profile at the test site and geometry of the test pile, as used in both numerical models, are shown in Figure 7-3.

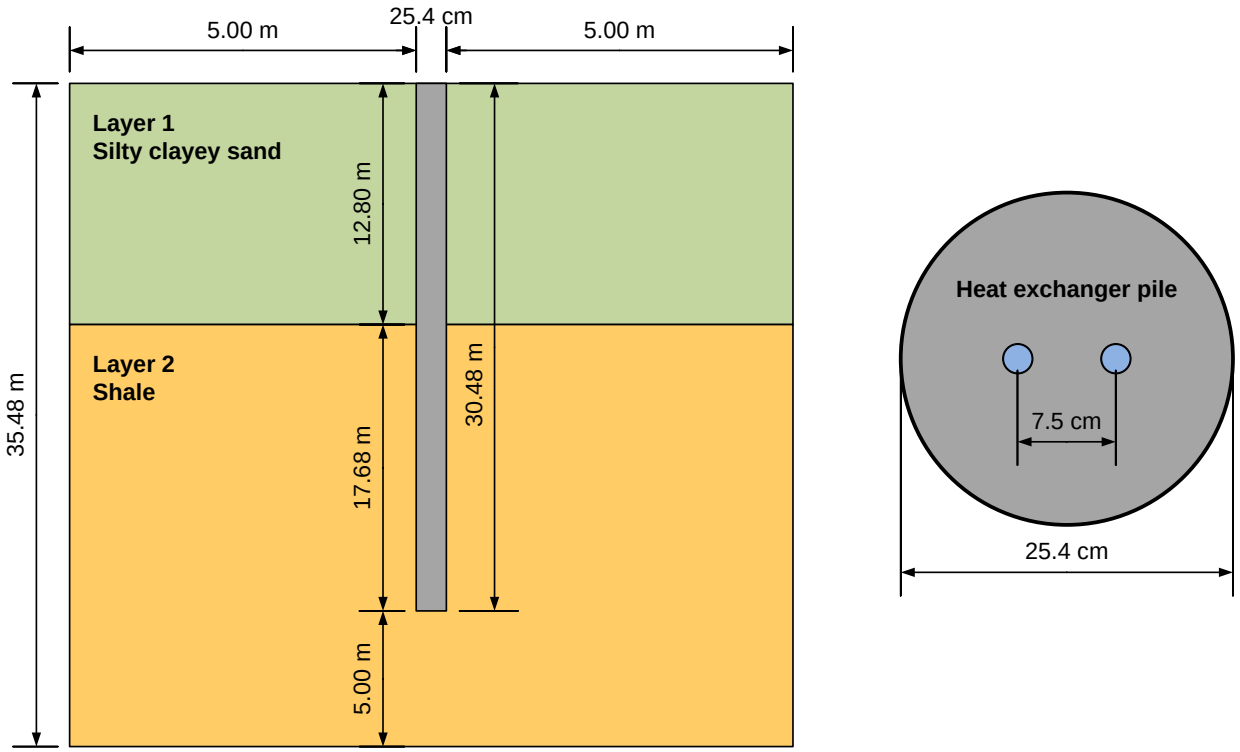

Figure 7-3 **Subsurface profile and geometry of the test pile**

The undisturbed ground temperature was measured as 14.7°C. The duration of the test was approximately 50 hours. Water was used as the circulation fluid and the temperature difference between the inlet and outlet was kept as 5.56°C during the entire testing period. This temperature change corresponds to a constant heat rate of 72 W/m.

The inlet and outlet temperatures were recorded during the field test. The results obtained from the numerical analyses are presented in Figure 7-4, along with the field measurements (Ozudogru *et al*. 2014b). The result of the verification study shows that both FD and FE model predicted the measured fluid temperatures with good accuracy. The coefficient of determination (R^2) of the FE model in comparison to the field measurements is evaluated as 0.995.

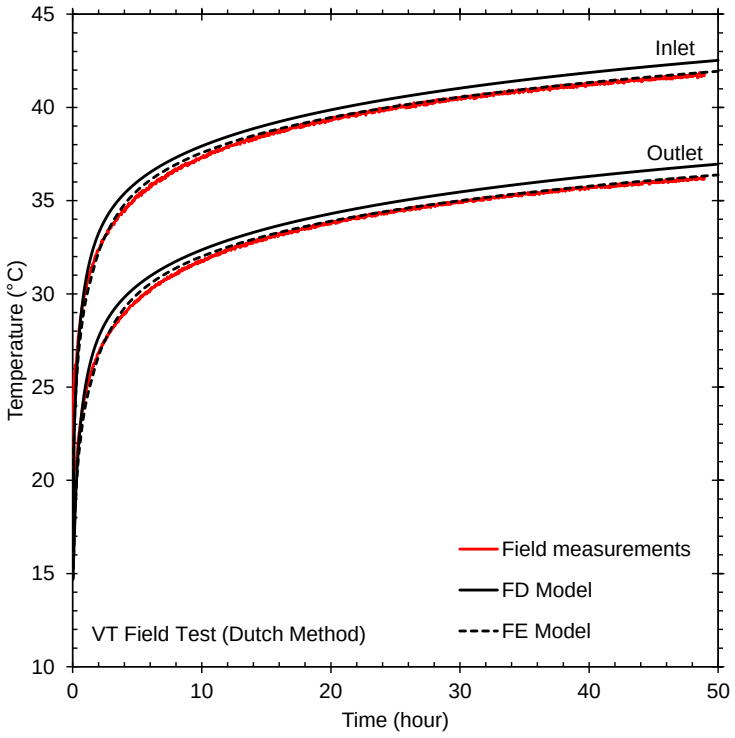

Figure 7-4 **Comparison of the FE model and the experimental test**

8. Finite element analysis of bridge deck deicing

A series of three-dimensional numerical analyses was performed to model the bridge deck heating process using the finite element software COMSOL Multiphysics in order to obtain a comprehensive understanding of how a heated bridge deck would interact with the environment. Relevant heat sources and heat transfer mechanisms need to be considered to determine how a bridge deck will respond to external temperature effects and to thermal regulations from the embedded tubing system. The bridge deck sketch provided in Figure 8-1 summarizes the relevant heat transfer mechanisms and a brief discussion of each component follows in the subsequent sections.

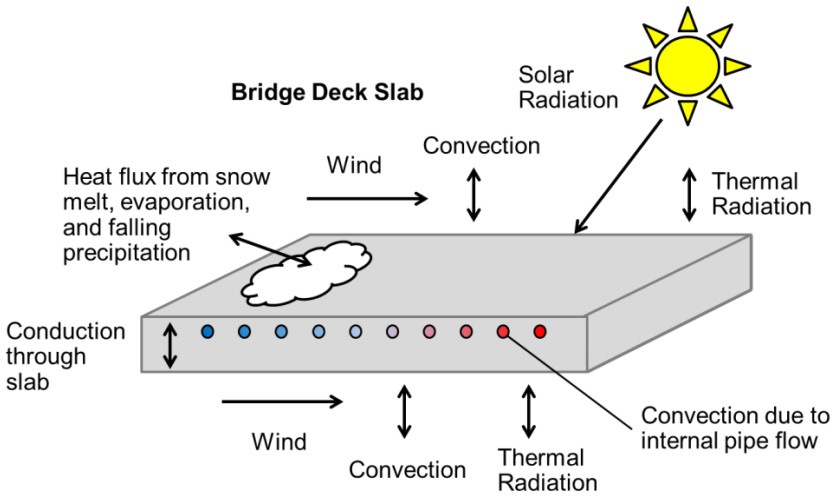

Figure 8-1 **Heat transfer considerations for bridge deck deicing**.

Conduction: Conduction occurs in and between the circulation tube, the concrete bridge deck, and any precipitation on the bridge deck. Conduction also occurs between falling precipitation and either the bridge deck or accumulated precipitation on the bridge deck.

Convection: The four types of convection are forced, natural, boiling, and condensation. The two of concern for the bridge deck are natural and forced. Natural convection occurs when the flow is driven purely by the buoyancy forces that are created from variations in the fluid's density, which is a result of temperature differences in the fluid. Forced convection occurs when the fluid flow is caused by some external means.

Radiation: Although radiation is one of the most important mechanisms in energy transfer between a bridge deck and its environment, it is also one of the most variable. A bridge deck absorbs solar radiation and longwave radiation from the atmosphere and also emits longwave radiation back to the atmosphere. The amount of radiation a bridge absorbs or emits is influenced by the temperature, cloud cover, the type of surface on the bridge deck, time of day, time of year and if the bridge deck is shielded or shaded.

Additional Heat Flux Considerations: Several additional heat fluxes impact the thermal response of the bridge deck during certain operations. Mass is added to the system whenever precipitation falls on either the bridge deck or on the accumulated precipitation that is already on the bridge deck. Unless the temperature of the falling precipitation is the same as that of the surface on which it is falling, the precipitation's heat energy will affect the thermal equilibrium of the system. This requires consideration of the falling precipitation's mass and specific heat. Evaporation and melting are phase change processes that also require significant heat energy. Evaporation may take place during snow melting operations and during concrete curing.

8.1 Model development

From the field test results, it became evident that these systems must be turned on in advance of a storm to operate effectively. As such, the vast majority of system operation will occur before any precipitation falls, which allows for the omission of directly considering snow melt in these models. This is a great advantage as snow melt is an extremely complicated and computationally expensive process to numerically model. Also due to the fact that these systems must be turned on before precipitation arrives, a metric that can be used to judge their success is how long it takes the surface temperature to reach 0^oC, if it reaches 0^oC at all. By following this approach, the following model was developed.

8.1.1 The governing physics included in the model

The physics included in this model have been discussed previously; however, the exact equations are given below:

The heat transfer through the slab is governed by the following differential equation, assuming there is no internal heat generation:

$$\rho c_p \frac{\partial T}{\partial t} + \nabla \cdot (-\mathbf{k}\nabla T) = 0 \tag{8-1}$$

Several boundary conditions can exist. For completely insulated, or adiabatic surfaces of the bridge deck, a Neumann boundary condition exists, which specifies there is no heat flux at the surface:

$$q" = (-\mathbf{k}\nabla T) = 0 \tag{8-2}$$

The top and bottom deck surfaces, unless insulated, are exposed to the environment, in which case they will experience both radiation and convection. Convection at the surface is expressed as:

$$-\mathbf{n} \cdot (-\mathbf{k}\nabla T) = h \cdot (T_{ext} - T) \tag{8-3}$$

Radiation between the surface and the environment is expressed as:

$$-\mathbf{n} \cdot (-\mathbf{k}\nabla T) = \varepsilon\sigma(T_{ext}^4 - T^4) \tag{8-4}$$

8.1.1.1 Modeling of fluid circulation and fluid circulation tubes

Directly modeling fluid flow is a computationally expensive process and being able to directly model the direct flow of the fluid through the pipes is not within the objectives of the model. Rather, the transfer of thermal energy between the fluid and the slab is of concern. Furthermore, the circulation tubes have very small thicknesses relative to the overall size of a bridge deck slab and having to discretize their domain would add additional computational burden. Thus, simplifications following the methodology found in Abdelaziz (2013) were used that allowed for both the fluid and circulation tubes to be accounted for indirectly.

8.1.2 Geometry, material properties, and domain discretization

The bridge deck slab modeled in the analyses is shown in Figure 8-2. The dimensions of the slab are 6.6 m x 4.5 m x 0.25 m. The hydronic piping selected was 1.9 cm OD / 1.3 cm ID PEX pipe. Warm fluid was circulated through the circulation tube at a constant flow rate and the temperature progression within the deck was evaluated. Water with 25% propylene glycol was used as the carrier fluid. The temperature of the inlet fluid is a reflection of the in-situ ground temperature. Inlet fluid temperature was kept constant throughout the analyses even though this temperature is likely to vary slightly as a result of colder fluid being injected into the ground. The material properties used are given in Table 8-1.

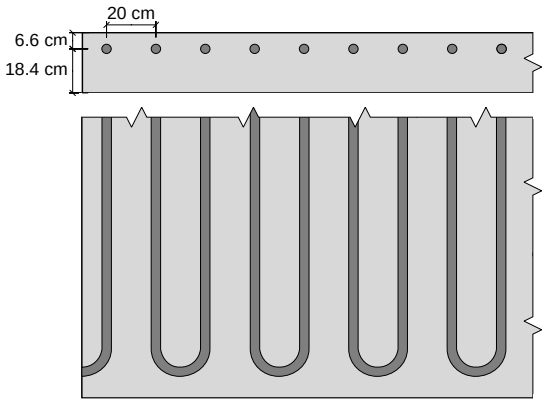

Figure 8-2 **Bridge deck slab used in the analyses and layout of the circulation tube.**

Table 8-1 **Summary of the material properties used in the numerical analyses**

Property	Material	Value
Density	Concrete	2408 kg/m^3
	Carrier Fluid	1041 kg/m^3
	Air	1.23 kg/m^3
Heat Capacity	Concrete	880 J/kg·K
	Carrier Fluid	3691 J/kg·K
	Air	1006 J/kg·K
Thermal Conductivity	Concrete	1.44 W/m·K
	Carrier Fluid	0.48 W/m·K

	Tube	0.41 W/m·K
	Air	0.0239 W/m·K
Kinematic Viscosity	Air	1.315×10^{-5} m^2/s
Surface Emissivity	Concrete	0.91
Dynamic Viscosity	Carrier Fluid	0.00273 kg/m·s
Prandtl Number	Air	0.72

The rebar was not modeled in the analyses because relative to the concrete, its volumetric mass and heat capacity is small and its thermal conductivity is much higher. In addition, the diameter of the rebar is very small and would require an extremely fine mesh, significantly increasing computation time. Preliminary analyses have been performed with and without rebar. It was concluded that the effect of rebar was negligible.

The domain was meshed using tetrahedral elements. Though the number of elements varied slightly depending on the circulation tube spacing, all models contained around 1.3 million elements. The geometry as built and a zoomed in section below show the completed meshing.

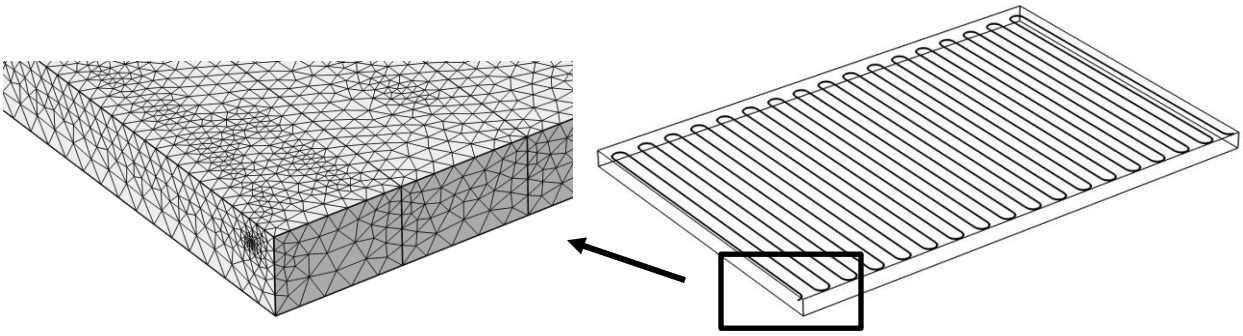

Figure 8-3 **A portion of the discretized domain**

8.2 Parametric analysis methodology

The analyses considered a variety of tube spacing, inlet fluid temperatures, flow rates, wind speeds, ambient temperatures and thicknesses of concrete cover over the circulation tubes. The ambient temperature was kept constant throughout the analyses. Variation of these parameters allowed us to evaluate the respective effects of different factors on the bridge deck heating process.

The analyses were limited to the heating process of the bridge deck while the ambient temperature was kept constant and the melting of the snow was not included. The main purposes of these assumptions were to maintain simplicity in the computations and also to develop a baseline for the energy demand to bring the bridge deck to above freezing temperatures. This condition can be considered as the case when the bridge deck is heated to above freezing temperatures preemptively before snowfall. In this case, the bridge deck will remain snow-free after precipitation if the heat injection compensates the latent and evaporative heat demands from snow melting after the start of precipitation.

A total of 256 models were analyzed where different model parameters were systematically varied as summarized in Table 8-2. The center-to-center spacing of the circulation tubes for the base case was set at 20 cm and the centerline of the tubes was 6.6 cm below the deck surface which corresponds to a concrete cover of 5.7 cm above the tubes as recommended (ACI 2011). Fluid with 12°C inlet temperature was circulated at a flow rate of 11.4 L/min. The initial slab temperature is -2°C and no wind was considered for the base case.

Table 8-2 **Model parameters used in the numerical analyses**

Tube Spacing (cm)	Wind Speed (m/s)	Concrete Cover (cm)	Inlet Fluid Temperature (°C)	Ambient Temperature (°C)	Flow Rate (L/min)	Number of Runs
20	0	5.7	12	-2.0	11.4	Base Case
15, 20, 25, 30	0	3.7, 5.7, 7.7, 9.7	6, 8, 10, 12, 14, 16, 18, 20	-2.0	11.4	127
15, 20, 25, 30	1, 2, 4	5.7	6, 8, 10, 12, 14, 16, 18, 20	-2.0	11.4	96
15, 20, 25	6	5.7	6, 8, 10, 12, 14, 16, 18, 20	-2.0	11.4	24
20	0	5.7	12	-0.5, -1.0, -1.5, -2.0, -2.5	11.4	4
20	0	5.7	12	-2.0	6, 8, 15, 20	4

8.3 Results

There are many different ways in which to analyze the results of these analyses. The first of which is by looking at an energy distribution. For example, consider the base case. The total amount of energy injected into the slab over time is shown in Figure 8-4. Of that total energy, the amount required to heat the slab and the amount of energy that was lost due to radiation with the ambient environment are separated. During the first several hours, almost all of the injected energy was being used to heat the bridge deck. But after the surface started to heat, more and more energy was lost to the environment.

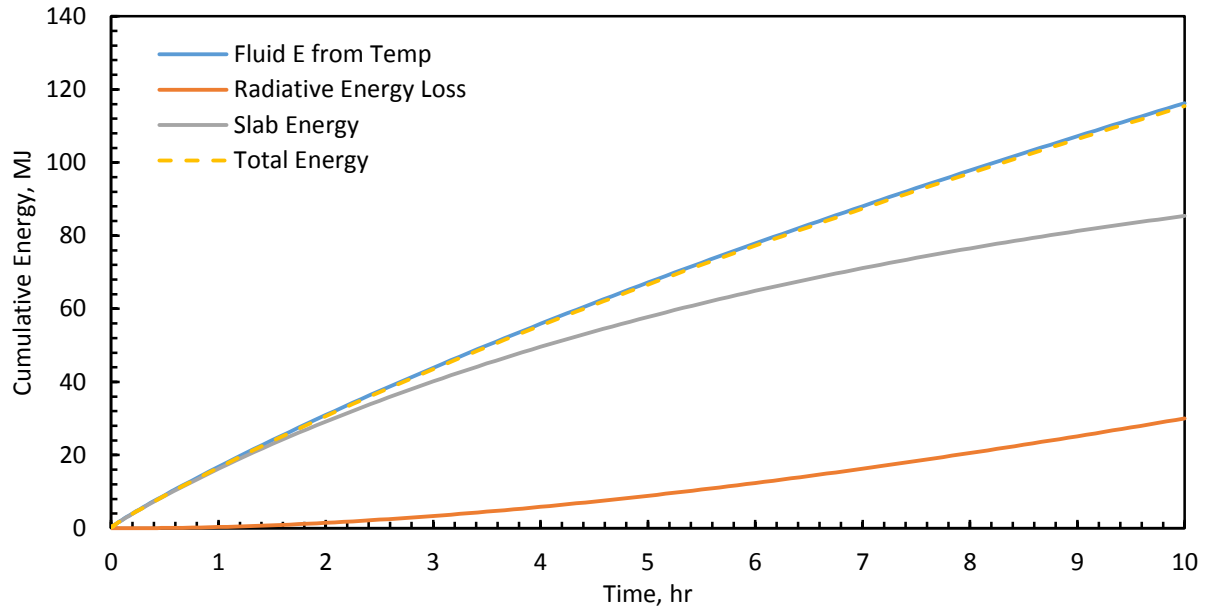

Figure 8-4 **Cumulative energy distribution over time**

The rate at which energy was transferred to the slab and the rate at which it was lost can also be plotted, as shown in Figure 8-5.

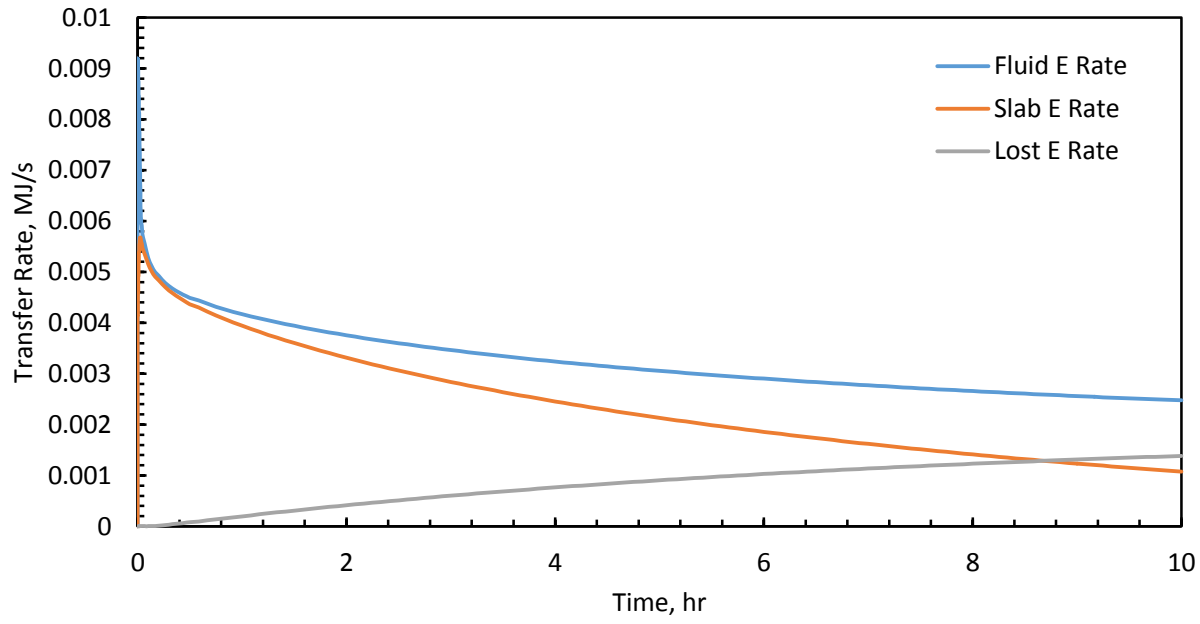

Figure 8-5 **Rate of energy transfer**

Though energy is a valuable measurement to have, and will be needed for examination of the foundation and whether or not it is capable of supplying enough energy, temperature is a more valuable metric in judging system performance as it can directly be correlated with success. That is, because the freezing point of snow is 0°C, any surface temperature greater than 0°C will be

considered a success. Temperature profiles along the vertical section at the mid-point between two tubes are shown in Figure 8-6 for different times into heating. This centerline section represents the most distant point from each tube in the horizontal direction. It is seen that the temperatures rise fastest near the tube elevation within the slab. The slab gets progressively warmer with higher temperatures expectedly at the surface in comparison to the slab base. In this analysis, the top 8.5 cm of the deck slab is greater than 0°C at the end of 2 hours of heating with 12°C circulation fluid.

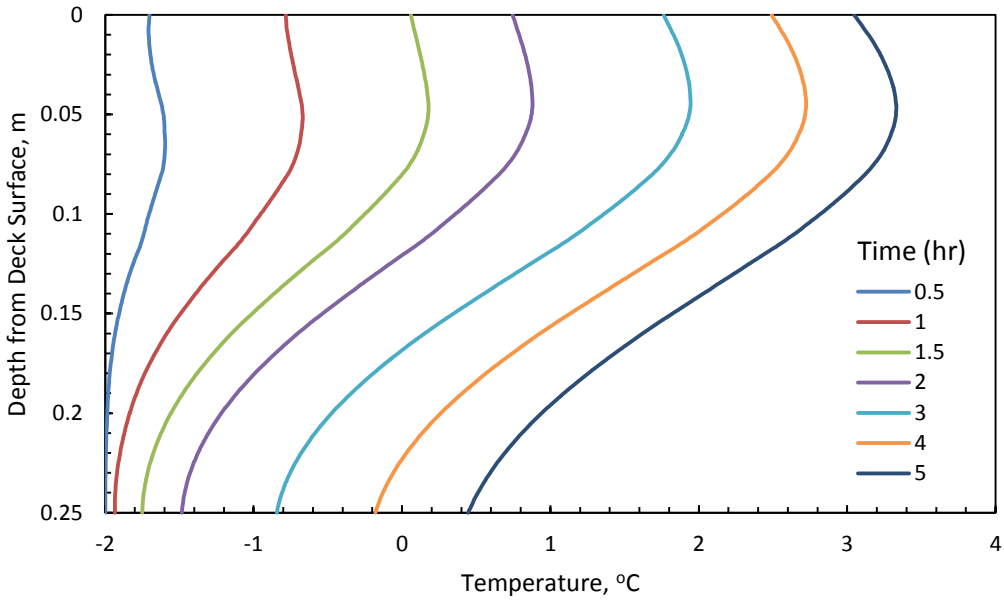

Figure 8-6 **Temperature profiles through the deck between two tubes**

Progression of temperatures for the base case analysis is shown in Figure 8-7 as a result of fluid circulation with inlet temperature of 12°C at a flow rate 11.4 L/min (base case). This figure shows the deck surface temperatures above the circulation tube and in-between the tubes in comparison to the average surface temperature. It is seen that the surface temperature increases from the initial value of -2°C more rapidly above the tube location than the mid-point between the tubes, taking 0.71 and 1.47 hours, respectively, to reach 0°C.

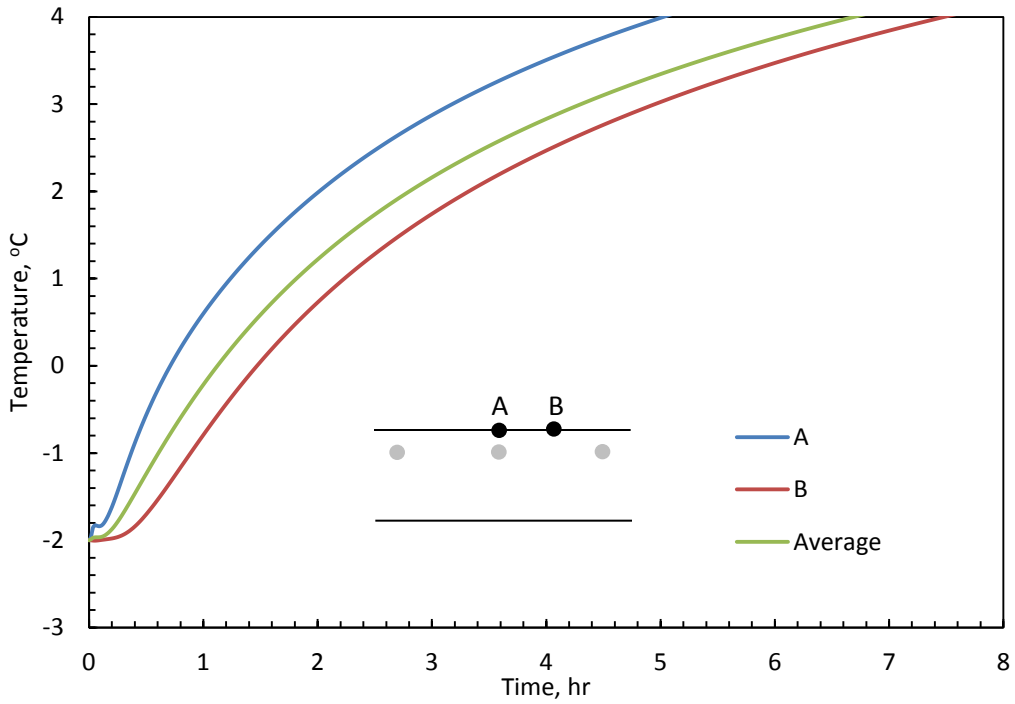

Figure 8-7 **Temperature increase above and between tubes as compared with the average surface temperature increase for the base case.**

The effect of wind speed is demonstrated in Figure 8-8 where the progression of average deck surface temperatures is shown for cases with various wind speeds. As expected, the convective cooling effect of the wind inhibits the heating process as it removes heat from the bridge deck slab, while the ambient temperature remains constant. It takes 1.12, 1.26, 1.39, 1.68 and 2.06 hours for average deck surface temperatures to reach 0°C for conditions with 0, 1, 2, 4 and 6 m/s wind speeds respectively. On the contrary, it takes 1.81, 2.22, 2.67, 4.08 and 8.18 hours to reach 1°C average deck surface temperature for the same wind conditions. These results shows the significance of wind conditions during a deicing process which can be critical for determining the required ground-source heating capacity for a given performance level. It is also instructive to note that heating the bridge deck slab takes increasingly longer at higher wind speeds. This is evidenced by the temperature increase curves getting asymptotically horizontal with increasing wind speeds as shown in Figure 8-8. For example the bridge deck slab subjected to 6 m/s wind does not get any warmer than 1°C with prolonged heating up to 8 hours. This indicates that the heat injection rate for this specific inlet temperature is more or less balanced with the heat removed by convection from wind at this speed.

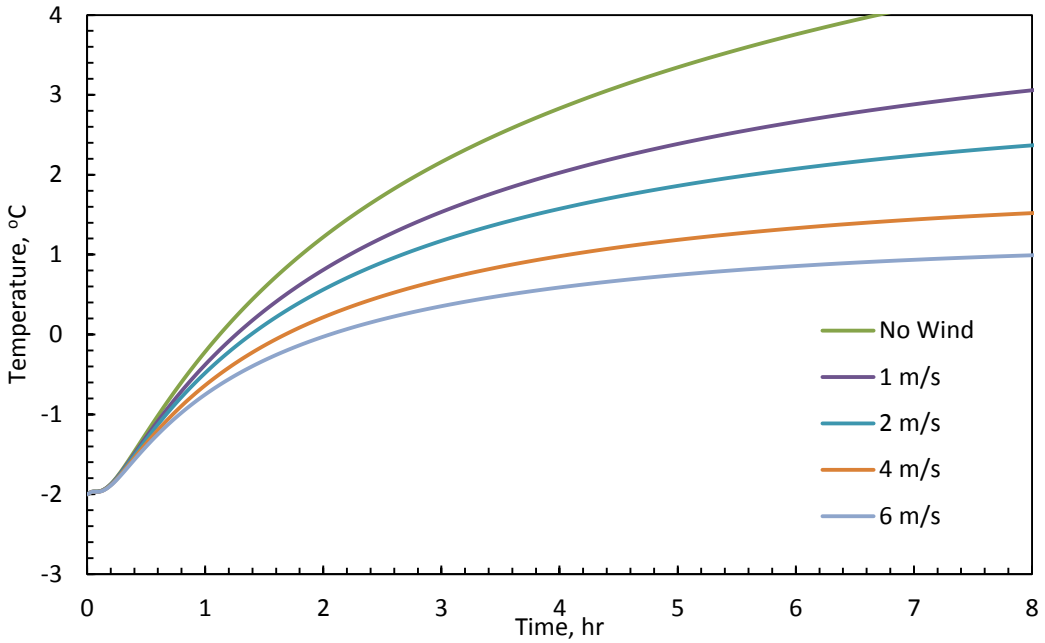

Figure 8-8 **Effect of wind speed on the average surface temperature during heating for an inlet fluid temperature of 12°C**

By determining the amount of time it takes the average surface temperature of each case to reach zero, many cases can be compared at once. Shown below is a graph of the amount of time it takes the average surface temperature to reach 0°C for a 20cm tube spacing with various wind speeds. Observe that as the inlet fluid temperature increases, the effect of wind speed on the amount of time it takes to heat decreases.

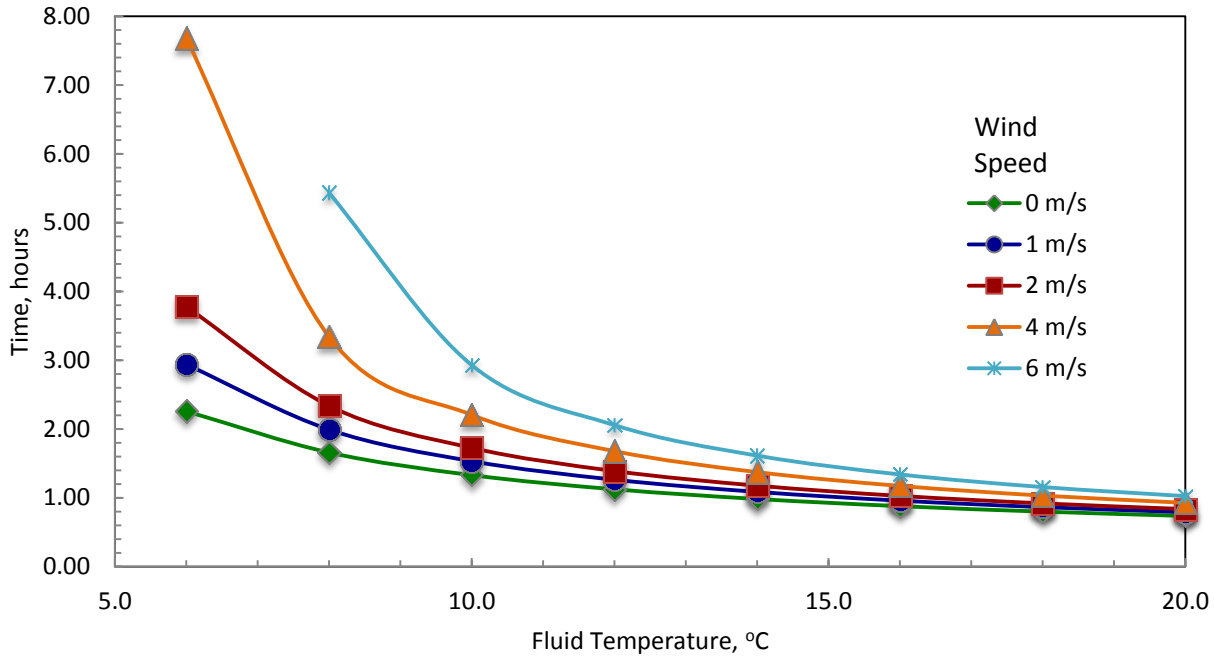

Figure 8-9 **Effect of wind speed on deck surface heating**

The effect of circulation tube spacing is also investigated, as this is one of the primary design factors. The heating durations required to reach 0°C average deck surface temperature are shown in Figure 8-10 for different tube spacings. In this case, the concrete cover thickness above the tubes is 5.7 cm and ambient air temperature is -2°C. Tube spacing of 15 cm results in 19-30% reduction in heating time to reach 0°C average deck surface temperature in comparison to 20 cm tube spacing for different inlet fluid temperatures. Similarly, 25 cm and 30 cm tube spacings result in 20-38% and 41-85% increase in heating periods, respectively, in comparison to 20 cm tube spacing. As shown, it is possible to heat the bridge deck with these tube spacings within reasonably short time periods for the range of considered inlet fluid temperatures.

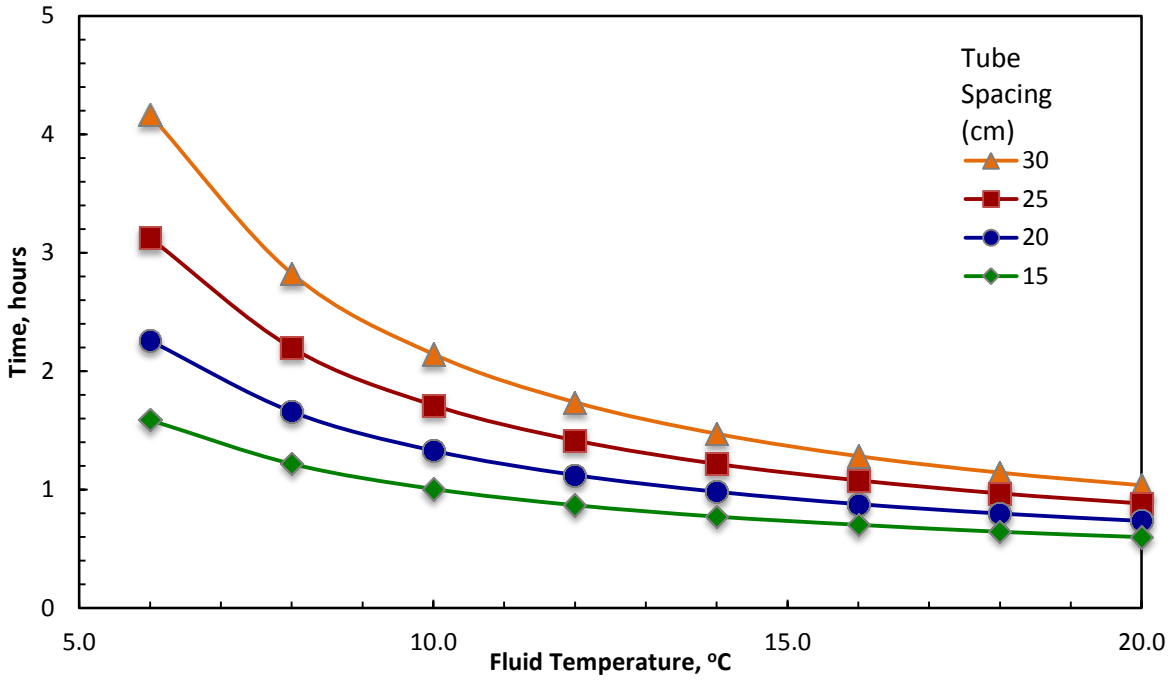

Figure 8-10 **Effect of tube spacing on the amount of time it takes to heat the surface for no wind and an ambient temperature of -2°C**

Thickness of the concrete overlay above the circulation tube can vary due to a variety of project considerations. Therefore our analyses also included cases where the thickness of the concrete cover was varied from the base case value of 5.7 cm. The results for the heating time to reach 0°C average deck surface temperature are shown in Figure 8-11 for different concrete cover thicknesses. It appears that every centimeter of cover thickness adds about 10-20 minutes to the bridge deck heating for the above metric. Within this given range, thickness of the concrete cover has a smaller effect on heating time for closer spaced tubes in comparison to more distantly spaced ones.

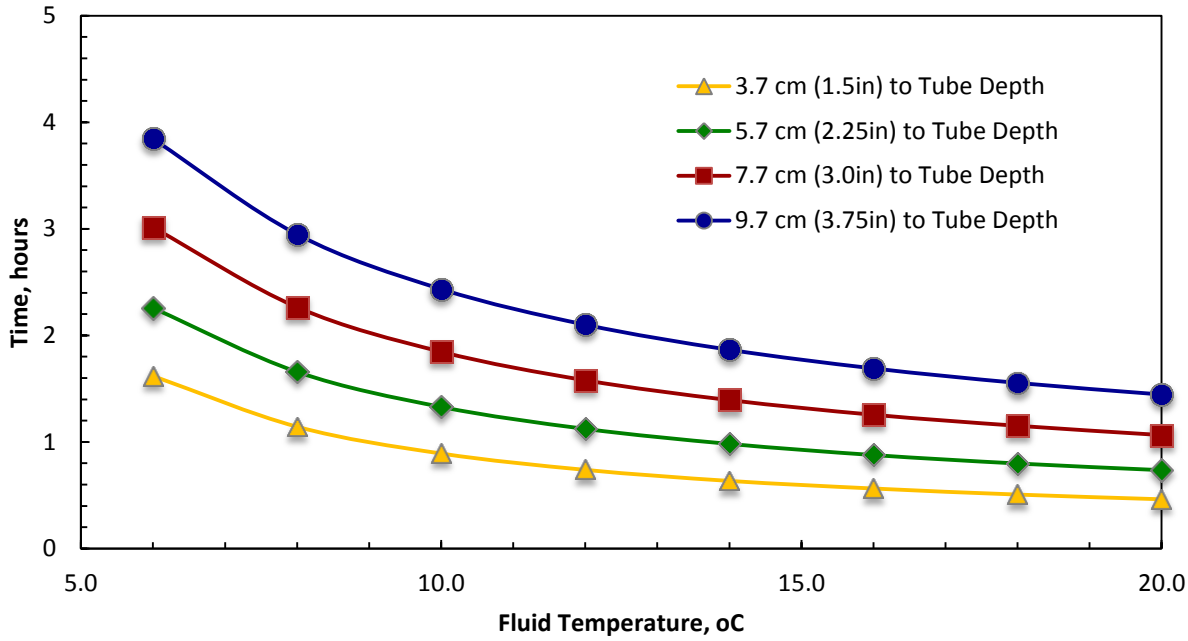

Figure 8-11 **Effect of concrete thickness above tube on the amount of time it takes to heat the surface for a 20cm tube spacing with no wind**

The results for the effect of the fluid flow rate on deck heating are presented in Figure 8-12. Several analyses were performed for 6, 8, 15 and 20 L/min flow rates in comparison to the 11.4 L/min in the base case. The effect of flow rate is relatively minor and slower flow rates result in longer times to heat the bridge deck. A flow rate of 6 L/min results in a 13% increase in heating time whereas 20 L/min results in a 6% decrease in heating time compared to 11.4 L/min flow rate.

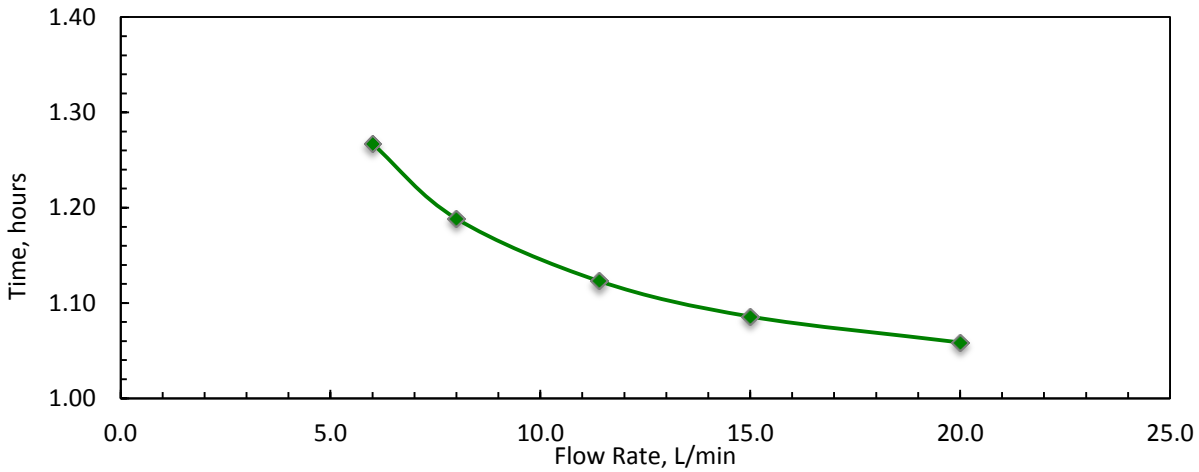

Figure 8-12 **Effect of fluid flow rate on the amount of time it takes to heat the deck surface with 20cm tube spacing, -2°C ambient temperature, and no wind**

Analyses were also performed to investigate the effect of ambient temperatures on bridge deck heating performance. This results of this for various tube spacing and no wind is shown in Figure 8-13. It was seen that every degree °C reduction in ambient temperatures resulted in 40-50% increase in the time required to raise the average deck surface temperature to 0°C.

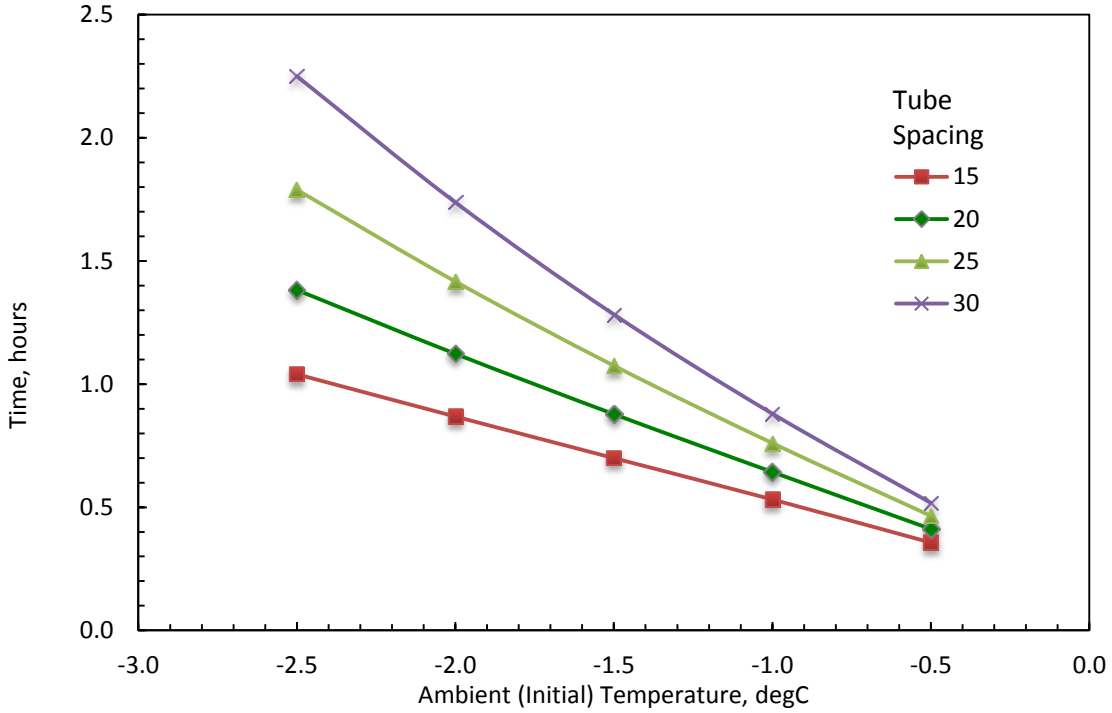

Figure 8-13 **Effect of ambient (initial) temperature on the amount of time it takes to heat the deck surface for different tube spacings with no wind.**

8.4 Conclusions

From the results of the numerical study, the following conclusions were drawn:

1) A bridge deck heating system with heat energy supplied by energy piles alone (i.e. without the aid of a heat pump) is capable of heating the bridge deck to above freezing temperatures in a reasonably short amount of time, well within the range of storm forecast predictions.
2) The above finding is conditional on certain environmental parameters being met. For example, colder areas experience temperatures much lower than -2^{o}C and have average ground temperatures of 10°C or less, such a system would not be feasible without the aid of a heat pump. However, in many warmer areas that experience milder winters and have a higher average ground temperature, these systems are more feasible for occasional extreme environmental conditions where deicing is required. Thus the designer must carefully consider the objective of the system and understand the system's limitations.

3) The major limitation due to the coupling of higher heating demand and colder ground temperatures at colder environments can be overcome by collecting heat from the bridge deck slab in the summer and injecting into the ground to be reclaimed in the winter when needed. Thermal storage will result in higher circulation fluid temperatures in the winter, which can reduce required heating durations as shown in the presented analyses.
4) Certain design factors such as closer spacing and less concrete cover can aid in increasing the efficiency of a system by decreasing the amount of time it takes the deck to heat. Increasing the fluid flow rate can also increase the efficiency of a system but its effects are not as significant.

9. Cost analysis

9.1 Introduction to life cycle analysis (LCA)

In order to compare the feasibility of the ground-coupled bridge deck deicing system with the conventional deicing systems, a life cycle analysis (LCA) framework was developed for the deicing salt. LCA is a quantitative method, which aims to assess environmental and social impacts through the whole product life cycle. According to International Organization for Standardization (ISO 14040; ISO 14044, 2006), LCA is a "compilation and evaluation of the inputs, outputs and the potential environmental impacts of a product system throughout its life cycle." The Society of Environmental Toxicology and Chemistry (SETAC) also defined LCA as "a process to evaluate the environmental burdens associated with a product, process, or activity by identifying and quantifying energy and materials used and wastes released to the environment; to assess the impact of those energy and materials used and releases to the environment; and to identify and evaluate opportunities to affect environmental improvements."

9.2 Steps of a LCA

LCA consists of four steps: (1) Goal and Scope Definition, (2) Inventory Analysis, (3) Impact Assessment, and (4) Interpretation (Figure 9-1). Below is a description these steps in the deicing salt LCA framework

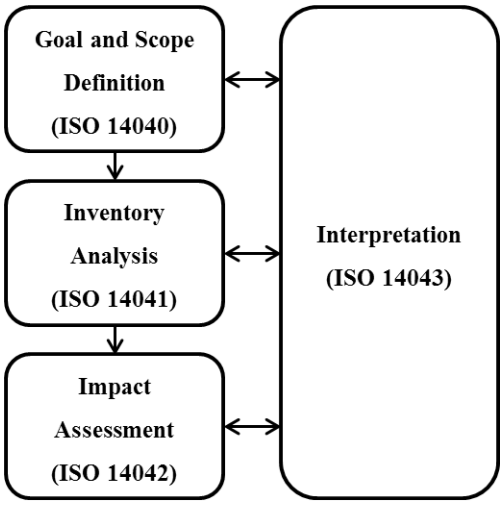

Figure 9-1 **LCA Steps according to ISO 14040**

1) Goal and Scope Definition:

In this step, the scope and the boundary of the LCA is defined as well as the functional unit. The type of methods, impact categories, and set of data that needs to be collected are also identified. System boundary and functional unit definition are important elements of this component. Functional unit is a description of a product or system to be assessed. The functional unit aids in comparing the results of a LCA of a product with a similar product. The functional unit is defined based on the needs of the assessment. For the deicing salt, the functional unit can be defined as the entire life cycle of the product from the raw material extraction to the disposal to the landfill. System boundary defines the scope of the assessment. The system boundary indicates what products and life stages are considered for the LCA.

2) Life Cycle Inventory (LCI) Analysis:

The life cycle inventory analysis is the most critical step in LCA. In this step, the inputs including energy and resources, and the outputs including the emissions to atmosphere, water, and soil are quantified. The inputs and outputs are then combined in the process flow chart and related to the functional basis (Bayer and Gentry, 2010). At this stage an inventory of all the inputs and outputs to and from the production system is prepared. As an example, the inputs may include electricity consumption and the outputs may include CO2. If the LCI results are consistent and accurate, the products and processes can be compared and evaluated enabling decision makers to make more environmentally friendly decisions.

According to a LCA Guideline developed for AIA, databases and LCA-based tools are critical in providing accurate and reliable results (Bayer and Gentry, 2010). In the next section, the LCA-based tools are highlighted.

3) Life Cycle Impact Assessment:

The life cycle impact assessment translates the result of LCI analysis into impacts on environment and human health. The effects are categorized in various impact categories in order for the users to gain a better understanding of the impacts. For example, the quantified emission of CO2 is translated to its impact on ozone depletion layer. Furthermore, a single value result can be obtained by applying weights to the LCI result. In this case, only one single value is reported rather than multiple impact categories.

4) Interpretation:

In order to report the LCA result in the most informative way, the results are interpreted. The aim of the interpretation step is to help decision makers to easily compare different scenarios; and ultimately, make environmentally friendly decisions.

9.3 The life cycle of deicing salt (Calcium Chloride)

Figure 9-2 presents the system boundary of the life cycle of chemical deicing salts. It begins (cradle) with raw material extraction, preparation, and treatment. From there, it is stored and transported as it moves to the manufacturing process. After manufacturing, it is stored and transported again before being spread on a deck, where it accomplishes its deicing purpose. Afterwards, the remaining salt and byproducts are ideally collected and stored/transported on their way to ultimate disposal in the landfill. However, this is almost never the case and the salt usually ends up leaching into the environment. But that is outside of the boundaries of the system of what can be considered. Thus, a cradle-to-gate approach is suggested to consider the life cycle impacts of deicing salt. The ‘gate’ refers to the delivery of the product (the salt) to the user (the bridge).

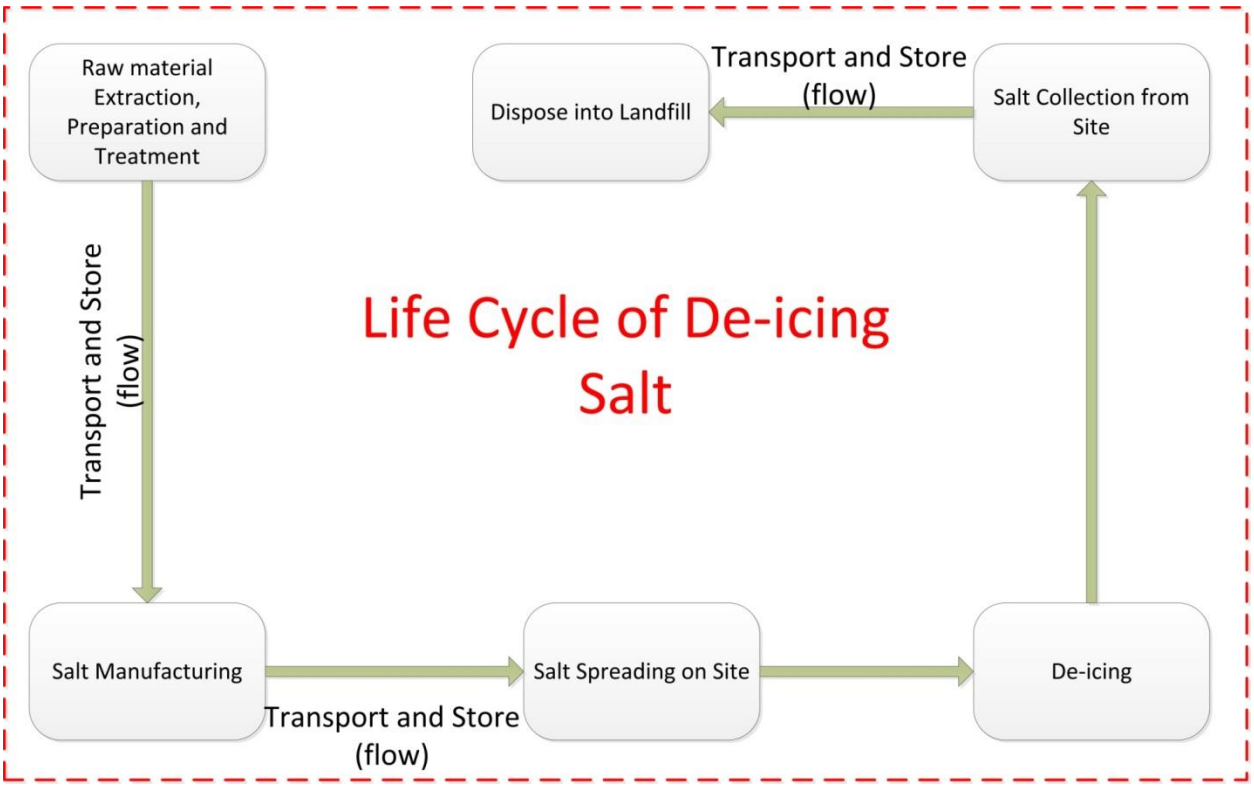

Figure 9-2 **System boundary of the life cycle of deicing salt**

9.4 Cradle-to-Gate life cycle assessment of deicing salt (Calcium Chloride $CaCl_2$)

This section briefly describes a cradle-to-gate approach that could be implemented for the assessment of deicing salt. The table below gives an overview of the product including its description, which is the type of $CaCl_2$ being considered, the project boundaries, the functional unit, and the source of data for the analysis (project libraries).

Table 9-1 **Product overview for a LCA of $CaCl_2$**

Product Name	**Description**	**Project Boundaries**	**Functional Unit**	**Project Libraries**
Calcium Chloride	$CaCl_2$, at regional storage	Cradle-to-Gate	1 kg	Ecoinvent System Processes

A proper analysis would include the environmental impacts from the raw materials used to produce $CaCl_2$, examples of which are given in the table below. Note that the amount represents the amount of raw material required per functional unit (1kg) of $CaCl_2$.

Table 9-2 **Raw materials required for $CaCl_2$ production and processing**

Substance	**Amount (m^2)**
Transformation, from arable	4.75e-7
Transformation, from arable, non-irrigated	0.000115
Transformation, from arable, non-irrigated, fallow	1.08e-7
Transformation, from dump site, inert material landfill	1.06e-5
Transformation, from dump site, residual material landfill	4.35e-6
Transformation, from dump site, sanitary landfill	7.59e-8
Transformation, from dump site, slag compartment	3.08e-8
Transformation, from forest	4.85e-5
Transformation, from forest, extensive	0.000529
Transformation, from forest, intensive, clear-cutting	3.39e-7
Transformation, from industrial area	4.42e-7
Transformation, from industrial area, benthos	6.3e-10
Transformation, from industrial area, built up	3.14e-9
Transformation, from industrial area, vegetation	5.36e-9
Transformation, from mineral extraction site	1.48e-5
Transformation, from pasture and meadow	2.66e-5
Transformation, from pasture and meadow, intensive	9.36e-8
Transformation, from sea and ocean	1.46e-5
Transformation, from shrub land, sclerophyllous	1.67e-5
Transformation, from tropical rain forest	3.39e-7
Transformation, from unknown	0.000106
Transformation, to arable	6.11e-6
Transformation, to arable, non-irrigated	0.000115
Transformation, to arable, non-irrigated, fallow	2.29e-7
Transformation, to dump site	1.62e-5
Transformation, to dump site, benthos	1.44e-5
Transformation, to dump site, inert material landfill	1.06e-5
Transformation, to dump site, residual material landfill	4.35e-6

In addition there will be emissions to the air, water, and soil, examples of which are given below. Again, note that the emissions represent the amount of emission of a given substance per functional unit (1kg) of $CaCl_2$.

Table 9-3 **Emissions to air, water, and soil from $CaCl_2$ production and transportation processes**

Substance	Emission	Amount (kg)
1-Butanol	Air	8.15E-14
1-Pentanol	Air	3.47E-13
1-Pentene	Air	2.62E-13
1-Propanol	Air	8.14E-12
1,4-Butanediol	Air	2.00E-11
2-Aminopropanol	Air	1.08E-14
2-Butene, 2-methyl	Air	5.81E-17
2-Methyl, 1-propanol	Air	6.14E-13
2-Nitrobenzoic acid	Air	1.55E-14
2-Propanol	Air	3.73E-07
Acenaphthene	Air	4.77E-13
Acetaldehyde	Air	3.39E-07
Acetic acid	Air	3.56E-07
Acetone	Air	5.17E-07
Acetonitrile	Air	3.68E-10
Acrolein	Air	1.09E-10
Acrylic acid	Air	9.64E-10
Aldehydes, unspecified	Air	4.71E-09
Aluminum	Air	0.000119
Ammonia	Air	0.00132
Ammonium carbonate	Air	1.00E-10
Aniline	Air	1.47E-12
Anthranilic acid	Air	1.13E-14
Antimony	Air	4.29E-08
Arsenic	Air	3.99E-07
Arsine	Air	1.12E-14
Barium	Air	7.79E-07
Benzal chloride	Air	5.36E-17
Aclonifen	Soil	1.26E-10
Aldrin	Soil	2.48E-11
Aluminum	Soil	4.99E-06
Antimony	Soil	2.92E-12
Arsenic	Soil	1.10E-09
Atrazine	Soil	6.50E-12
Barium	Soil	4.85E-07
Benomyl	Soil	7.87E-13
Bentazone	Soil	6.45E-11
Boron	Soil	2.32E-08
Cadmium	Soil	8.61E-10

Substance	Emission	Amount (kg)
Calcium	Soil	1.89E-05
Carbetamide	Soil	3.21E-11
Carbofuran	Soil	4.32E-10
Carbon	Soil	4.85E-05
Chloride	Soil	5.59E-05
Chlorothalonil	Soil	9.17E-09
Chromium	Soil	2.27E-08
Chromium VI	Soil	7.62E-08
Cobalt	Soil	2.22E-09
Copper	Soil	1.30E-07
Cypermethrin	Soil	6.19E-11
Feniclonil	Soil	3.65E-10
Fluoride	Soil	1.00E-07
Glyphosate	Soil	3.18E-08
Iron	Soil	9.30E-05
Lead	Soil	2.34E-08
Linuron	Soil	9.79E-10
1-Butanol	Water	6.27E-09
1-Pentanol	Water	8.33E-13
1-Pentene	Water	6.29E-13
1-Propanol	Water	1.22E-12
1,4-Butanediol	Water	8.00E-12
2-Aminopropanol	Water	2.68E-14
2-Methyl, 1-propanol	Water	1.47E-12
2-Methyl, 2-butene	Water	1.40E-16
2-Propanol	Water	1.38E-13
4-Methyl, 2-pentanone	Water	3.18E-13
Acenaphthene	Water	1.26E-11
Acenaphthylene	Water	7.87E-13
Acetaldehyde	Water	1.15E-08
Acetic acid	Water	3.00E-08
Acetone	Water	8.66E-12
Acetonitrile	Water	7.17E-14
Acetyl chloride	Water	6.54E-13
Acidity, unspecified	Water	9.07E-09
Acrylate, ion	Water	2.28E-09
Aluminum	Water	0.00115
Aluminum, ion	Water	4.21E-05
Aniline	Water	3.54E-12
Antimony	Water	1.45E-06

Substance	Emission	Amount (kg)
AOX, Adsorbable Organic Halogen as Cl	Water	8.11E-09
Arsenic, ion	Water	4.41E-06
Barite	Water	8.98E-06
Barium	Water	1.64E-05
Benzene	Water	5.10E-07

10. List of references

Abdelaziz SL, Olgun CG, Martin II JR (2011) Design and Operational Considerations of Geothermal Energy Piles, Proceedings of Geo-Frontiers 2011, March 13-16, 2011, Dallas, Texas.

Abdelaziz, S.L., (2013). Deep Energy Foundations: Geotechnical Challenges and Design Considerations. PhD Thesis, Virginia Polytechnic Institute and State University, Blacksburg, VA, 347 pp.

Adam, D. and Markiewicz, R. (2009). "Energy from Earth-Coupled Structures, Foundations, Tunnels and Sewers." Géotechnique. Vol. 59, No. 3, pp. 229–236.

American Association of State Highway and Transportation Officials (AASHTO). (2005). "Grand Challenges: A Strategic Plan for Bridge Engineering." AASHTO Subcommittee on Bridges and Structures, June 2005.

American Association of State Highway and Transportation Officials (AASHTO). (2008). "Bridging the Gap: Restoring and Rebuilding the Nation's Bridges." AASHTO Subcommittee on Bridges and Structures, July 2008.

American Association of State Highway and Transportation Officials (AASHTO) (2012). AASHTO LRFD Bridge Design Specifications, Customary U.S. Units, American Association of State Highway and Transportation Officials (AASHTO), S.l.

American Concrete Institute (ACI) Committee 318. (2011). Building code requirements for structural concrete (ACI 318-11) and commentary, American Concrete Institute, Farmington Hills, MI.

American Society of Heating Refrigerating and Air-Conditioning Engineers (ASHRAE) (2011). 2011 ASHRAE Handbook – Heating, Ventilating, and Air-Conditioning Applications (SI Edition). Atlanta, GA. American Society of Heating, Refrigerating and Air-Conditioning Engineers, Inc.

Amis T, Bourne-Webb PJ, Davidson C, Amatya B, Soga K. The effects of heating and cooling energy piles under working load at Lambeth College. UK. Proceedings 2008.

Baboian, R. (1992). "Synergistic Effects of Acid Deposition and Road Salts on Corrosion." Corrosion Forms and Control for Infrastructure, ASTM STP 1137, pp. 17-29.

Barnard, A.C.L., Hunt, W.A., Timlake, W.P. and Varley E., 1966. A theory of fluid flow in

compliant tubes. Biophysical Journal 6, 717–724.

Barrett, M.L., and Pigman, J.G. (2001). "Evaluation of Bridge Deck Anti-Icing System." Kentucky Transportation Center, Kentucky Highway Investigative Task No. 36.

Basu, P., Loukidis, D., Prezzi, M., and Salgado, R. (2011). Analysis of shaft resistance of jacked piles in sands. International Journal for Numerical and Analytical Methods in Geomechanics, 35(2011), pp. 1605–1635.

Bayer, C., and Gentry, R. (2010), "AIA Guide to Building Life Cycle Assessment in Practice", Prepared for American Institute of Architects, Washington, Dc.

Bhattacharya M.C. An explicit conditionally stable finite difference equation for heat conduction problems, International Journal for Numerical Methods in Engineering, 1985, 21: 239-265.

Bieganousky, W. A. and Marcason III, W. E. (1976). "Uniform placement of sand." Journal of Geotechnical and Geoenvironmental Engineering, 102(ASCE# 11985).Boënnec, O. (2009). "Piling on the energy", Geodrilling International, March 2009, pp. 25-28.

Boënnec O. Piling on the energy, Geodrilling International, 2009; 25-28.

Bourne-Webb P.J., Amatya B., Soga K., Amis T., Davidson C., and Payne P. (2009). "Energy Pile test at Lambert College, London: Geotechnical and Thermodynamic Aspects of Pile Response to Heat Cycles." Geotechnique, Vol. 59, No. 3, pp. 237-248.

Brandl, H. (2006). "Energy Foundations and Other Thermo-Active Ground Structures." Geotechnique. Vol. 56, No. 2, pp. 81-122.

Cady, P.D., and Weyers, R.E. (1983). "Chloride Penetration and the Deterioration of Concrete Bridge Decks." Cement, Concrete & Aggregate, Vol. 5, No. 2, pp. 81-87.

Carslaw HS, Jaeger JC. Heat Conduction in Solids. Claremore Press: Oxford; 1947.

Churchill, S.W., 1997. Friction factor equations spans all fluid-flow regimes, Chemical Engineering 84, 91–92.

Courant R, Friedrichs K, Lewy H. On the partial difference equ.ations of mathematical physics. IBM Journal 1967; 11: 215-234.

Cresswell, A., Barton, M. E., and Brown, R. (1999). Determining the maximum density of sands by pluviation. ASTM geotechnical testing journal, 22(4), 324–328. Retrieved from http://cat.inist.fr/?aModele=afficheN&cpsidt=1203284

Edwards D.K, Denny V.E, Mills A.F. Transfer process, Hamisphere Publishing Crop, New York, 1979.

EGEC (2007) "Geothermal Snow Melting and De-Icing." European Geothermal Energy Council, Brussels, September 2007.

Eskilson P. Thermal analysis of heat extraction boreholes. Ph.D. Thesis, University of Lund, Department of mathematical Physics: Lund: Sweden; 1987.

Eskilson P, Claesson J, Simulation model for thermally interacting heat extraction boreholes.

Numerical Heat Transfer 1988, 13: 149–165.

Fasullo, E.J. (1992). "Infrastructure: The Battlefield of Corrosion." Corrosion Forms and Control for Infrastructure, ASTM STP 1137, pp. 1-16.

Federal Highway Administration (FHWA) (2008). "Status of the Nation's Highways, Bridges, and Transit: Conditions & Performance" Report to Congress, U.S. Department of Transportation Federal Highway Administration, Federal Transit Administration, Washington D.C., 622 p.

Federal Highway Administration, (FHWA, 2010), "Drilled shafts: construction procedures and LRFD design methods", U.S. Department of Transportation.

Gao J., Zhang X., Liu J., Li K., Yang J. (2008a). Numerical and experimental assessment of thermal performance of vertical energy piles: an application, Applied Energy 85; 901-910.

Gao J., Zhang X., Liu J., Li K., Yang J. (2008b). Thermal performance and ground temperature of vertical pile-foundation heat exchangers: a case study, Applied Thermal Engineering 28; 2295-2304.

Ghasemi-Fare, O. and Basu P. (2013a), An annular-cylinder source model for heat transfer through energy piles. Compendium of Papers - 92nd Transportation Research Board Annual Meeting, Washington D.C.

Ghasemi-Fare, O. and Basu P., (2013b). A practical heat transfer model for geothermal piles. Energy and Buildings 66:470-479.

Ghasemi-Fare, O., Basu, P., and Banerjee, S. (2014) Reliability-Based Assessment of Sustainable Heat Exchange through Pile Foundations. Geo-Congress 2014 Technical Papers: pp. 3323-3332. doi: 10.1061/9780784413272.323

Ghasemi-Fare, O. and Basu, P. (2015) Thermal Operation of Geothermal Piles Installed in Sand—A Comparative Assessment Using Numerical and Physical Models. IFCEE 2015: pp. 1721-1730. doi: 10.1061/9780784479087.156

Ghasemi-Fare, O. (2015). Geothermal energy harvesting through pile foundation – analysis-based prediction and performance assessment, Ph.D. dissertation, The Pennsylvania State University, U.S.A.

Gnielinski V. New equations for heat and mass transfer in turbulent pipe and channel flow, International Journal of Chemical Engineering, 1976; 16: 359–368.

Granata, R.D., and Hartt, W.H. (2009). "Integrity of Infrastructure Materials and Structures." FHWA-HRT-09-044, Federal Highway Administration, Washington, D.C.

Hamada Y, Saitoh H, Nakamura M, Kubota H, Ochifuji K. (2007). Field performance of an energy pile system for space heating. Energy and Building; 39: 517-524, DOI: 10.1016/j.enbuild.2006.09.006.

Hoppe E.J., (2000). "Evaluation of Virginia's First Heated Deck Bridge." Virginia Transportation Research Council, Report No. VTRC 01-R8, December 2000.

Ingersoll LR, Zobel OJ, Ingersoll AC. Heat conduction with engineering geological and other applications, second edition. McGraw-Hill; 1954.

Iskander, M. (2010). Behavior of pipe piles in sand. (W. Wu and R. I. Borja, eds.), Springer.

ISO 14040 (2006). "Environmental management - Life cycle assessment - Principles and framework." International Organization for Standardization (ISO), Geneve, Switzerland.

Jalaluddin E, Miyara A, Tsubaki K, Inoue S, Yoshida K. (2011). Experimental study of several types of ground heat exchanger using a steel pile foundation. Renewable Energy; 36: 764–771, DOI: 10.1016/j.renene.2010.08.011.

Javed S., Fahlen P. (2011). Thermal response testing of a multiple borehole ground heat exchanger. International Journal of Low-Carbon Technologies, 6; 141-148.

Johnson, P.M., Couture, A., and Nicolet, R. (2007). "Report of the Commission of Inquiry into the Collapse of a Portion of the de la Concrete Overpass." Quebec, Government of Quebec, ISBN 978-2-550-50961-5, October 2007, 198 p.

Kavanaugh, S.P., Xie, L. and Martin, C., 2001. Investigation of methods for determining soil and rock formation from short term field tests. ASHRAE1118-TRP, American Society of Heating, Refrigerating and Air-Conditioning Engineers, Inc., 77 pp.

Koch, G.H., Brongers, P.H., Thompson, N.G., Virmani, Y.P, and Payer, J.H. (2002). "Corrosion Costs and Prevention Strategies in the United States." Report No. FHWA-RD-01/156, Federal Highway Administration, Washington, D.C., 2002.

Kraft, L. (1991), "Performance of axially loaded pipe piles in sand", Journal of Geotechnical and Geoenvironmental Engineering, Vol 117 (2), pp. 272-296.

Kramer C.A. (2013). "An experimental investigation on performance of a model geothermal pile in sand". M.S. dissertation, The Pennsylvania State University.

Kramer, A. C. and Basu, P. (2014a). Performance of a model geothermal pile in sand. Physical Modelling in Geotechnics – Proceedings of the 8th International Conference on Physical Modelling in Geotechnics (ICPMG) 2014, v 2, pp. 771-777, Perth, Australia, January 14-17.

Kramer, A. C. and Basu, P. (2014b). Experimental characterization of energy output from a model geothermal pile. Proceedings of Geocongress 2014, ASCE, Atlanta, Georgia, February 23-26.

Kramer C.A, Ghasemi-Fare O, Basu P. (2014) P Laboratory thermal performance tests on a model heat exchanger pile in sand, Journal of Geotechnical and Geological Engineering Special Issue on "Thermo-mechanical Response of Soils, Rocks, and Energy Geostructures".

Kusuda, T., and Achenbach, P.R. (1965) "Earth temperature and thermal diffusivity at selected stations in the United States." ASHRAE Transactions, Vol. 71, Part 1, pp. 61-74.

Laloui, L., Nuth, M. and Vulliet, L. (2006). "Experimental and numerical investigations of the behavior of a heat exchanger pile", International Journal for Numerical and Analytical

Methods in Geomechanics, Vol. 30, pp. 763–781.

Lamarche L, Kajl S, Beauchamp B. (2010). A review of methods to evaluate borehole thermal resistances in geothermal heat-pump systems. Geothermics; 39: 187-200, DOI: 10.1016/j.geothermics.2010.03.003.

Lings, M. L., and Dietz, M. S. (2005). "The peak strength of sand-steel interfaces and the role of dilation." Soils and Foundations, 45(6), pp. 1–14.

Liu, Y. (1996). "Modeling the Time-to-Corrosion Cracking of the Cover Concrete in Chloride Contaminated Reinforced Concrete Structures." Ph.D. Dissertation, Virginia Polytechnic Institute and State University, Blacksburg, VA, December 1996, 117 p.

Liu, X., Rees, S. J., and Spitler, J. D. (2003). "Simulation of a Geothermal Bridge Deck Anti-Icing System and Experimental Validation." 82nd Annual Meeting of the Transportation Research BoardWashington, DC.

Liu, X., Rees, S. J., and Spitler, J. D. (2007a). "Modeling snow melting on heated pavement surfaces. Part I: Model development." Applied Thermal Engineering, 27(5-6), 1115-1124.

Liu, X., Rees, S. J., and Spitler, J. D. (2007b). "Modeling snow melting on heated pavement surfaces. Part II: Experimental validation." Applied Thermal Engineering, 27(5-6), 1125-1131.

Liu, X., and Spitler, J. D. (2004). "A Simulation Tool for the Hydronic Bridge Snow Melting System." 12th International Road Weather ConferenceBingen, Germany.

Man Y., Yang H., Diao N., Liu J., Fang Z., (2010). A new model and analytical solutions for borehole and pile ground heat exchangers, International Journal of Heat and Mass Transfer; 53: 2593-2601.

Marcotte, D., Pasquier, P., 2008. On the estimation of thermal resistance in borehole thermal conductivity test. Renewable Energy 33, 2407–2415.

McCartney JS, LaHaise D, LaHaise T, Rosenberg JE. (2010). Application of Geoexchange Experience to Geothermal Foundations. The art of foundation engineering practice. Geotechnical Special Publication No. 198, Hussein, M. H., Anderson, J. B. and Camp, W. M. (eds.); 411-421.

McCartney JS, LaHaise D, LaHaise T, Rosenberg JE. Application of Geoexchange Experience to Geothermal Foundations. The art of foundation engineering practice. Geotechnical Special Publication No. 198, Hussein, M. H., Anderson, J. B. and Camp, W. M. (eds.) 2010; 411-421.

Minsk, D. (1999). "Heated Bridge Technology." Final Report, Report No. FHWA-RD-99/158, Federal Highway Administration, Washington, D.C., 1999.

Naito, C., Sause, R., Hodgson, I., Pessiki, S., and Macioce, T. (2010). "Forensic Examination of a Non-Composite Adjacent Precast Prestressed Concrete Box Beam Bridge." ASCE Journal of Bridge Engineering, Vol. 15, No. 4, pp. 408-418.

Nam Y, Ooka R, Hwang S. (2008). Development of a numerical model to predict heat exchange rates for a ground-source heat pump system. Energy and Buildings; 40: 2133-2140, DOI: 10.1016/j.enbuild.2008.06.004.

National Instruments (2011). LabVIEW. Vers. 2011. National Instruments. Computer software.

Nydahl, J., Pell, K., Lee, R., and J. Sackos, J. (1984). "Evaluation of an Earth Heated Bridge Deck." USDOT Contract No. DTFH61-80-C-00053, University of Wyoming, Laramie.

Olgun, C.G., Martin, J.R., Bowers G.A. (2012) "Energy Piles: Using Building Foundations as Heat Exchangers", Geo-Strata, Professional Magazine of the Geo-Institute, American Society of Civil Engineers, March/April 2012.

Olgun, C.G., Sezen A., Martin, J.R., Abdelaziz, S.L. (2010). "Renewable Energy Applications in Geotechnical Engineering." ZM13, 13th Turkish National Conference on Soil Mechanics and Geotechnical Engineering, Invited Keynote Lecture, September 30-October 1 2010, Istanbul Turkey (In Turkish).

Ooka, R., Sekine, K., Mutsumi, Y., Yoshiro, S. SuckHo, H. (2007). "Development of a Ground Source Heat Pump System with Ground Heat Exchanger Utilizing the Cast-in Place Concrete Pile Foundations of a Building." EcoStock 2007. 8 pp.

Ozudogru, T.Y., Olgun, C.G. and Senol, A., (2014a). 3D numerical modeling of vertical geothermal heat exchangers. Geothermics 51, 312–324.

Ozudogru, T., Ghasemi-Fare, O., Olgun, G. and Basu, P. (2014b). Numerical modeling of vertical geothermal heat exchangers using finite difference and finite element techniques. Geotechnical and Geological Engineering; 33; pp. 291-306; Special Issue on – Thermo-mechanical Response of Soils, Rocks, and Energy Geostructures; Springer; DOI 10.1007/s10706-014-9822-z

Parkin, A. K. and Lunne, T. (1982). "Boundary effects in the laboratory calibration of a cone penetration for sand," Proceeding of the Second European Symposium on Penetration Testing, Netherlands National Society for Soil Mechanics & Foundation Engineering (NNSSMFE), pp. 761–768.

Petukhov B.S, Heat Transfer and Friction in Turbulent Pipe Flow with Variable Physical Properties. Advances in Heat Transfer, J. P. Hartnett and T. F. Irvine, J,R.(EDS.), 6: 503-564, Academic Press, New York , 1970.

Plazak, D.J. (2008). "Strategic Highway Research in the United States." November 2008, Transportation Research Board, The National Academies, 33 p.

Poupard, O., Ait-Mokhtar, A., and Dumargue, P. (2004) "Corrosion by Chlorides in Reinforced Concrete: Determination of Chloride Concentration Threshold by Impedance Spectroscopy." Cement and Concrete Research, Vol. 34, No. 6, pp. 991-1000.

Presetschnik, A., and Huber, H. (2005). "Analysis of a Ground Coupled Heat Pump Heating and Cooling System for a Multi-story Office Building." Proceedings of the 8th International Energy Agency, Heat Pump Conference 2005, pp. 4-8.

Rad, N. S. and Tumay, M. T. (1987). “Factors affecting sand specimen preparation by raining.” ASTM Geotechnical Testing Journal, 10 (1).

Rees, S. J., Spitler, J. D., and Xiao, X. "Transient analysis of snow-melting system performance." Proc., ASHRAE Transactions 2002, June 22, 2002 - June 26, 2002, Amer. Soc. Heating, Ref. Air-Conditoning Eng. Inc., 406-423.

Roosevelt, D.S. (2004). “A Bridge Deck Anti-icing System in Virginia : Lessons Learned from a Pilot Study.” Virginia Transportation Research Council, Report No. VTRC 04-R26, June 2004.

Rouissi K, Krarti M, McCartney JS. (2012). Analysis of thermo-active foundations with U-tube heat exchangers. Journal of Solar Energy Engineering, ASME; 134: 021008-1 - 021008-8.

Salgado, R. (2008). “Analysis and design of single piles” The Engineering of Foundations. Chapter 13, pp. 547-550.

Salgado, R., Mitchell, J. K., and Jamiolkowski, M. (1998). “Calibration chamber size effects on penetration resistance in sand,” J. Geotech. Geoenviron. Eng., Vol. 124, No. 9, pp. 878–888.

Schnaid, F. and Houlsby, G. T. (1991). “An assessment of chamber size effects in the calibration of in situ tests in sand,” Geotechnique, Vol. 41, No. 3, pp. 437–445.

Spitler, J.D., and Ramamoorthy, M. (2000). “Bridge Deck Deicing using Geothermal Heat Pumps.” Proceedings of the Fourth International Heat Pumps in Cold Climates Conference, Aylmer, Québec, August 17-18, 2000.

Strategic Highway Research Program 2 (SHRP2) (2006). “Accelerating Solutions for Highway Safety, Renewal, Reliability, and Capacity.” 2006 Annual Report, Transportation Research Board, The National Academies.

Suryatriyastuti ME, Mroueh H, Burlon S. (2012). Understanding the temperature-induced mechanical behavior of energy pile foundations. Renewable and sustainable Energy Reviews; 16: 3344-3354, DOI: 10.1016/j.rser.2012.02.062.

Tarnawski V.R., Momose T., and Leong W.H. (2011). Thermal conductivity of standard sands II. Saturated conditions, International Journal of Thermophysics 32; pp. 984-1005.

Tuutti, K. (1982). “The Corrosion of Steel in Concrete.” Swedish Cement and Concrete Research Institute, Stochkolm. 469 p.

Uesugi, M. and Kishida, H. (1986). “Influential factors of friction between steel and dry sands.” Soils and Foundations, 26 (2), pp. 33–46.

Uesugi, M., Kishida, H., and Tsubakihara, Y. (1988). “Behavior of sand particle in sand-steel friction.” Soils and Foundations, 28 (1), pp. 107–118.

Virmani, Y.P, Jones, W.R., and Jones, D.H. (1984). “Steel Corrosion in Concrete: pH at Corrosion Sites.” Public Roads, Vol. 84, No. 3, pp. 96.

Virmani, Y.P., Clear K.C., Pasko, T.J. (1983). “Time-To-Corrosion of Reinforcing Steel in

Concrete: Vol.5 Calcium Nitrite Admixture or Epoxy-Coated Reinforcing Bars as Corrosion Protection Systems." Report No. FHWA-RD-83/012, Federal Highway Administration, Washington, D.C., 1983.

Wang, K., Nelsen, D.E. and Nixon, W.A. (2006). "Damaging Effects of Deicing Chemicals on Concrete Materials." Cement & Concrete Composites, Vol. 28, pp. 173-188.

White, D.J., Sritharan, S., Suleiman, M.T., Mekkawy, M.M., and Chulter, S. (2005). "Identification of the Best Practices for Design, Construction, and Repair of Bridge Approach Sections." Final Report, Iowa DOT TR-481, CTRE Report 02-118.

Witte, H.J.L., van Gelder, G.J., and Spitler, J.D., (2002). In situ measurement of ground thermal conductivity: a Dutch perspective. ASHRAE Transactions 108 (Part 1), 263–272.

Yavusturk C. (1999). Modeling of vertical ground loop heat exchangers for ground source heat pump systems. Ph.D. Thesis, Oklahoma State University, USA.

Yunovich, M., Thompson, N.G., and Virmani, Y.P. (2003). "Life Cycle Cost Analysis for Reinforced Concrete Bridge Decks." Paper No. 03309, Presented at CORROSION/03, San Diego, CA.

Zemajtis, J. (1998). "Modeling the Time to Corrosion Initiation for Concretes with Mineral Admixtures and/or Corrosion Inhibitors in Chloride-Laden Environments." Ph.D. Dissertation, Virginia Polytechnic Institute and State University, Blacksburg, VA, January 1996, 140 p.

Zeng H.Z., Diao N.R., Fang Z.H. (2002). A finite line-source model for boreholes in geothermal heat exchangers, Heat Transfer-Asian Research; 31(7): 558-567.